NANOPARTICLES AS CHEMICAL REAGENTS: SYNTHESIS,

CHARACTERIZATION AND POST-SYNTHETIC MODIFICATION OF

FUNCTIONALIZED MONOLAYER PROTECTED GOLD NANOPARTICLE

BUILDING BLOCKS FOR THE CONSTRUCTION OF ADVANCED

NANOMATERIALS

by

EDWARD WHITNEY ELLIOTT III

A DISSERTATION

Presented to the Department of Chemistry and Biochemistry
and the Graduate School of the University of Oregon
in partial fulfillment of the requirements
for the degree of
Doctor of Philosophy

June 2014

DISSERTATION APPROVAL PAGE

Student: Edward Whitney Elliott III

Title: Nanoparticles as Chemical Reagents: Synthesis, Characterization and Post-synthetic Modification of Functionalized Monolayer Protected Gold Nanoparticle Building Blocks for the Construction of Advanced Nanomaterials

This dissertation has been accepted and approved in partial fulfillment of the requirements for the Doctor of Philosophy degree in the Department of Chemistry and Biochemistry by:

Catherine J. Page	Chairperson
James E. Hutchison	Advisor
David C. Johnson	Core Member
Raghuveer Parthasarathy	Institutional Representative

and

Kimberly Andrews Espy	Vice President for Research and Innovation; Dean of the Graduate School

Original approval signatures are on file with the University of Oregon Graduate School.

Degree awarded June 2014

DISSERTATION ABSTRACT

Edward Whitney Elliott III

Doctor of Philosophy

Department of Chemistry and Biochemistry

June 2014

Title: Nanoparticles as Chemical Reagents: Synthesis, Characterization and Post-synthetic Modification of Functionalized Monolayer Protected Gold Nanoparticle Building Blocks for the Construction of Advanced Nanomaterials

The wide variety of novel properties provided by various nanomaterials has striking implications for future applications. However, adoption of new materials is hindered by challenges in material definition, reproducibility, and characterization. While a specific application will define a set of desired properties, the development of a new material that addresses each need often proves challenging particularly when addressed in a linear fashion. With the development of libraries of nanomaterial building blocks and chemical reagents it would be possible to develop a modular approach to the discovery phase. This dissertation describes the development of two such approaches and explores how the challenges of materials definition and characterization may be addressed through the development of characterization sets that afford both corroborative and commentary approaches.

The appropriate characterization of any nanomaterial is challenging regardless of the properties being investigated. Considering characterization during the design of new materials greatly benefits the speed at which new materials may be explored. In addition to addressing characterization challenges, issues of reproducibility are considered early in the discovery phase in order to maximize the utility of the materials produced.

A modular method for the construction of new nanomaterials is illustrated in two

different approaches. The design and synthesis of functional gold nanoparticles that were water-soluble and contained tailored reactive group densities for use as chemical reagents is provided. These nanoparticle reagents are intended to take advantage of the benefits of "click" chemistry, namely the use of readily prepared modular reagents with appropriate functionality compatible with a wide range of synthetic conditions. The direct synthesis method demonstrated here allows for the one-step functionalization of the gold core with both an ethylene glycol diluent ligand for solubility and stability along with functional groups to be used in subsequent azide-alkyne coupling reactions. In the final illustrative approach, functionalized gold nanoparticles were used as building blocks in the construction of a functional nanomaterial assembly. A dilute ozone treatment to remove part of the ligand shell allows for the benefits of ligand-protected nanoparticles while still allowing the properties to the core to be utilized.

This dissertation includes previously published and unpublished co-authored material.

CURRICULUM VITAE

NAME OF AUTHOR: Edward Whitney Elliott III

GRADUATE AND UNDERGRADUATE SCHOOLS ATTENDED:

>University of Oregon, Eugene, OR
>Northeastern Illinois University, Chicago, IL

DEGREES AWARDED:

>Doctor of Philosophy, Chemistry, 2014, University of Oregon
>Master of Science, Chemistry, 2010, University of Oregon
>Bachelor of Science, Chemistry, 2008, Northeastern Illinois University

AREAS OF SPECIAL INTEREST:

>Microfluidic Nanoparticle Synthesis
>Nanomaterial Characterization
>>Small Angle X-ray Scattering
>>X-ray Photoelectron Spectroscopy
>Green Chemistry

PROFESSIONAL EXPERIENCE:

>Graduate Research Assistant, Department of Chemistry, University of Oregon, 2008-2014

>OMSI Science Communication Fellow, Oregon Museum of Science and Industry, 2014

>Custodial Information Consultant, Campus Operations, University of Oregon, 2011-2014

GRANTS, AWARDS, AND HONORS:

>Center for Sustainable Materials Chemistry Information Science Education Follow, University of Oregon, 2013-2014

>Gold Duck Award, Consulting for Facilities Services, University of Oregon, 2011

PUBLICATIONS:

Elliott III, E. W., Oliveri, A. F., Carnes, M. E., Hutchison, J. E., Johnson, D. W. Elucidating Inorganic Nanoscale Species in Solution: Complementary and Corroborative Approaches. *Chem. Phys. Chem.*, **2013**, 14, 2655-2661.

Elliott III, E. W., Fraiman, A. Using Chem-Wiki to Increase Student Collaboration Through Online Lab Reporting. *J. Chem. Educ.*, **2010**, 87, 54-56.

ACKNOWLEDGMENTS

I am grateful to have been provided with the opportunity to conduct this research by Jim Hutchison. In addition to offering countless hours of feedback and encouragement Jim also fostered creativity in research and backed many of my various investigative diversions, which ultimately led several of the breakthroughs in this work.

During my years in the department I had many opportunities for wonderfully productive collaborations that greatly contributed to my success. I cannot thank my co-authors enough, particularly Rick Glover, Pat Haben, Zack Kennedy, Ana Oliveri, and Professor Darren Johnson. In addition, the input of Josh Razink on TEM experiments, Steve Golledge on XPS analysis and Mike Strain on NMR techniques made CAMCOR and the UO NMR facility both invaluable resources that facilitated the depth of my research.

The members, past and present, of the Hutch lab all had a hand in my development as a scientist. It was my first introduction to gold nanoparticles while rotating in the lab under Sam Lohse that kindled my interested in the field. Rick Glover and Zack Kennedy have both been good friends and coworkers throughout as we kept each other (relatively) sane during our tenure as lab mates. Our camping trips to various alpine lakes were as valuable to me personally as our successful research endeavors. Bev Smith taught me a great deal about facing adversity in research and the role that unflinching stubbornness must play when luck just is not going your way. Tatiana Zaikova provided endless scientific insights and plenty of good humor, John Miller, and Lallie McKenzie were helpful sounding boards as well. My time in the bullpen was as character building as it was productive and I wish the best of luck to our most recent lab

members Adam Jansons and Sam Young who both served to remind me that I really do love this science, even as I fell into end of graduate school apathy.

Lastly, but most importantly, I need to thank my family for the support that made it possible for me to even consider this academic endeavour. My amazing wife Magdalena Elliott backed the decision to come to Oregon, even when it meant she had to sacrifice greatly. None of this would have been possible without her support and understanding during this process. My father, E. W. Elliott Jr. supported my meandering road through academia since I was a computer science, philosophy, psychology, and finally chemistry major absolutely unflinchingly. I am grateful that I may now share the light at the end of the tunnel with him. My brother Tim Elliott has always kept me humble; as brothers are want to do. Finally, although we Elliott's lost two our two most respectable members before I could complete this work: my mother Betty F. Elliott and my uncle Tom S. Elliott, their memories continue to keep me motivated to do my best in life.

This dissertation is dedicated to the memory of my mother, Betty F. Elliott (1945-2002)

TABLE OF CONTENTS

LIST OF FIGURES

LIST OF TABLES

LIST OF SCHEMES

LIST OF CHARTS

CHAPTER I

INTRODUCTION: ACTUALIZATION OF FUNCTIONAL NANOMATERIALS

Introduction

The study of nanoscience continues to garner the interest of multiple disciplines. As a crude measure one may look to the plethora of nanoscience research. While it is difficult to determine the exact number of annual publications, it is clear that there are tens of thousands of publications each year and that number continues to grow.[1] Nanomaterials are a broad collection of diverse materials that take advantage of the size dependent properties that manifest themselves on length scales below 100 nm. Nanomaterials research has captured the imagination of scientists and the public alike, with far reaching potential applications as diverse as improvements in biomedical applications, such as imaging[2] and drug delivery[3], as well as sensing[4], nanoelectronics[5] and the functionalization of macroscale objects. The, often difficult to predict, size-dependent properties that deliver such promise also impedes introduction to the marketplace. As research into the synthesis of new materials continues the field would do well to consider the words of George Hammond during his Norris award lecture, "The most fundamental and lasting objective of synthesis is not production of new compounds, but the production of properties."[6]

One specific type of nanomaterial of interest is monolayer protected gold nanoparticles (AuNPs). The understanding and utilization of gold AuNPs began in fits and starts. While gold nanoparticles had been used unknowingly in decorative

applications such as red stained glass for centuries, it was the materials first described by Faraday[7] that marked the beginning of modern chemical research into nanoparticles. It was not until 100 years later that Turkevich's synthesis and characterization of citrate stabilized gold nanoparticles >10 nm in diameter[8] established a foundation for AuNP research. Nearly another 50 years passed before the method developed by Brust afforded the synthesis of alkanethiol monolayer protected nanoparticles below 2 nm in the early 90s.[9] Novel size-dependent properties were discovered in both size ranges. Large gold nanoparticles exhibit a size dependent optical absorbance from 500 - 530 nm. By absorbing the green wavelength of light suspensions of AuNPs, such as those embedded in stained glass, appear red when white light is passed through. The very small nanoparticles have an even more surprising property. While bulk gold is typically regarded as an inert metal, small AuNPs were found to exhibit catalytic activity similar to platinum.[10] In addition to operating as a catalyst for the room temperature oxidation of carbon monoxide, some sizes of AuNPs in solution have also exhibited unprecedented selectivity for partial oxidation reactions.[11,12] In addition to these novel size dependent properties AuNPs were found to be useful scaffolds for the assembly of functional organic ligands.[13] Gold nanoparticle research thus began a climb to prominence within the newly developing field of nanoscience.

The promise of nanoscience has been touted for a number of years, yet there are difficulties in moving from proof-of-concept demonstrations to mass-produced materials. Given the rapid advance in the field this is not entirely unsurprising; however, it may serve to undermine the confidence that the public has in the ability of nanoscience to deliver projected benefits. This current state of affairs may still be regarded as a unique opportunity. As more precisely defined nanomaterials are developed we are afforded

2

information about the properties of these materials, both desirable and deleterious. By iterating nanomaterial synthesis and the determination of structure-function relationships it may be possible to design in specific properties rather than working to change current materials.

The objective of this dissertation is to identify the roadblocks to utilization of functional nanomaterials and develop methods to proactively address these challenges. After first enumerating the promise of harnessing the properties of functionalized nanoparticles, the issues surrounding reproducibility and characterization of well-defined nanomaterials will be introduced. Strategies will be provided that have been developed for addressing these hurdles. Finally, approaches for developing functional nanomaterials efficiently will be presented.

Novel Properties and Applications of AuNPs

Nanomaterials are of interest to chemists and materials scientists due to the multitude of unique properties that may be expressed, as well as the ability to tune those properties. Gold nanoparticles are a particularly versatile class of materials. AuNPs may be readily functionalized with organic ligands and are relatively stable. The size dependent optoelectronic properties may be varied across a range of materials sharing the same surface chemistry. AuNPs are particularly suitable for biomedical applications owing to their stability.[14] Early studies on the toxicity of gold nanoparticles indicated that while the nanoparticles did enter cell bodies, they were not acutely cytotoxic.[15] More recent advances in nanotoxicological testing has demonstrated that toxicity may be dependent on the nanoparticle size[16] as well as the type of ligand shell.[17,18]

In general a functionalized nanoparticle has properties relating to each part of its

3

structure: the core, the ligand shell, and the terminal functionality (Figure 1). The core diameter of an AuNP determines the size dependent absorbance of light of certain wavelengths. Since the absorbance of light depends on the collective oscillation of conduction band electrons the wavelength of light absorbed undergoes a redshift as any dimension of the gold nanoparticle core increases. The ligand shell of a nanoparticle will dictate interactions with the surrounding medium. Ligands may be used to dictate solubility, to reduce the adsorption of other chemical moieties onto the surface, to target specific areas for transport, or to enable sensing by designed self-assembly or disassembly in the presences of an analyte.
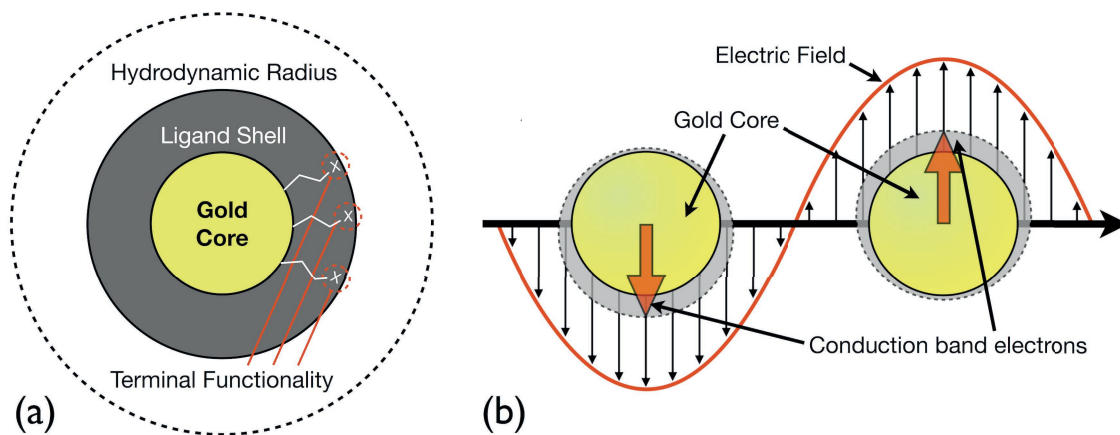
Figure 1. Representation of (a) the various elements considered when defining a gold nanoparticle and (b) simplified representation of the origin of the unique size-dependent plasmon absorbance of gold nanoparticles.

Functionalized nanoparticles have several attributes that have positioned them for extensive use in addressing the current biomedical needs. One of the largest issues facing modern medicine is the treatment of cancer, as incidence of cancer continue to increase.[19] Several studies have demonstrated the promise of well-defined AuNPs for the treatment

of cancer.[20,21,22] The ligand shell greatly determines how a nanoparticle will interact with surrounding biomolecules *in vivo*.[23,24] As a result, PEGylated nanoparticles are particular well suited for these types of applications as the ligand shell has been shown to increase the circulation time of the AuNPs within the blood.[25,26] Very large or anisotropic AuNPs are of particular interest in the treatment of cancer using hyperthermia, the direct heating of a tumorous mass, because the plasmon absorbance may be shifted out into the near-IR region.[27] The long wavelength of light in that region raises the possibility of irradiating the cancer through the skin once AuNPs have been transported into the tumor.[28] Interestingly in biomedical applications the size of the nanoparticle also seems to play a role in determining the transport and compartmentalization of AuNPs within the body.[29,30] One study found that even when the AuNPs were functionalized with peptides known to promote cellular uptake, there were still a significant size-dependence for the ultimate intercellular destination. The largest AuNPs (16 nm) were unable to penetrate the cell membrane, while nanoparticles of 5.5 or 8.2 nm entered the cell and ended up in the cytoplasm, 2.4 nm AuNPs were localized to the nucleus.[31] In the treatment of cancer, it may not be enough to simply enter the tumor cells, as a judicious choice of ligands to target the nucleus of the cell proved most effective for triggering cell death.[32,33]

Ultimately precise control over the size of AuNPs as well as the appropriate mixture of ligands will be required to capitalize on these novel properties. Small changes in core diameter or the ligand shell may have large impacts on the efficacy for a specified application, or even toxicity of the nanomaterials produced. New functionality tends to be added only by layering on additional levels of complexity to the design of the desired nanomaterials, which means that ultimately the most useful particles may be the most difficult to define.

Addressing the Challenges Facing the Adoption of Advanced Nanomaterials

A major barrier to the adoption of new nanomaterials for emerging applications is the difficulty of appropriately defining a given material. As the very nature of these materials means that properties will change with size and morphology it is challenging to know what the appropriate descriptors would be for a given nanomaterial. This in turn informs the characterization challenges, as determination of any given attribute of a new material tends to require development of appropriate methodologies (such as those described in Chapeter II) rather than routine analysis. This uncertainty in material definition leads to an increased economic burden, which is compounded as material complexity increases. Further, this uncertainly leads to difficulty in obtaining or assessing reproducibility as quality control challenges may be quite different from traditional materials, and will be highly dependent on the properties of a given material. As it is unrealistic to require complete characterization of every property of a nanomaterial in every case we are left with an additional regulatory challenge that is the converse of the characterization issue, that is how do we choose an appropriate attribute that encompasses the wide variety of possible nanomaterials. All of these issues, from material definition to reproducibility and characterization along with regulatory definition, must be addressed in order to further advance the field.

Nanoscience has provided the promise of imparting novel material properties and advancing the diagnosis and treatment of disease.[34] It is curious then that although there are many proof-of-concept studies in the research literature the movement of these materials into applications is lagging. One question that must be solved before nanomaterials products can enter the mainstream market is how we define and thus

regulate this category of materials. This issue is many layered, even if we begin by categorizing all materials with at least one dimension under 100 nm as "nano-" we are still lumping together a disparate group of materials ranging from thin films, macro assemblies composed of small building blocks, to polydisperse and poorly defined powders, and relatively monodisperse nanoparticle distributions, or atomically defined macromolecules. Furthermore, the utility of each specific material may be related to very different physical or chemical properties of the material. Finally, we are still left with inconsistencies in the definition and determination of size that further confound the issue.[35]

Regulatory challenges arise out of the definitions that we use to describe a nanomaterial sample. This will play an integral role in the public response to nanoscience as new regulations require product labeling on the basis of the regulator definition of nanomaterials. Even if we consider a relatively straightforward example, a polydisperse size distribution of spherical monolayer protected nanoparticles, the amount of material present in a product may be considered on the basis of surface area, volume, mass, or number count each relevant depending on the application. European regulators recently settled on a definition by number distribution[35] as the European Commission moves forward with requirements for labeling of all nanomaterial containing products.[36] There is a great deal of debate within the scientific community as to which definition is acceptable from a research or regulatory standpoint. Some argue that there should not be a one-size-fits-all definition used in regulation.[37] Others argue that size is an inappropriate attribute for discrimination, and rather an approach based on the appearance of novel size-dependent properties are in order, it has been argued that generally these new properties appear only below 30 nm.[38] Of course any size cutoff for novel properties will

vary wildly on a material by material basis. In the end, these types of nanomaterial regulation may result in the same pitfall, described by K. B. Sharpless, that has plagued organic synthesis: "As it is now, most discovery endeavors suffer from being too invested in *structure*, when *function* is what is sought."[6]

Another reason for the delay in advancing adoption of nanomaterials for new applications has to do with these materials being a victim of their own success. Nanomaterials research is moving to design of materials with multiple specific properties, such as adding the capability for imaging or targeting to drug delivery vectors. As increasingly complex multifunctional nanomaterials are created in an attempt to improve upon the performance of current functional nanomaterials the cost of development can increase significantly.[39] This is because as material complexity increases so too does the cost of synthesis and characterization as well as regulatory hurdles.[40] In part this is due to the current method of introducing additional complexity, where each new material is a discrete one-off design. Taking advantage of more modular approaches to the design of new materials could substantially reduce the burden of complexity.

The challenge now facing researchers is how to address the definition, reproducibility and characterization of new nanomaterials during the design phase rather than when trying to move to market. Reproducibility and characterization are in fact two facets of the same issue, namely that the products of typical nanoparticle syntheses are a polydisperse collection of particle sizes and morphologies. Research articles that neglect this facet of nanomaterial properties, choosing instead to report on an average idealized particle, further confound this problem.[41] Indeed it is difficult to find standard methods of reporting on the size distribution of nanoparticles. Typically the distribution is provided with the assumption that the materials conform to a symmetric Gaussian distribution.

This assumption simplifies reporting by allowing for two parameters, the mean size and standard deviation, to describe an entire size distribution. Occasionally a polydispersity index (PDI), a term borrowed from polymer chemistry, is used. PDI is defined as the square of the standard deviation over the mean particle diameter. This seems needlessly complicated when other reports in the literature simply provide the size distribution in nanometers, or express the polydispersity as a percentage of the mean particle size. The same nanoparticle sample could be reported as being 10.0 ± 3.2 nm or 10.0 nm with a PDI = 0.1 or simply as 10.0 nm with 32% polydispersity. I contend that this final method is most intuitive. When reported in this way it is clear that a size distribution, and not an error, is being described, and it allows for a more useful comparison of nanoparticle distributions with different mean diameters. Further, the definition of a "monodisperse nanoparticle sample" varies from those materials that are defined with atomic precision[42,43], to samples with a PDI < 0.1, or samples with < 10-15% polydispersity each considered by some to be monodisperse. This polydispersity introduces difficulties in characterization (how many particles must be imaged for statistical significance?) and in the definition of reproducible syntheses (must the mean particle diameter be identical, or the polydispersity, or both?). In addition, the wide variety of nanomaterials further confounds the issue, as it may be impossible to define a single set of standard characterization techniques that are appropriate for every sample. Addressing these challenges during the discovery phase will pay great dividends as new hybrid materials are developed for increasing complex applications utilizing the assembly of previous described nanomaterials.

Reproducibility of Nanomaterial Syntheses

Reproducibility in nanoparticle production is an important consideration owing in part to the interplay between unique size-dependent properties and the reality of a polydisperse size distribution that results from syntheses. The scale of nano materials may also introduce sensitivity to impurities that may be present during synthesis. Other synthetic considerations, owing to coupled thermodynamically and kinetically controlled processes in play during nanoparticle synthesis, mean unexpected experimental parameters (the ramp rate to a final reaction temperature for example) may affect size and shape control.[44] In addition, reaction times for the formation of many nanoparticles occur on the time scale, or even orders of magnitude faster, than the time required for mixing. Typical addition of two reagents in equal volume can require mixing times on the order of 10's of seconds.[45,46] However, nanoparticle syntheses, for example the Bunte salt approach used in Chapters 3 and 4, form growing nanoparticles within 150 ms. Rates of mixing, when mixing time is on the order of the reaction time, can alter the cascade of reactions that makes up a nanoparticle synthesis.[47] These effects are evident in the varied products of gold nanoparticle syntheses performed at different flow rates, and thus mixing times, in a microfluidic reactor (Figure 2).

These complications are dealt with within Chapters III and IV by utilizing a simple microfluidic reactor. At high flow rates the microfluidic reactor described acts instead as a mesofluidic reactor, providing Reynolds numbers in the turbulent mixing regime (Re > 1000) where complete mixing would be expected to occur on the order of 1 to 10 milliseconds.[47,48, 49] It is also noted in Chapter III that the use of continuous flow systems helps mitigate the disparity in products produced when multiple researchers perform the same synthesis resulting in improved reproducibility.
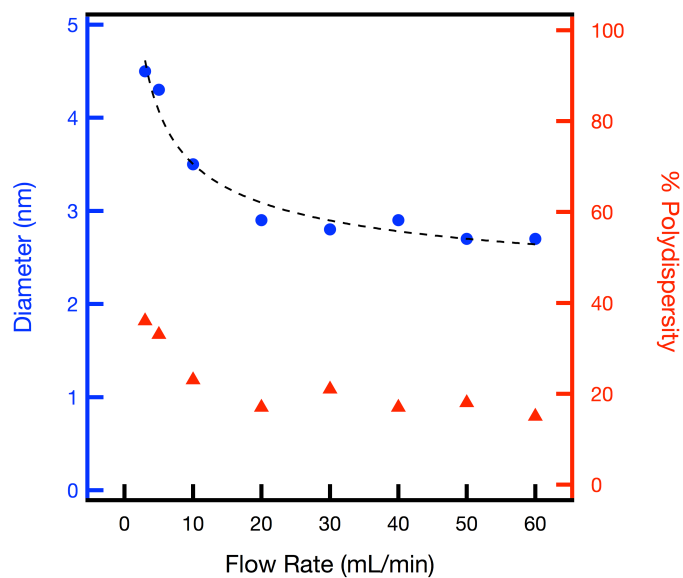
Figure 2. Change in final diameter of nanoparticles produced with the same reagents (a 1:5:2 ratio of Bunte salt ligand / Au(III) / NaBH$_4$) mixed in a T-mixer at various flow rates within the microfluidic reactor described in Chapters III and IV

A final issue with the reproducibility of nanoparticle syntheses is the lack of published data within literature reports, further confounding structure-function investigations.[41] A discussion of the variability of a single synthetic method when performed by a single or multiple researchers is considered in Chapter III. Alternatively it would behoove researchers to simply report on the achieved reproducibility across more than a single batch of material such as the standard deviation in mean diameter during multiple syntheses, such as is illustrated in Chapter IV.

Characterization of Complex Nanomaterials

As described previously, the characterization of nanomaterials is not a trivial task.

Often the techniques that are well suited to nanomaterial analysis require extensive sample preparation, occur in ultrahigh vacuum, and are operating near their fundamental limits. Inadequate characterization may result in confusing or inconsistent experimental results. In addition, there are few techniques that can probe the materials in the environments in which they will be stored or used, such as in solution. A combination of corroborative and complementary techniques are examined, with careful attention paid to which size descriptor is being probed (Chapter II, Figure 2). In addition, it is good practice to utilize techniques that describe both individual nanoparticles as well as measuring bulk properties to ensure the novel properties being investigated do in fact arise from the nanomaterial being described. Indeed, this is becoming a requirement in scientific journals such as *Chemical Communications*. In the following sections the common techniques used throughout this work as introduced with a brief discussion on their relative merits and potential pitfalls.

UV-visible Spectroscopy

One of the first size dependent properties observed in gold was the strong optical absorbance that results in a red color. UV-visible spectroscopy provides a way to quantify the strong plasmon absorbance between 500-530 nm. It has been shown that this UV-visible spectrum may be used both for the determination of approximate concentration and AuNP size in nanoparticle solutions.[50,51] While this is not the most information rich technique of those described herein, it does sample a large number of particle in the most expedient and least costly way and as such is often used as a first look into the properties of new nanoparticles. Analysis of UV-vis spectra can be used to reasonably approximate the size and concentration of many types of nanoparticles in solution. In addition,

qualitative information may be obtained regarding the stability of AuNPs over time as flocculation and aggregation both increase scattering and decrease overall absorbance as nanoparticles precipitate from solution.

Transmission Electron Microscopy (TEM)

Bright field TEM provides micrographs of individual nanoparticles by passing an accelerated electron beam though a thin sample, in much the same way as a typical light microscope.[52] Given that the electron beam must pass through the sample in order to form an image samples must be deposited on substrates designed for use in the TEM. These substrates may be simple films of carbon or specialized substrates using tailored surface chemistry to tether nanomaterials to a surface for study.[53] TEM is often used for the determination of nanoparticle size by using a CCD detector or film to capture micrographs that can then be analyzed by image processing software such as ImageJ.[54] TEM relies on a difference in electron density between the material being studied and the substrate used for imaging, as a result the nanoparticle core, but not the ligand shell, is typically observed. The size distribution defined by a TEM size analysis is a number weighted average of the core diameter of all nanoparticles observed. There are a number of considerations that must be made; in particular a TEM operator must be wary of biasing the resulting analysis because so few particles may be observed at once. In addition, TEM experiments require depositing samples that are then placed in an ultrahigh vacuum environment and then battered with high-energy electrons. As such, significant sample damage including aggregation and growth may occur either during sample preparation or measurement. Figure 3 illustrates the types of images that were acquired over the course of one hour during the determination of a nanoparticle size

distribution. While images such as Figure 3 (A) are useful for the large number of

nanoparticles sampled, they lead to complications in automated size analysis both in
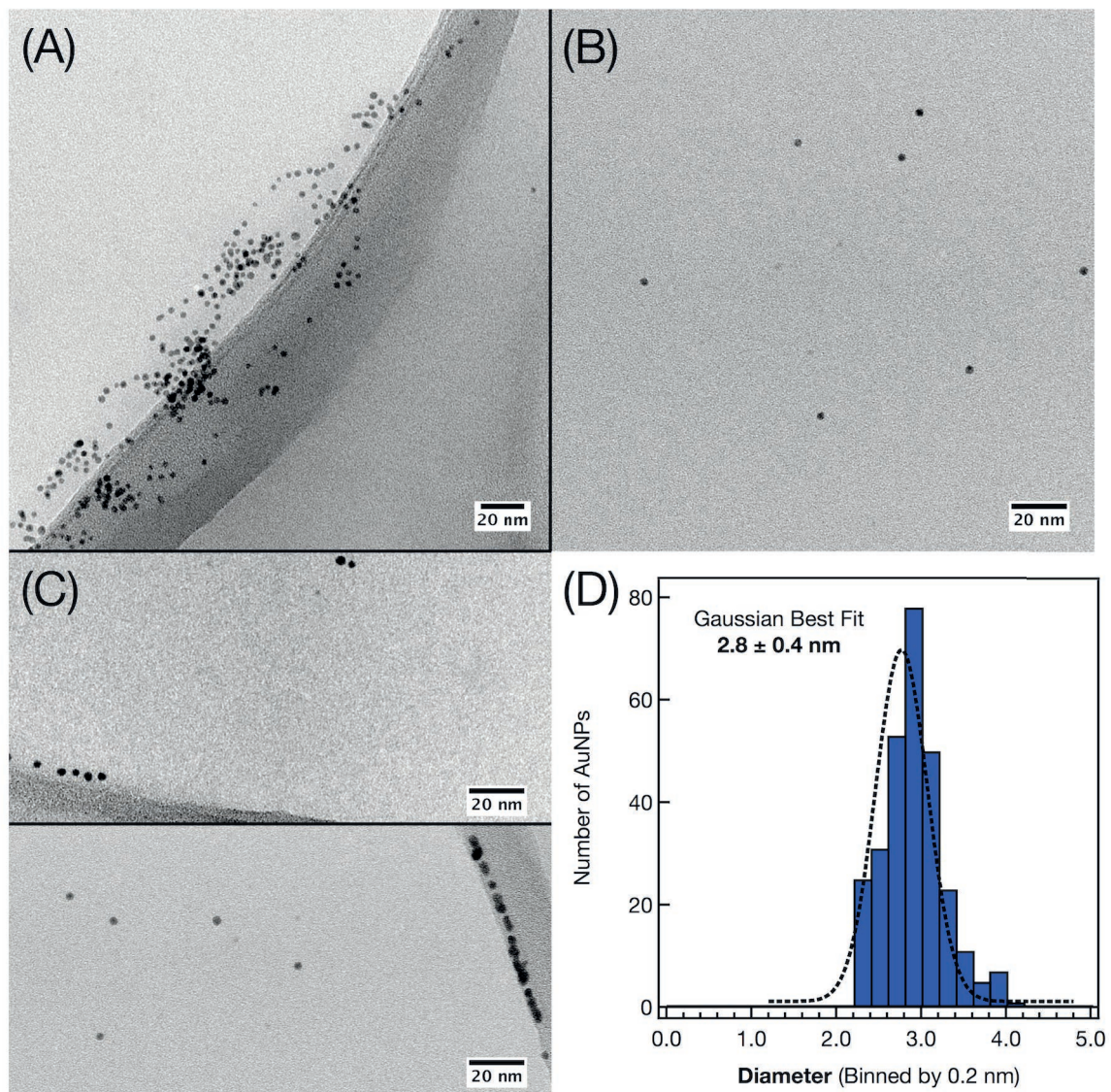
Figure 3. TEM size analysis of AuNPs with a core diameter of approximately 3.0 nm. Of the 20 images acquired in one hour of instrument time there are three general types of micrographs typical of nanoparticle samples including: (A) densely packed particles showing many overlapping particles, typical of 5% of images, (B) well dispersed nanoparticle on a uniform surface, typical of 65% of the images and (C) images containing background artifacts or drying effects, typical of 30% of images. (D) Shows a Gaussian fit of the number distribution of particles.

determining a threshold for binary cutoff and distinguishing the cores of overlapping particles. Ideally, images such Figure 3 (B) would be used exclusively; however, due to the low number of particle counts, even though these types of images make up the majority of those collected they account for less than half of the particles analyzed. Artifacts due to either the substrate used or drying effects, such as those shown in Figure 3 (C) complicate analysis, but should not be excluded outright if operator bias is to be avoided. Ideally, the size distribution shown in Figure 3 (D) should be corroborated by some other method such as SAXS.

Advances in sample holders for TEM imaging are now allowing for the use of liquid samples, at the expense of resolution. However, there are a number of challenges to be considered which introduce artifacts into the data that may skew analysis[55] Other sophisticated sample holders are used for the measurement of a nanomaterials physical properties, such as electrical and mechanical properties, while the material or device is imaged.[56]

Additional imaging modes are also available within a TEM column. Some instruments incorporate a STEM (Scanning Transmission Electron Microscope) for Annular dark-field (ADF) imaging. This technique provides z-contrast, so can be used to gauge thickness of a homogeneous features within a sample, the stacking of nanoparticles, or to show composition differences in nanomaterials composed of multiple elements.[57,52]

TEM is one of few techniques that may be used for the direct observation of nanomaterial morphology. In particular the technique is compatible with nanomaterials that may consist of multiple elements, such as supported catalysts. This is in part due to the ability to perform additional experiments in the same instrument such as Energy Dispersive X-ray Spectrometry (EDX) or Electron Energy Loss Spectroscopy (EELS) in

the same instrument on materials being imaged.[58,59] The shape of a nanoparticle sample can also be readily discerned and in turn used to inform other techniques used for the more accurate determination of a nanoparticle size distribution in solution, such as SAXS described below (Figure 4).
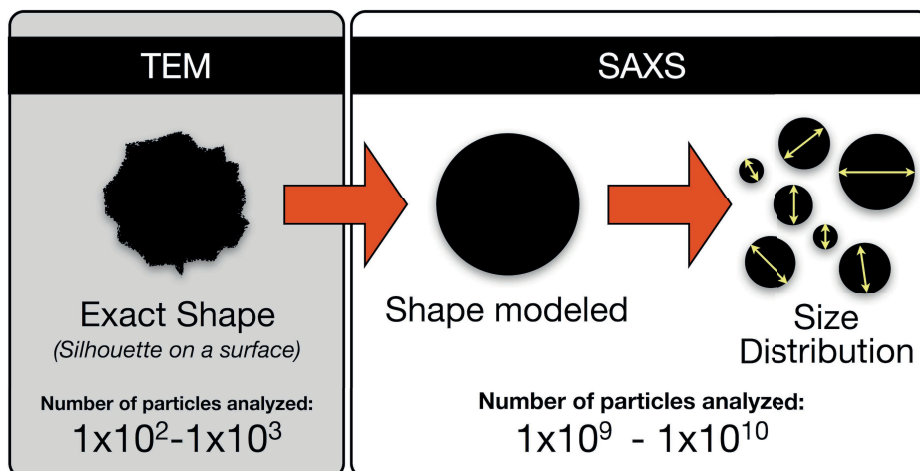
Figure 4. Cartoon representation of how information from TEM and SAXS experiments are used together for accurate determination of nanoparticle size distributions.

Small Angle X-ray Scattering (SAXS)

Once an experimental technique that was the exclusive domain of the beam-line scientist, SAXS instruments are now available on the lab scale. Improvements in the flux of x-ray sources and creative use of optical geometry has made it possible to obtain high quality SAXS data quickly and accurately.[61] Small angle x-ray scattering can be thought of as the interaction between a wave and a point sized object, or the peak broadening of the [000] reflection present in all materials. Mathematically scattering can also be described as a time averaged slice through the Fourier transform of the electron density of a sample.[65] The SAXS scattering pattern is described by the equation relating scattering

intensity to the various components of the sample.[60]

$$I(q) = c\int_0^\infty n(r)[f(qr)]^2 S(qr)dr$$

Where the intensity of scattering, I(q), is proportional to the contrast of the material being investigated relative to the surrounding medium, c, the size distribution of the particles, n(r) where r is the radius of the material, the shape of the particles also called the form factor, f(qr), and order introduced by interactions between neighboring particles described by the structure factor, S(qr).[60] The smallest measureable feature in a SAXS experiment is related to the largest angle measured by the instrument through the equation:[60]

$$R_{min} \approx \frac{\pi}{q_{max}}$$

A typical lab scale SAXS, such as a well-aligned Anton-Paar SAXScess, has a q_{max} = 0.6 Å^{-1} which provides measurements down to R = 5.24 Å.

In principle it is possible to determine structural information about the shape of nanomaterials using SAXS; however there are several obstacles to these experiments. The primary difficulty in analyzing SAXS data is that the integral that describes the scattering data can only be used to go from a geometric model to simulated data. A given scattering pattern does not uniquely describe a single physical model due to effects of averaging the position of nanomaterials over the course of data acquisition. Obtaining more information about the sample then requires one of two approaches, either it is necessary to acquire time-resolved scattering data or it is necessary to make assumptions about the sample that allows for various size distribution models to be simulated.[62] The acquisition of time resolved SAXS data requires the use of incredibly high flux (several orders of

magnitude higher than is possible with lab-scale instruments) and detectors with improved resolution.[63] Instead, in order to maximize the amount of information output from a SAXS pattern a variety of tools that can be used to iteratively fit models to the obtained scattering patterns. Fortunately, the work being performed at beamlines like the Advanced Photon Source has enabled the development of powerful modeling packages that have been used to describe a large range of nanomaterial types which can be used for the analysis of lab-scale SAXS data.[64]

These modeling methods typically consist of solving a system of equations that describing the three morphological aspects of a nanomaterial: shape, size distribution and interparticle interactions.[65] Solving these equations requires that assumptions are made about at least two of the three aspects. For proteins[66,67,68] and other biological macromolecules[69] generally the assumption is that the pure sample is monodisperse, that is contains many copies of identical molecules. Assuming the experiments are also performed under dilute conditions, this affords the ability to determine shape information as well as information about dynamic conformational changes.[70] For nanoparticle samples assumptions are made about all three attributes in order to solve for specific size information. Generally three assumptions made for nanoparticle samples: that the nanoparticle solution is dilute enough to minimize contributes for interparticle scatter, that the nanoparticle size distribution can be described as a Gaussian-shaped size distribution of polydisperse scatterers (other probability distributions may also be used), and that the shape of the nanoparticles are known (and generally assumed to be anisotropic). These assumptions must be justified using other characterization techniques, such as TEM for morphology and UV-vis for concentration, in order to have confidence in the measurements provided by model fitting of the SAXS patterns.[71]

When these corroborative techniques are used the model fitting of SAXS data is generally very robust providing nanoparticle size distributions within < 0.1 nm. This may be demonstrated by comparing multiple measurements of aliquots from the same AuNP solution that was used in the previous TEM size analysis (Figure 4 (D)). As signal-to-noise doubles as acquisition times quadruple, five experiments were performed each doubling the signal to noise ratio (Figure 5).
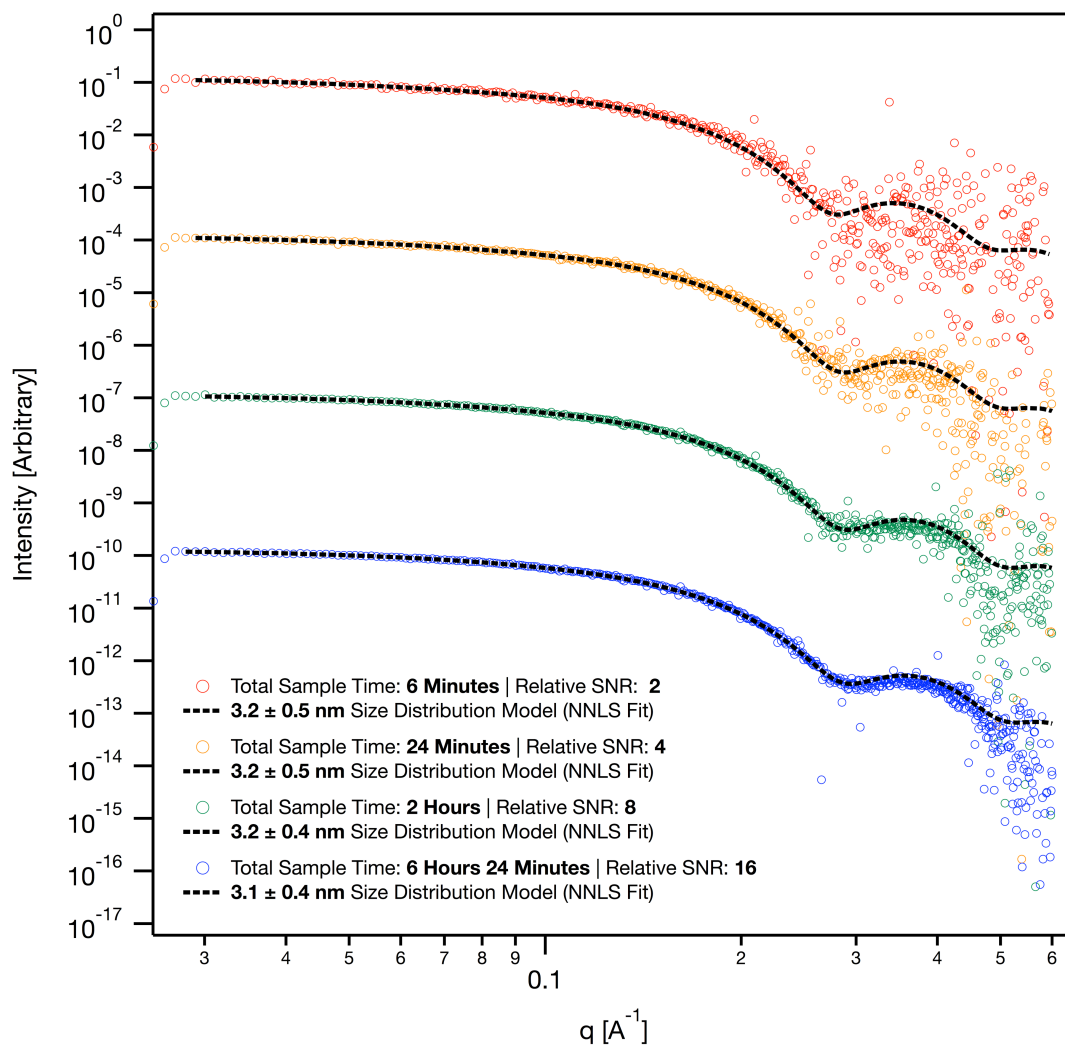
Figure 5. Stacked SAXS data showing the scattering data and corresponding model fits for aliquots of the same nanoparticle solution measured for various times. Acquisition times include the time required for obtaining a nanopure water background and the CCD dark current required for data processing. All models shown were determined by modeling a volume weighted histogram consisting of 200 bins between 0.1 and 10 nm

19

which was then iteratively compared to the scattering data using the NNLS (non-negative least squares) best fit.

The goodness of fit between a SAXS model and the corresponding scattering data is typically described in terms of the reduced chi-squared (the chi-squared value over the number of data points). In general, a good fit may be broadly defined as a reduced chi-squared value of less than 5. In practice noisy data may appear to provide a better fit, as larger error bars for each data point (not shown in Figure 5 for clarity) result in a given model fitting more points by default. For example the model fit the data acquired over 6 minutes provides a reduced chi-squared value of 1 while the model fit for the data acquired over 6 hours 24 minutes provides a reduced chi-squared an order of magnitude higher. Another approach would be to consider the average magnitude of the residuals between models and scattering data. However, this type of analysis is poorly suited to SAXS data where the intensity measured varies by orders of magnitude from low to high q. Because SAXS scattering data is typically displayed on a log-log plot, the determination of relative goodness of fit by eye is misleading. Note that there are orders of magnitude differences between the intensity measured at low and high q and there are an order of magnitude more data points in the region of the data that appears most noisy!

In addition, the simulation of scattering provided by a given model is not an arbitrary line, but rather each portion of the pattern corresponds to different, but interrelated properties of the nanoparticle size distribution. The high intensity data at low q serves to fix the mean size of the model, while the lower intensity region is related to the polydispersity. Because they are interrelated it is not possible to acquire meaningful information if one region is arbitrarily fit without the other. In the end, an empirical determination of goodness of fit should be determined for a given class of sample (defined

by material and solvent type and mean size) by performing a similar study on the effects of changing signal to noise in the measurement. This type of analysis provides the researcher with confidence in the model fit to the data if two or more measurements are made at different acquisition times and the best-fit model converges on the same nanoparticle size distribution. As can be seen in the case illustrated in Figure 5, although the signal to noise ratio is 8 times higher at the longest acquisition times the model fits all agree within < 0.1 nm. The general trend is that noisier data produces a slight apparent increase in mean core diameter as well as an apparent increase in polydispersity. To address concerns of "over fitting" these data we can look to the trends which show that even for very noisy data the mean core diameter is well described, and the polydispersity is, if anything, overstated. An analysis of the uncertainty (also described as error) within the SAXS measurement itself may be obtained by adding Gaussian disturbed noise proportional to the error in each scattering intensity value for several (usually 20-40) iterations. When this analysis is performed on the data with a relative SNR of 2 the error was an order of magnitude below the reported value, with the data with a relative SNR of 16 the error is two orders of magnitude lower.

For further corroboration of the SAXS data we may look to the analysis of the same sample by another technique, such as TEM (Figure 6). When comparing size distributions determined by different techniques there are two consideration: do the techniques measure the same size property of the nanoparticle and do the techniques define the distribution in terms of number of nanoparticles or the volume of those nanoparticles. Both TEM and SAXS measure the core diameter of a nanoparticle sample; however the type of size distribution is a particularly important consideration when comparing TEM and SAXS. The volume distribution determined by SAXS

showed a core diameter of 3.1 ± 0.4 nm. This distribution can be converted to a number

distribution using the total scattering volume for a number distribution corresponding to

2.9 ± 0.4 nm. This agrees well with the TEM size analysis of several hundred particles,

which fit to a Gaussian distribution of 2.8 ± 0.4 nm (Figure 4).
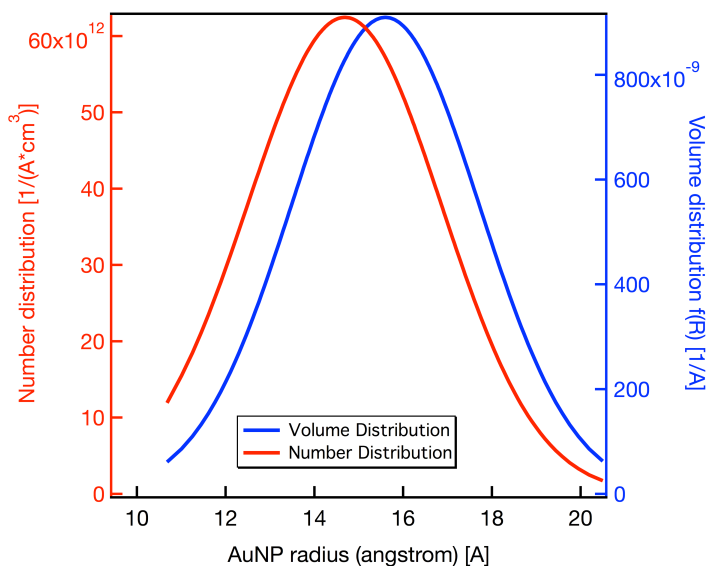
Figure 6. Shows the difference between volume weighted distributions determined by SAXS (d_{core} = 3.1 ± 0.4 nm) and the calculated number distribution corresponding to an identical distribution of nanoparticles (d_{core} = 2.9 ± 0.6 nm). Note that SAXS data are typically modeled using nanoparticle radius as a parameter.

Nuclear Magnetic Resonance (NMR)

NMR is a powerful go-to technique in organic chemistry. Unfortunately

quadrupolar broadening of peaks due to the slow movement of nanoparticle on the NMR

timescale makes detailed analysis of the ligand shell of nanoparticles difficult. One benefit

to this broadening is the ability to use NMR to quickly determine if there are free ligands

present in a purified nanoparticle sample. Further, in the case of thiolate functionalized

AuNPs, the challenges introduced by peak broadening may be overcome by using the

strong affinity of I_2 for a gold surface to release the ligand shell into solution as disulfides.

The composition of mixed ligand shell AuNPs may then be determined if characteristic peaks are isolated.

Nuclear Magnetic Resonance - Diffusion Ordered Spectroscopy (NMR-DOSY)

Diffusion weighted NMR may be used for the determination of diffusion rate of a nanomaterial within a solvent. For a spherical particle in a homogeneous solution, the hydrodynamic radius *r* can then be calculated by using the Stokes–Einstein equation

$$r = \frac{k_b T}{6\pi\eta D}$$

where k_b is the Boltzmann constant, T is the temperature at which the experiment is performed, η is the viscosity of the solution, and D is the diffusion rate of the nanoparticle.[72] Note that the hydrodynamic radius is a size dimension that will include the core, the ligand shell, and the surrounding organized solvent (Figure 1a), a very different descriptor than the core size distribution provided by SAXS or TEM. It is important to recognize that this radius will only be an approximation based on the assumption that the nanoparticle moves like a hard sphere through the solvent in question. Ligand type and resulting solvent interactions may invalidate this assumption resulting in a relative, rather than quantitative size determination unless standards are used.

In nanoparticle characterization, DOSY has been used to complement TEM for size of AuNPs in organic solutions. While the technique may not be suitable for very large nanoparticles, 0.8 to 5.0 nm AuNPs have been successfully analyzed.[73,74] This technique has also been shown to provide a realistic hydrodynamic radius for nanoparticles which may be useful for investigating behavior in solution.[72] While DOSY is a useful technique

for nanomaterial size determination it is important to note that the hydrodynamic radius is often misrepresented in the literature, for example being inappropriately compared directly to sizes determined by TEM without a single caveat.[75] This is of particular concern not only because it convolutes material definition, but also when comparing one type of nanomaterial to another.

X-ray Photoelectron Spectroscopy (XPS)

XPS is capable of providing elemental composition and information about the oxidation state of those elements.[76] In addition, elemental mapping is possible with micron resolution.[77] XPS is generally considered to be a surface sensitive technique because the low energy photoelectrons generated by the x-ray source are scattered as they travel though the sample. For planar materials this means that only electrons generated in the top few nanometers escape and are able to be detected. However, the electron attenuation length is on the order of typical nanoparticle sizes, which allows for the determination of elemental composition throughout the entire material. One concern is signal due to the underlying substrate when thin layers of small nanoparticles are measured. This can be mitigated either through the use of a conductive layer such as chromium or by sampling an identical substrate which may then be subtracted from the sample spectrum as described in Chapter V (Appendix C, Figure S4).

The binding of sulfur with gold surfaces has been extensively studied.[78]There are differences in the binding energies associated with organic ligands bound to nanoparticle versus planar surfaces.[79,80] With the proper use of standards, small shifts in binding energy may be used to explain to complex surface binding phenomenon.[81] XPS cannot provide information about the absolute amount of any given element; however, it is possible to

perform high resolution scans of specific elements within a sample in order to get a ratios between various elements in different oxidation states. This type of analysis is complicated with nanomaterials due to attenuation effects as the excited photoelectrons travel through a sample. While there are geometric corrections that may be performed for deconvolution of these effects in a well-defined large sample, the organized spatial distribution of elements often present in nanomaterial samples further complicates determination of absolute ratios. These factors mean that complete analysis of nanomaterials may require extensive modeling and analysis of peak shape[104], as well as the use of standards, to gain further information about nanomaterial morphology and composition.[82]

Thermogravimetric Analysis (TGA)

The ligand shell dictates many of the properties of interest in functionalized nanoparticles. While XPS can provide some information about the composition of a nanoparticle sample, quantification is often impossible. However, TGA is an ideal complementary technique that, when used together, can provide a direct measurement of the ligand shell. While the core material of typical nanoparticles is inorganic, either a metal or metal oxide, the ligand shell is composed of organic molecules that may be removed by heating. Alone TGA can provide ratio of the mass of the ligand shell, which is vaporized, and the mass of the core material, which is not. When used in concert with information about the design of the nanomaterials, the ratios of elemental composition (from XPS) and the size distribution of the nanoparticle (from either TEM or SAXS) it is possible for TGA to be used to determine the average number of ligands on a particle of the mean diameter.[83] This in turn provides information on the packing density of the

ligand shell which has implications for nanoparticle stability in solution. TGA has also been used to investigate the behavior of nanoparticles as they are heated to induce sintering which has important implications for catalysis applications and the preparation of porous electrodes.[81]

Gold Nanoparticles as Reagents in Chemical Synthesis

Early research into new nanoparticles was driven solely by the discovery of novel properties arising at the nanoscale. Now multifunctional nanoparticles with additional layers of structural complexity are being developed for use in targeted drug delivery, imaging, and sensing applications. Increasingly these nanoparticles are being used as building materials for the additive design of more complex nanostructures. Using organic chemistry to functionalized AuNPs generates functional inorganic -biomolecule hybrid nanomaterials.[84] Taking inspiration from the chemistry performed by biological systems, self-assembly processes for production of "higher-level hybrid structures" are also being developed.[85,86] With additional complexity comes additional synthetic and characterization challenges.

Nanoscientists are not alone in facing increasing complexity as their toolkit of synthetic techniques expands, organic chemists in the pursuit of synthetic strategies for the production of natural products face similar challenges. As such it would be wise to heed the wisdom of K. B. Sharpless who said: "If useful properties are our goal … then the use of complicated synthetic strategies is justified only if they provide the best way to achieve those properties."[6] Often linear synthetic routes are used as a research group builds upon previous work. Yet this strategy of synthesis at any cost, overlooking issues of process development, proves costly and time consuming. Instead during the discovery

phase syntheses may be designed to utilize efficient syntheses of various building blocks, which could then be used in the generation of complex nanomaterials via convergent syntheses. This would have the added benefit of not only saving time and money, but also in speeding the adoption of nanomaterials in the consumer market.

The promised benefits of modular assembly in organic chemistry were realized with the advent of click chemistry. Click chemistry is defined broadly as a set of synthetic reactions that are thermodynamically driven and may be used for the efficient, modular construction of target molecules. With such an approach syntheses are designed with features amenable to scale up and rapid modification from the start. Thus the promise of click chemistry is not only an increased rate of development of new materials affording a broader parameter space in structure-function investigations, but also lowered costs. An ideal synthetic approach is one that adheres to a few basic principles such as being modular, wide in scope, insensitive to water and oxygen, as well as affording ease of purification with chromatographic techniques.[6] Designing nanomaterial syntheses with these principles in mind will pay compounding dividends over time not only in money saved, but also by allowing for the rapid development of new materials for structure activity relationship studies.

Modular assembly of specifically synthesized monomers, a concept explored at length within click chemistry, allows one to compartmentalize the challenging organic chemistry to a small molecule fragment before assembling these fragments (or substructures) into a larger structure. A similar approach can be taken in the synthesis of hybrid nanomaterials, performing troublesome organic chemistry steps on ligand precursors prior to nanoparticle synthesis or optimizing nanoparticle syntheses independent from the synthesis of complex targeting groups. For example, masked thiols

can be used in the preparation of thiolate protected AuNPs while avoiding some of the pitfalls of thiol reactivity, such as the formation of disulfides which react with very different kinetics to their thiol analogs. This have been demonstrated for thioacetates[87], and S-alkylthiosulfuric acids, also known as Bunte salts[88,89,90]. The term Bunte salt is discourage as obsolete by the IUPAC;[91] however, the term shows signs of continuing popularity even within the organic chemistry community.[92] Bunte salts, in particular, have properties that are particularly of interested to the researcher in lab, namely their facile preparation from corresponding halides[93,94], a lack of offensive odor owing to their low volatility, and their shelf stability[95,63]. In addition Bunte salts tend to be water soluble due to their charge, which allows for water to be used as a benign solvent. Purification is a necessary consideration as well, and by designing syntheses that use water as a solvent diafiltration can be used to allow for the effective and reproducible removal of impurities.[96] Well designed, stable, nanoparticles may include functionality amenable to further coupling reactions following synthesis allowing them to be used as reagents in subsequent assemblies.[97,98,99,100,101,102,103] Further, developing nanoparticle reagents would allow for scientists with diverse expertise to capitalize on nanoscience research. This would have similar impacts to the development of the automated syntheses of proteins and other biomolecules, which made it possible or a non-biochemist to incorporate these molecules into their research, greatly expanding the potential applications conceptualized.

Thesis Overview

The intent of this dissertation is to provide a framework for the design, synthesis, modification, and characterization of functional nanomaterials. Chapter II describes the

challenge of defining a nanoscale material. For a well-defined inorganic nanoscale species, a size measurement can describe a number of different dimensions (core, shell, solvation sphere). Often these size parameters are reported out of context or even inadvertently misrepresented. Since many of the techniques used to measure size depend on significant and sometimes destructive sample preparation, an additional challenge is defining "what size means" for a nanoscale species while still in solution. The distinction is drawn between complementary techniques that can be used together to unveil more information about the material in question, and corroborative techniques, which are used to make multiple measurements of the same property for verification. Additionally, corroborative techniques can be used to measure the same property in and out-of solution so as to reveal details about solution behavior. Various approaches to this characterization challenge are provided in the context of three case studies demonstrating the use of both complementary and corroborative techniques to elucidate the various size-properties of different types of inorganic nanoscale species in solution. This chapter was developed for publication with my co-authors Anna Oliveri, Matt Carnes, Jim Hutchison and Darren Johnson.

Chapter III describes a new method for the direct synthesis of functionalized gold nanoparticle that affords simultaneous control over the final core diameter independent from the functionality chosen. In addition a convenient, single-step synthesis is described that produces ligand-stabilized, water-soluble gold nanoparticles (AuNPs) with diameters in the range of 2-10 nm. The nanoparticles properties due to the surface chemistry and core size/structure can be simultaneously controlled. The method overcomes a traditional limitation to synthesis imposed by the fact that the ligands used have a direct impact on nanoparticle size during synthesis. As a consequence multifunction

nanoparticles required for biomedical and other applications can be easily and reproducibly synthesized. In the new synthesis, reduction of a Au(III) species with sodium borohydride in the presence of a functionalized alkyl thiosulfate (Bunte salt) yields monolayer-protected AuNPs. AuNP core size can be controlled by varying the pH of the gold salt solution because the speciation of Au(III), and the kinetics for its reduction, depend upon pH. The dependence of the core size on the pH was different for each ligand functionality studied. However, a working curve can be plotted for each that can be used to identify conditions to synthesize particles with specific, targeted core diameters regardless of the influence of the specific ligand. Using this approach reaction conditions can be rapidly optimized using a combination of a microfluidic reactor and automated small-angle X-ray scattering (SAXS) size analysis. The synthetic method demonstrated here eliminates the need for ligand exchange with or without phase transfer catalysts and thus avoids complexity due to additional synthetic steps or the possibility of a change in nanoparticle core size during ligand exchange. This approach enables the development of libraries of related particles for rapid investigations into structure-function relationships. This work was submitted for publication with my collaborator Pat Haben under the guidance of Jim Hutchison.

Chapter IV demonstrates the realization of a gold nanoparticle reagent for use in the construction of complex nanomaterials. Small (D_{core} < 5nm) water-soluble gold nanoparticles with tailored reactive group densities were developed to allow for direct synthesis and ease of purification and isolation. These nanoparticle reagents are intended to take advantage of the benefits of "click" chemistry, namely the use of readily prepared modular reagents with appropriate functionality. Typical synthetic approaches relied on the synthesis hydrophobic nanoparticles followed by ligand exchange reactions, which are

time intensive, often incomplete and may suffer from changes in core diameter or loss of material. In contrast, the direct synthesis method shown here allows for the use of an ethylene glycol diluent ligand for solubility and stability along with varied numbers of functional groups to be used in subsequent azide-alkyne coupling reactions. The nanoparticles remain stable when purified using tangential flow filtration and are readily resuspended following lyophilization. The reactivity of the resulting nanomaterials is then demonstrated by coupling to a variety of hydrophobic and hydrophilic moieties with terminal functionality using a simple copper catalyst. Copper-free reaction conditions were also investigated using strained cyclooctynes. The diameter of the core was maintained throughout the reaction and particles remained soluble even after coupling was complete. These hybrid nanoparticle products retain properties of both the azide functionalized nanoparticle reagent, such as water solubility and optoelectronic properties, along with the properties introduced by the incoming moiety such as fluorescence. These AuNPs are of potential interest as reagents in the preparation of complex nanomaterials for biomedical applications where stable, precisely defined, biocompatible particles are required. The ease of synthesis of these materials along with their stability during coupling and purification provided access to a breadth of related materials that may be rapidly prepared and screened. This work was completed and is intended for publication by Zack Kennedy, Zhenshuo Feng, Jim Hutchison and myself.

Chapter V describes a method of gently removing the ligand shell of monolayer protected AuNPs in order to generate a reactive gold surface that may be exploited. The size dependent properties of surface-confined inorganic nanostructures are of interest for applications ranging from sensing to catalysis and energy production. Ligand-stabilized nanoparticles are attractive precursors for producing such nanostructures because the

stabilizing ligands may also be used to direct assembly of intact nanoparticles on the surface. However, for applications requiring direct access to the core, these ligands block the active surface of the nanoparticle. Typical methods used to remove these ligands typically results in release of nanoparticles from the surface or causes undesired growth of the nanoparticle core. A mild chemical oxidation step using 50 ppm of ozone in nitrogen lowers the ligand's affinity and permits the removal of the ligands at room temperature by rinsing with water. XPS and TEM measurements conducted using a custom planar analysis platform were performed to assess changes in the ligand shell and nanoparticle core during treatment. Using dilute ozone it is possible control the amount of ligand removed by adjusting the treatment time. The particles retain their original core size and remain tethered on the surface. Carbon monoxide oxidation was then used as a functional assay to demonstrated ligand removal from the gold surface for nanoparticles assembled on a high surface area support. This work was completed with Rick Glover and Jim Hutchison and is intended for future publication.

Bridge to Chapter II

Before the design and synthesis of a nanoparticle reagent could be realized it was necessary to improve upon material definition. During my rotation in the Hutchison lab during my first year I was introduced to the synthesis of gold nanoparticles using biomolecules as ligands. Initial experiments quickly demonstrated some of the issues related to a lack of reproducibility and difficultly of characterization. As the CAMCOR facility at the University of Oregon grew I was presented with the opportunity to utilize additional characterization techniques (XPS) and cutting edge instruments (The FEI Titan Electron Microscope). It was during my work with Patrick M. Haben at the

32

Advanced Light Source in the Lawrence Berkeley National Lab that I first saw the capabilities that SAXS could offer in the analysis of gold nanoparticles *while in solution*. With the acquisition of a lab-scale SAXS (the Anton-Paar SAXScess) new studies were suddenly viable. In Chapter II the multitude of instrumental techniques available at the University of Oregon are utilized to address the solution phase characterization of nanomaterials. The need for both complementary and corroborative techniques in the definition of novel materials is explored. In addition, the implications of appropriate (and inappropriate) definition of a given nanomaterial are considered.

CHAPTER II

ELUCIDATING INORGANIC NANOSCALE SPECIES IN SOLUTION:

COMPLEMENTARY AND CORROBORATIVE APPROACHES

Introduction

Corroborating the solid-state structure to solution structure and elucidating solution dynamics have been challenging goals confronted by many researchers, particular in supramolecular chemistry and nanoscience. If a substance can be crystallized, solid-state structures can confidently be determined using single crystal X-ray diffraction (XRD), but what exists in the solid-state does not always reflect the relevant species in solution. Small molecule synthetic chemists have adopted a set of complementary techniques commonly used to identify and confirm a molecular structure in solution (NMR, UV-Vis, IR, and Mass Spec).[1] Inorganic clusters, nanoparticles, and related species, together referred to henceforth as "inorganic nanoscale species", are not as easily structurally characterized using these techniques. In this Concept, the complementary combination of Small Angle X-ray Scattering (SAXS) and Diffusion Ordered Spectroscopy (DOSY NMR), as well as other analytical techniques, are reviewed and discussed for their use in the study of inorganic nanoscale species.

The dynamic behavior of inorganic nanoscale species in solution is of fundamental interest to inorganic, materials, and geological chemists; however, it is first necessary to identify the predominant species in solution before more thorough investigations can occur. One such inorganic nanoscale species which possesses interesting solution behavior is the cluster $Ga_7In_6(\mu_3\text{-}OH)_6(\mu\text{-}OH)_{18}(H_2O)_{24}](NO_3)_{15}$ (**Ga₇In₆**) (Figure 1). The solid-state structure of this discrete nanoscale cluster has been determined by single crystal X-ray diffraction. Researchers have discovered that these clusters make superb precursors for homogenous, smooth, defect free $InGaO_3$ thin films when using a simple spin coating method from aqueous solution, followed by mild annealing.[2] This type of solution processing has then been used to produce transistors incorporated into a functioning prototype liquid crystal display (LCD).[3] This finding raises the question of how and why do these clusters form and subsequently condense to produce films of far superior quality than the corresponding simple inorganic salts? Similar questions can be asked about nanoparticle behavior in solution. How do reaction conditions drive nanoparticle formation and subsequent ligand passivation of the core? Also, how do functionalized nanoparticles undergo self-assembly into more complicated devices? Before these more challenging questions can be answered, we must first find or develop techniques that are able to detect and define the relevant inorganic nanoscale species in solution.[4]

Some standard methods used to identify stable inorganic nanoscale species rely on significant sample preparation (SEM, TEM, AFM, XPS, and X-ray crystallography). These techniques each require species to be isolated from solution, which necessitates a large change in concentration and, in some cases, exposure to ultra-high vacuum (UHV). This makes it impossible to verify that the results of these experiments describe the

properties of the relevant species when in solution. For the analysis of the core dimensions of inorganic nanoscale species in solution, recent literature makes it clear that SAXS sells.[5–7] While powerful, this technique is not a stand-alone source for the identification and characterization of inorganic molecules and particles in solution. The best source of verification comes from a complement of solution analysis techniques. While NMR spectroscopy has been attractive to many fields, not until recently has interest in NMR resonated with inorganic cluster and nanoparticle researchers. Corroborative techniques such as DOSY NMR or DLS, which measure hydrodynamic radius, seem like ideal mates for SAXS analysis.
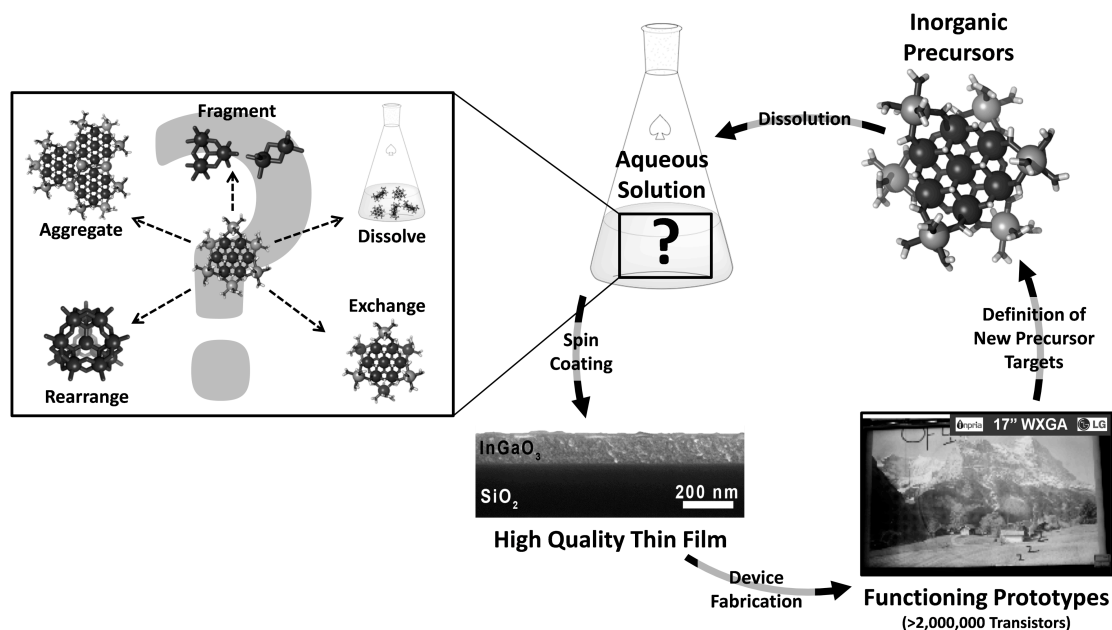
Figure 1. Determining the fundamental solution behavior of inorganic nanoscale species allows for the design and control of the syntheses of new precursors used in the production of functional materials. In this specific example, understanding the fundamental dynamic behavior of the nanoscale cluster **Ga₇In₆** in solution allows for better design of clusters for similar application cycles.

Solid-state analytical techniques are information rich, and would be even more powerful assets if related directly to complementary solution based characterization. In order to leverage the information available, the species in solution must first be observed. From there a combination of techniques can answer the more complicated questions of interest to researchers. In this Concept paper we illustrate how new strategies to elucidate the dimensions of inorganic nanoscale species in solution lead to significant advances in the understanding of solution structure and dynamics. These advances will, in turn, lead to better control and refinement of the chemistry and resultant materials properties.

Complementary and Corroborative Solution Techniques

This Concept will first review a variety of techniques commonly available for the analysis of size in solution (UV-Vis, ESI-MS, DOSY, SAXS, and DLS). Techniques that can provide complementary spectral signatures for the inorganic nanoscale species in solution are also discussed (NMR, Zeta-potential, UV-Vis, IR, and Raman). While there are a number of other information-rich techniques, the focus here is on those that are commonly available at a typical research institution. Although each of these techniques has an important function in the analysis of certain compounds, this Concept focuses on the characterization of clusters, nanoparticles, and other inorganic species in solution from the perspective of synthetic materials chemists.

Given the limited literature precedence and the restrictions of the techniques used for the characterization of nanoscale inorganic species in solution, researchers must first be able to predict an expected size range for the stable species making this an iterative process. This necessity demonstrates that size actually does matter. In an ideal case, a solid-state technique such as crystallography can be used to guide the search in solution

while keeping in mind that the isolated solid-state species may not be the same as the relevant species in solution. There are several dimensions of well-defined nanoscale inorganic species that can be measured and described as size. The concept of size is fundamentally ambiguous as it may be related to the ***core***, ***shell***, or ***outer solvation sphere*** of the structure in question (Figure 2). While alone each technique is able to provide some indirect measure of size, the complete determination of the size-properties of any given material requires corroboration or the correlation of multiple complementary techniques. Once the size-properties have been determined, the material may be subjected to a multitude of techniques to determine more detailed structural properties. These techniques can be used in concert to elucidate more complex dynamic behavior in solution.
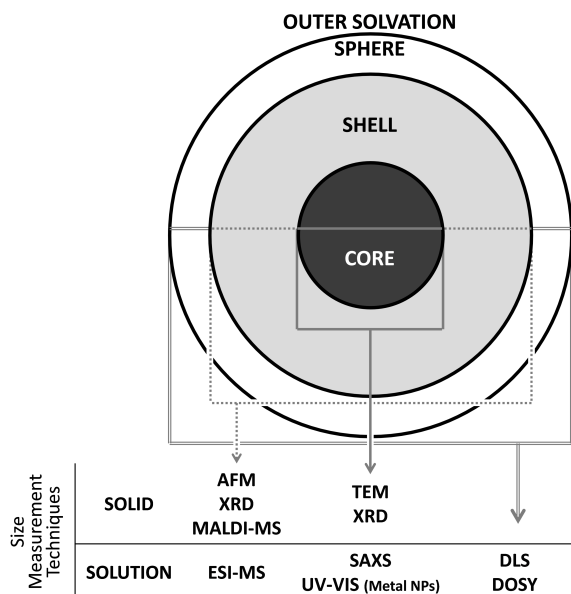
Figure 2. ***Core***, ***shell***, and ***outer solvation sphere*** dimensions in inorganic nanoscale species. The multiple corroborative techniques capable of measuring the same dimension are grouped in columns by color. Techniques in separate columns complement one another by measuring different regions.

Small Angle X-ray Scattering (**SAXS**) uses the elastic scattering of monochromatic X-ray radiation to determine the size, shape, and volume of nanoscale particles in solution. For inorganic clusters and nanoparticles the technique is best suited to the measurement of the core, where the elements are of significantly higher or lower Z than the solvent. SAXS was developed for the determination of the shapes of large biomolecules using synchrotron radiation sources. Advances in X-ray generator technology and the use of line source collimation now enables this technique at the lab-scale. While scattering data may be analyzed using model-independent approaches, much of the utility of SAXS for the analysis of small (< 5 nm) inorganic clusters is derived from direct modeling. The information that can be obtained from a SAXS experiment depends on the type of sample being analyzed as well as what is already known about the material.[8] For polydisperse materials, a size distribution can be determined if information about shape is known. If the material is well-defined and monodisperse, information about shape can be extracted along with size. For this reason it is important to couple SAXS analysis with another technique in order to maximize the information gained. The ***core*** size can be corroborated with solid-state measurements (XRD or TEM), or complementary techniques can be used to measure the ***shell*** or ***solvation sphere*** in solution in order to correlate with the core size (Figure 2). One obvious advantage of the use of SAXS for ***core*** size determination is the ability to characterize the material in solution without the risk of artifacts from sample preparation. SAXS also allows for the variation of sample parameters such as solvent, temperature, or pH. However, in order to produce scattering there must be a contrast in electron density between the material of interest and the solvent used.[9] Additionally, solvents with a very high X-ray absorbance, including many halogenated organic solvents such as chloroform

and dichloromethane, are not well suited to analysis by lab scale instruments because the majority of photons will not reach the X-ray detector.

Nuclear Magnetic Resonance (NMR) spectroscopy can provide information about structure, concentration, dynamics, reaction rate, and chemical environment, among others. Using a magnetic field, NMR aligns the spin of nuclei in a molecule then measures their relaxation. Depending on the atom and its environment, the frequency of relaxation will result in a signal with a specific chemical shift. Structural information can be gained from NMR, but prior chemical shift information is necessary and not easily found for many inorganic species. To assign chemical shifts in molecules with no literature precedence, high-level computations are required. When working with ^{1}H nuclei there can be sample-dependent solvent limitations due to exchange between the protons of the molecule in question and the solvent. This is usually not an issue when working with other NMR-active nuclei. Unfortunately, any paramagnetic metal will lead to severe broadening of NMR signals making it more difficult to gain useful information from the spectrum.[1,10] Two-dimensional NMR techniques have allowed for complex structural problems to be tackled more easily. By applying field gradients, ***Diffusion Ordered Spectroscopy*** (**DOSY**) has allowed for the measurement of the translational diffusion coefficient, caused by Brownian motion, of a molecule relative to the solvent. Once the viscosity of the sample is measured, the Stokes-Einstein equation can be used to approximate the ***solvation sphere*** of a spherical species.[11,12] This measurement can be corroborated in solution with DLS measurements and complemented with techniques measuring the **core** or **shell** (Figure 2).

Electrospray Ionization Mass Spectrometry (**ESI-MS**) is capable of determining the molecular weight and fragmentation pattern of many discrete molecular

species. By charging a fine spray of a very dilute (10^{-5} M) solution of the species, the mass to charge ratio of the resulting fragments can be determined. This has recently been used to identify intermediates in order to infer assembly mechanisms in polyoxometallates.[13] ESI-MS is potentially very powerful for the characterization of suitably stable inorganic species especially when corroborative techniques are used (Figure 2). There are several drawbacks to using this technique for the investigation of inorganic nanoscale species with more dynamic speciation such as hydroxy-bridged aqueous clusters. Due to the low concentrations necessary for this measurement the species being investigated may not represent the species present at the higher concentrations relevant to materials scientists. In addition, this technique can lend itself to over interpretation due to the copious amounts of data that can be gathered from fragmentation patterns. Caution should be taken when applying information on charged particles in the gas phase to solvated inorganic nanoscale species.[14] These issues may be mitigated with complementary ***core*** and ***solvation sphere*** measurements.

     Dynamic Light Scattering (**DLS**) allows indirect measurement of the ***solvation sphere*** of a species by measuring changes in Rayleigh scattering. DLS uses the time dependent scattering intensity fluctuations to measure the same Brownian motion as DOSY NMR making them ideal corroborative techniques. DLS can determine the size and polydispersity of an inorganic nanoscale material and does not require the use of potentially expensive deuterated solvents. Many of the disadvantages of DLS result from the intensity weighing of the measurement. This means that the technique is biased to larger particles with more scattering. As a result, detection limits are inversely proportional to the size of the object being analyzed, and the largest objects in solution dominate the signal from samples with multiple populations.[15] DLS has a major

limitation in studying metal nanoparticles when the wavelength of the laser excites the surface plasmonic resonance (SPR). For instance, gold's SPR absorbance overlaps with the wavelength of the green laser at 532 nm in some DLS instruments, reducing signal to noise. This can easily be resolved by choosing a different wavelength of laser, but finding a second instrument is not always an easy task and purchasing a second laser is costly. DLS instruments can also be used to measure zeta potential. The zeta potential is a way of characterizing the surface charge of the solvation sphere in a given solvent system.[16] This can then be related to the relative stability of the particles in the solvent of choice.

UV-Visible Spectroscopy (**UV-Vis**) provides information about the wavelengths of light that a species absorbs. For inorganic cluster chemistry UV-Vis can provide information about the coordination of the atoms within a cluster. UV-Vis can also measure absorbance caused by the SPR of electrons in the metal core of a nanoparticle. This absorbance can be used indirectly to calculate the ***core*** size of metal nanoparticles and quantum dots, which can be corroborated by SAXS.[17] This also provides a handle for determining concentration, as well as, changes in speciation over time. However, this technique is limited to inorganic nanoscale species that absorb in the wavelengths of light accessible to the spectrometer. This is particularly well suited for the measurement of metal nanoparticles with a SPR in the visible range or clusters composed of transition elements because of well-known excitations involving d-orbitals. This limits the utility of the technique for main group elements containing closed d shells.[10]

Infrared (IR) **and** *Raman spectroscopy* are techniques that can be used to complement the determination of size by providing structural information about a molecule based on rotational and vibrational frequencies. By using them in tandem, scientists are able to characterize both the symmetric and asymmetric vibrational modes

of bonds in inorganic species in the solid and solution phases. Although IR is the less expensive and more common technique, it is essentially impossible to collect usable data in aqueous solutions. This is due to the large dipole moment of water that causes an enormous signal across the entire spectrum. Useful IR data can be collected in an array of other solvents including alcohols and organics. On the other hand the Raman spectra are clearly visible in water, because water is not readily distorted by an external electric field (polarizability). IR and Raman cannot be used to identify inorganic species directly unless there are analogs in the literature. To assign vibrational modes in molecules with no literature precedence, high-level computations are necessary. These complementary techniques are best used to study the solution dynamics, formation, and exchange kinetics of a species that has been identified and characterized in solution. By using these techniques on inorganic nanoscale species one can gain structural information by characterizing the vibrational modes, as well as, study kinetics and dynamics of the inorganic species in solution.[1,10]

Multiple Techniques Provide More Detailed Information

The understanding of the dynamic behavior of inorganic nanoscale species in solution is rapidly evolving, and a gap exists in relating solid-state and solution structures. As a result, the literature tends to report size measurements in an inconsistent manner and rarely provides detail about which dimension is being defined. For inorganic nanoscale species the ***core*** can describe different size aspects. For instance, "core" could describe the metal core of a ligand-stabilized nanoparticle or the kinetically stable covalently-bonded metal hydroxide/oxide portion of aqueous clusters or even the coordination network surrounding the hollow core of cage clusters (Figure 3). For solvated

43

species the **shell** comprises either well-defined organic capping ligands or tightly

associated counter ions of an inorganic cluster. The **_outer solvation sphere_** of all of

these species includes organized solvent and will be related to the solvent of choice. In

much of the literature that reports size, these distinctions are often overlooked.
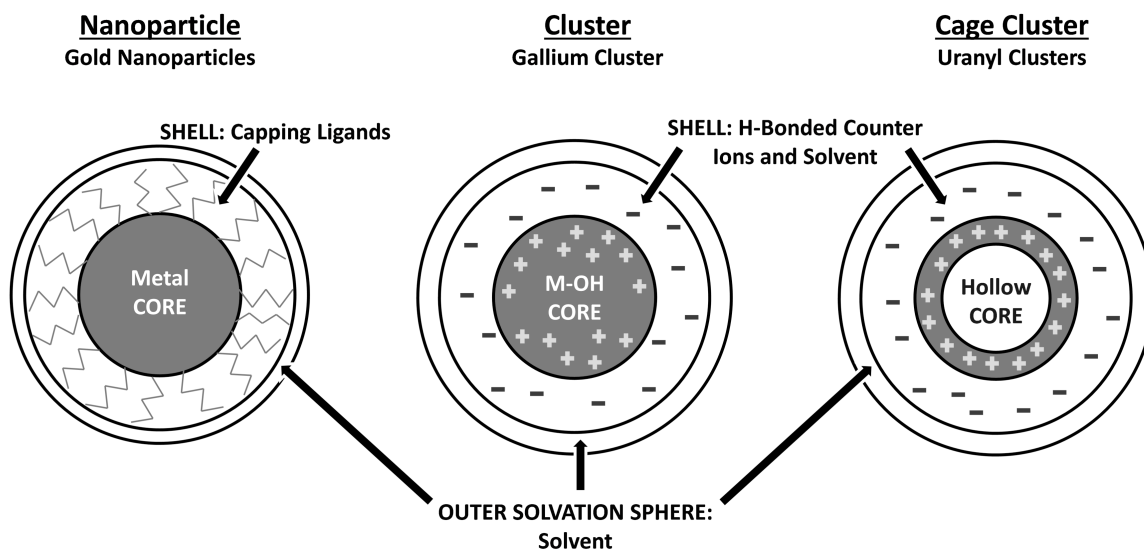
Figure 3. Schematic diagram relating the various layers of inorganic nanoscale species to the generic regions referred to as the **_core_**, **_shell_**, and **_outer solvation sphere_**. Each of these examples is further explored in the case studies presented.

Starting from the outside, the **_outer solvation sphere_** can be probed by

techniques measuring the diffusion of the stable inorganic nanoscale species in solution

such as DOSY and DLS (Figure 4). By varying the solvent system, changes in solvation

can be probed. By identifying a weakly interacting solvent this diffusion information can

also be used to approximate the outer dimensions of the **_shell_**. SAXS data can be

modeled to provide core size and volume or thickness of a cage cluster. By subtracting the

core size from the ***shell*** or ***outer solvation sphere*** dimensions, thicknesses and volumes of these regions can be calculated.

These types of inorganic nanoscale species represent examples of the need to use complementary characterization methods. More information can be gained by combining multiple techniques and using iterative investigations to observe dynamic behaviors in solution. The authors have chosen three examples that exemplify this approach in practice.

Observing Ga₁₃: More Complex than a Disappearing Spoon

Similarly to the Ga_7In_6 example, $Ga_{13}(\mu_3\text{-}OH)_6(\mu\text{-}OH)_{18}(H_2O)_{24}]\text{-}(NO_3)_{15}$ (**Ga₁₃**) can be used as a precursor to make high quality Ga_2O_3 thin films.[2] Until recently, very little was known about the existence or stability of this cluster in solution. Johnson, Hutchison, and co-workers were recently able to observe **Ga₁₃** in solution via ^{1}H-NMR in the non-exchanging solvent d_6-DMSO.[18] With no literature precedence it was impossible to confirm that the ^{1}H signals observed in the spectrum belonged to the bridging hydroxo and capping aquo ligands of the cluster. After acquiring a DOSY spectrum with a corrected diffusion coefficient of $0.955 \times 10^{-10} \pm 0.064 \times 10^{-10}$ m^{2}s^{-1} in d_6-DMSO, a hydrodynamic radius of 11.2 ± 0.8 Å was assigned to the species in solution (Figure 4). This alone was not sufficient evidence to confirm the existence of **Ga₁₃** in solution because the radius is significantly larger than a cluster in the solid-state. However, SAXS data indicated a core radius of 5.5 ± 1.5 Å in solution, which corroborates the size measured in the solid-state via single crystal XRD (r = 5.6 Å). Thus, we were able to confidently report that **Ga₁₃** is stable in DMSO at a concentration of 2 mM.
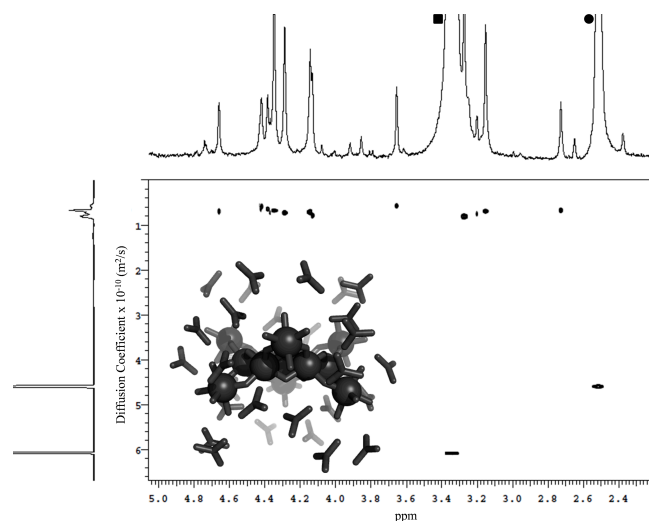
Figure 4. Representative ^{1}H-DOSY NMR spectrum of a 2mM sample of **Ga₁₃** cluster in d₆-DMSO (■) H₂O peak and (●) DMSO peak.

This confirmation allows for more complex studies to be initiated. Currently we are studying **Ga₁₃** in the solid and solution phase via Raman spectroscopy.[19] This research indicates that the cluster observed in solution has significantly different vibrational characteristics than the solid. These results support previous hypotheses that the clusters are very dynamic in solution. Using comparisons between NMR, Raman, SAXS, and DLS we seek to learn about the growth, stability, degradation, and aggregation of this cluster in solution. We hope to gain information on the mechanism of cluster formation and the pathway by which **Ga₁₃** becomes a thin film.

Probing Nanoparticles: Worth More than Their Weight in Gold

Gold nanoparticles (AuNPs) are of continued interested due to their unique size-dependent optoelectronic properties. Characterization of these materials can be challenging as they are often polydisperse which complicates measurement. While high

46

vacuum techniques such as TEM are effective in determining the core size and polydispersity, the low number of particles sampled makes statistically significant population characterization difficult. In addition, there are concerns over the effect that sample preparation may have on the nanomaterials analyzed. Hutchison and co-workers have synthesized and isolated a well-defined particle with the formula $Au_{11}(PPh_3)_8Cl_3$ (**Au-11**).[7]

Early investigations into the properties of **Au-11** led to the comparison and corroboration of TEM measurements with synchrotron SAXS data (Figure 5). The ability to perform these experiments with a lab scale SAXS followed and characterization was further corroborated with single crystal XRD.[7] While these experiments are a powerful way to confirm the stability of these nanoparticles in solution, they are only able to determine the size of the gold core. There have been conflicting reports in the literature about the solvation sphere of monolayer protected AuNPs. Early studies of AuNPs using DOSY NMR demonstrated the interdigitation of the ligand shell with neighboring particles when at high concentrations.[20] Other research groups have proposed that alkane thiol protected AuNPs in organic solvents may diffuse at a rate equivalent to the gold core alone.[21] This raises significant questions about the nature of solvated ligand-protected AuNPs.

In order to elucidate the behavior of the ligand shell, current studies aim to measure the effect of solvent interaction with these classes of AuNPs. Monodisperse particles with sharp NMR signals such as **Au-11** enable the use of DOSY to determine the hydrodynamic radius, which we will discuss in more detail in a subsequent paper.[22] By varying the solvent and then complementing the measurement of the hydrodynamic

47

radius using DOSY with the determination of the core size by SAXS we aim to uncover

information previously unavailable about the nature of the ligand shell.
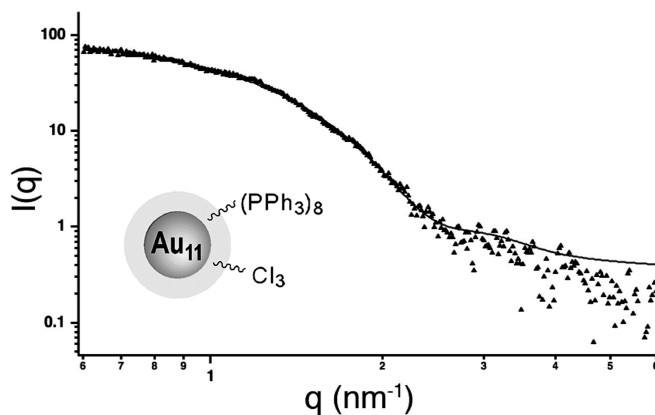
Figure 5. Schematic of $Au_{11}(PPh_3)_8Cl_3$ and SAXS scattering pattern from steady state flow measurements performed at the Advanced Light Source.[7]

Depleting the Controversy Around Clusters Containing Uranium: A Glowing Review

Widespread interest in the remediation of spent uranium fuel and other waste

products has spurred recent research into the controlled growth and speciation of uranyl

clusters. Under appropriate conditions the Burns group has shown that uranyl salts form

cage compounds including self-assembled core-shell clusters with fullerene topology.[23–26]

Single crystals were isolated of a variety of these cage clusters including compounds with

oxalate, pyrophosphate, and peroxide bridging ligands. SAXS data were collected and fit

to a core-shell model allowing for the determination of the inner and outer dimensions of

the cage cluster confirming the persistence of these species in solution. To follow the

growth of these cage clusters in solution, ESI-MS and SAXS were used in tandem to

measure the molecular weight and size of the species in solution over time. ESI-MS

suggests that one of the isolated cluster fragments forms within an hour of mixing. After 15 days the desired fullerene-like core-shell structure begins to form, a full 16 days before crystal formation! At the time of crystallization, ESI-MS showed that the solution still consists of a mixture of species.[23] However, these data alone are not sufficient to fully describe the growth of the clusters for the reasons outlined above. To bolster the ESI-MS findings, SAXS was used to follow the maximum vector length of particles in solution as a function of time. SAXS revealed a nearly linear increase in size from the initial cluster fragment to the final core shell structure (Figure 6).
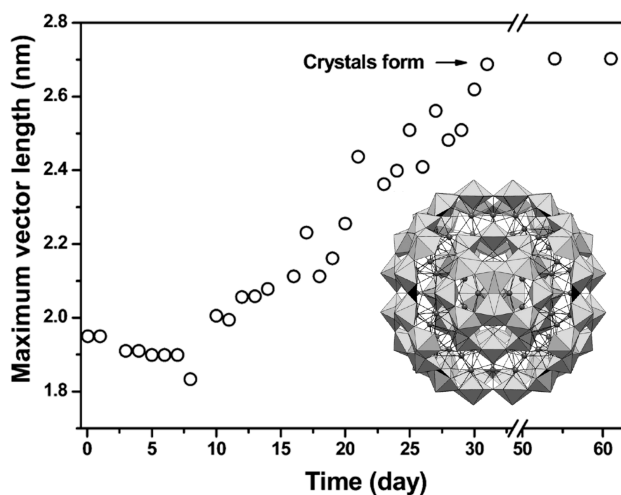
Figure 6. Structure of a uranyl cage and cluster growth monitored by SAXS in solution. Adapted with permission from J. Qiu, J. Ling, A. Sui, J. E. S. Szymanowski, A. Simonetti, P. C. Burns, *J. Am. Chem. Soc.* **2012**, *134*, 1810–1816. Copyright (2012) American Chemical Society.

In a recent collaboration between the Burns and Casey labs, the structure and reaction dynamics of the pyrophosphate cage cluster[26] in solution were studied using ^{31}P DOSY to obtain information about the hydrodynamic radius.[27] By using ^{31}P instead of ^{1}H DOSY the issues associated with solvent and proton exchange are eliminated. Studies

of this type allow for the characterization of these inorganic nanoscale species in water, the solvent most pertinent to their potential applications in the environment. This demonstrates a potential expansion of this combined technique to a wider variety of materials.

Conclusion

While there are a number of techniques available to determine the size of inorganic nanoscale species, the dimensions measured are often misrepresented. By recognizing that these techniques measure different dimensions, a complementary approach can be utilized to map out the ***core***, ***shell***, and ***outer solvation sphere***. Solid-state techniques can be used to characterize the core and shell of a material isolated from solution. To confirm that the relevant species in solution is the same as the solid-state structure, related dimensions of the species must be measured in solution to corroborate the solid-state data. Once this has been verified, additional techniques can provide a wealth of information. The ability to confirm and observe these inorganic nanoscale species in solution is the essential first step towards the understanding of dynamic behavior. This allows inorganic, materials, and geological chemists to perform more complex investigations to determine the mechanisms of formation, pacification, degradation, polymerization, and aggregation of nanoscale species.

Bridge to Chapter III

Addressing the challenge of nanomaterial definition is necessary for each stage of nanomaterial development. The design of a nanomaterial will inform the type of purification performed as well as the choice of characterization methods employed.

During the discovery phase of new materials corroborative methods are required in order to maximize the information output of each individual technique. Finally, as functional nanomaterials are developed experimental probes may be considered as functional assays for material properties, such as the demonstration of catalysis in Chapter V. Judicious choice of characterization techniques during experimental design has also been shown to address the nanomaterial characterization bottleneck. These benefits were illustrated during the development of a direct microfluidic synthesis of functional gold nanoparticles described in Chapter IV.

CHAPTER III

SIMULTANEOUS CONTROL OF LIGAND FUNCTIONALITY

AND CORE SIZE DURING DIRECT SYNTHESIS OF 2-10 NM

WATER-SOLUBLE GOLD NANOPARTICLES

Note: Material in Chapter III was submitted for publication in the journal Nano Letters in April, 2014. Patrick M. Haben contributed substantially to this work by assisting in experimental design, manuscript editing, nanoparticle batch syntheses and reproducibility studies. In addition, I contributed to optimization of reaction conditions and the microfluidic flow reactor, nanoparticle synthesis and characterization. James E. Hutchison was the principle investigator for this work and provided experimental and editorial guidance.

Multifunction nanoparticles with well-defined structures are key nanomaterials for fundamental studies and applications that require (1) specific control of optical or other properties through tuning of core size and (2) interfacing (e.g. chemical targeting or biocompatibility) through control of the ligand shell. Deliberate control of core and surface composition/structure is essential in a wide range of applications from biomedicine and toxicology to nanoelectronics and catalysis. For example, recent interest has been directed towards the diagnosis and treatment of cancer as targeted contrast agents for CT imaging[7,8] and as agents for chemotherapy, hyperthermic therapy and radiotherapy.[9,10] In these applications both the optoelectronic properties and the fate and transport *in vivo* depend strongly on the nanoparticle size and functionality.[11,12] A recent study by Oh et al.[13] showed that for small oligoethyleneglycol-functionalized AuNPs, particle diameter greatly influences localization to various cellular compartments.[14] The

smallest AuNPs, d_{CORE} = 2.4 nm, localized to the nucleus, while 5.5 and 8.2 nm AuNPs localized to the cytoplasm, and 16 nm AuNPs did not enter the cell.

Ligand-stabilized gold nanoparticles (AuNPs) are being widely investigated[1-5] because access to different core sizes is relatively straightforward and the surfaces can be modified with covalently anchored monolayer films. However, it remains challenging to simultaneously control both the core and surface attributes despite considerable effort to develop syntheses of thiolate-stabilized gold nanoparticles.[6] Specific structural variants are often difficult or impossible to prepare and the preparation of each new structural variant typically requires a considerable amount of trial and error to identify conditions that lead to the desired size and coating.[2] Here we describe a systematic approach to rapidly develop reaction conditions that produce water-soluble, functionalized AuNPs with specifically targeted core sizes over the range of 2-10 nm.

The challenge to attaining simultaneous control over both targeted core size and ligand functionality is the strong influence of ligand functionality on the resulting core size during synthesis. Although two-step synthetic methods involving core formation followed by ligand exchange have shown success,[2,15-17] each additional synthetic step adds complexity and introduces the potential for persistent impurities such as unexchanged ligands or surfactants.[2] Thus, a direct (single-step) process to produce this range of targeted materials would minimize complexity if the core size and surface coating can be independently controlled during synthesis.

Typical syntheses for sub-10 nm AuNPs are limited in the range of accessible core sizes and functionalities available, involve multiple steps, and/or utilize toxic surfactants during particle formation. In the well-known biphasic Brust preparation, 2-8 nm particles are synthesized with organic soluble ligands in the presence of tetraoctylammonium

53

bromide.[18] Ligand exchange is necessary to obtain water-soluble particles from this synthesis. Unfortunately, these exchanges are often time-consuming,[2,16] incomplete,[19-21] and may alter the core size of the particles.[4,15] To circumvent these issues, single phase methods were developed; however the size range available is further restricted to 1-4 nm.[22] Oh, et al.[23] employed specialized dithiol binding functionalities and large polymeric ligands to produce AuNPs over the range of 2-20 nm, utilizing ligand / gold ratio to control the core diameter.

In the examples above, size is controlled by adjusting the ligand / gold / reducing agent ratio,[24] however the size range available is typically constrained. In addition, the use of specialized ligands limits the types of functionality that can be introduced. We reasoned that it might be possible to control the reaction kinetics, and thus core formation, by taking advantage of the different reduction potentials of the Au(III) species that result from pH-dependent hydrolysis of $HAuCl_4$.[25,26] Initial attempts using this approach in the presence of thiol or disulfide ligands resulted in no significant variation in NP diameter (Figure S31), perhaps owing to the strong surface passivation of these ligands. Recent reports have demonstrated that AuNP diameter depends upon the Au(III) speciation in the presence of a weakly-passivating ligands such as citrate or benzenesulfonate.[25,26] Thus, we explored the use of alkyl thiosulfates (Bunte salts) to control size through pH variation of the Au(III) solution while introducing desired functionality. Bunte salts are known to passivate the NP core weakly during nanoparticle growth, yet produce strong covalent linkages to the final AuNPs.[27-30].

Specifically functionalized AuNPs with core sizes ranging from 2 to 10 nm can be easily prepared using this strategy. AuNPs were synthesized with three different Bunte salt ligands* in batch conditions. A Bunte salt, $HAuCl_4$ and $NaBH_4$ were combined (in a 1 : 5

: 2 ratio) in a round bottom flask stirred at moderate speed. $NaBH_4$ was added to the flask first, followed by Bunte salt solution, and finally $HAuCl_4$. Prior to addition, NaOH was added to both the $HAuCl_4$ and $NaBH_4$ solutions. The base added to the $HAuCl_4$ solution controls the Au(III) speciation and thus AuNP size (Supporting Information). Base was added to the $NaBH_4$ solution to maintain the same final pH between batches.

Increasing the pH of the Au(III) solution produced larger particles as indicated by a shift in the plasmon λ-max in the UV/visible spectra.[31] (Supporting Information). There appeared to be differences in the AuNP size dependence on pH when using different Bunte salt ligands, but the qualitative nature of optical spectroscopy and batch-to-batch variation precluded drawing definitive conclusions. Understanding this dependence on pH required quantitative size analysis, good reproducibility, and high throughput of synthesis and analysis.

In order to quantify how the size depends upon pH, TEM and small-angle x-ray scattering (SAXS) measurements were performed.[32-34] TEM analysis confirmed that the particles were spherical but proved to be too time-consuming for size determination of the many experimental replicates.[35] To avoid the possibility of deposition effects and poor statistical significance due to the small number of particles sampled by TEM, SAXS was used for determination of the AuNPs size distribution. A comparison of size determination by SAXS and TEM verified that SAXS model fitting is a viable approach to overcome these challenges.[33] SAXS analysis made it possible to rapidly (within minutes) analyze the nanoparticles in solution and allowed us to quantify the batch-to-batch variation in AuNP core size.

When different researchers performed these syntheses, this variability was as high as 18% (Table S4). When a single researcher performed multiple syntheses in succession,

55

the variation in AuNP core size was reduced to 5%. To further reduce this variation, we implemented flow based syntheses because such approaches have been shown to reduce polydispersity as well as improve reproducibility between batches.[38] The use of a microfluidic reactor (Figure 1) to control reagent addition and mixing rates significantly reduces variation between batches,[38] to less than 2%, even when performed by different researchers.[33,39,40]
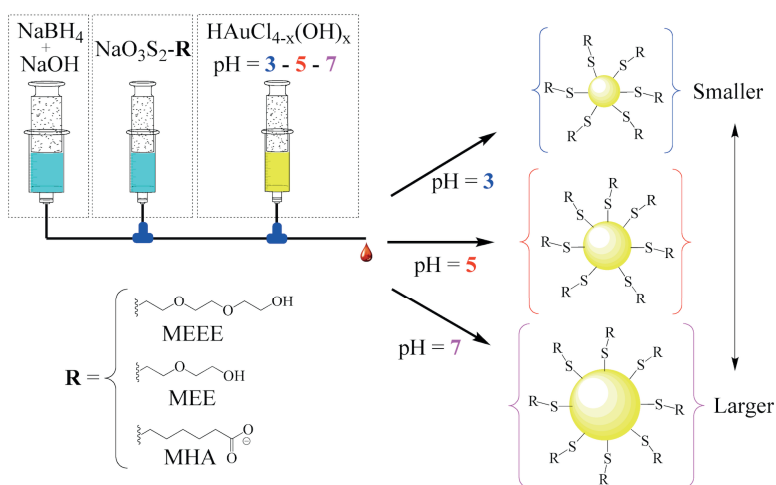
Figure 1. Synthesis of thiolate-passivated Au nanoparticles using a selection of Bunte Salt ligands in a microfluidic reactor. Three ligands used to examine this reactivity are illustrated in the figure. Adjustment of the pH of the Au (III) solution produces NPs with targeted core diameters.

Syntheses were performed in the microfluidic reactor at a flow rate of 60 mL/min using identical reagent ratios as the batch syntheses described above. The solutions were delivered by syringe pumps and mixed in Tefzel T-mixers connected by FEP tubing. To minimize loss of material to plating within the reactor, the flows of borohydride and ligand solutions were initiated prior to introducing the gold salt solution. In a typical synthesis, 8 mL of 5.0 mM HAuCl$_4$, 10 mL of 1.0 mM Bunte Salt ligand, and 20 mL of

1.0 mM NaBH$_4$ are used for a total reaction volume of 38 mL. To control the Au(III)

speciation, NaOH was added to achieve a given salt solution pH. An appropriate amount

of base was also added to NaBH$_4$ solutions so that the final pH of each reaction was the

same. Details of synthetic procedures are provided in Supporting Information.

Combining the improvements from microfluidic reactor and automated SAXS

analysis, we rapidly generated AuNPs with uniform, reproducible core sizes (Figure 2).

There is a smooth, non-linear trend in AuNP core size as the pH of the Au(III) solution is

scaled from ~ 3 to 7. From pH 3 to 5, a gradual increase in AuNP core size is observed. A

more rapid rise in the slope of this trend occurs as the pH is increased, with the steepest

slope observed as the pH approaches 7. The observed trend appears to correlate with the

changing speciation of the Au(III) salt from HAuCl$_4$ to HAuCl$_{4-x}$(OH)$_x$ and finally to

HAu(OH)$_4$ as pH increases. Multiple species co-exist at each pH (Figure S30).[26] The

reduction potential of the Au species is most positive for the tetrachloro species and

decreases as each chloride is substituted by a hydroxo ligand.[26] Greater substitution by

hydroxo ligands decreases the rate of reduction and, consequently, increases the final

AuNP core size. The change in the observed sizes correlates to the changes in Au(III)

speciation across the measured pH range.

This synthetic method affords the ability to incorporate specific functionality on

the AuNP surface while simultaneously maintaining control over core size. The NP size

and surface chemistry were characterized using a complementary suite of analytical

techniques[41] described in detail in the Supporting Information. Briefly, XPS of the S2p

region indicates the ligands are bound as thiolate, while TGA mass loss is consistent with

a fully formed monolayer on the gold surface. Collectively these data indicate that the

particles are thiolate-stabilized AuNPs. The particles exhibited long term (> 3 months)

stability in solution as well as stability during diafiltration, lyophilization and resuspension.[27-30] In a typical synthesis 6.25 mg of purified lyophilized nanoparticles are obtained, representing a 73% yield of gold used per batch. In addition, yields can be improved by reclaiming nanoparticles lost through nonspecific adsorption to the diafiltration membrane by flushing the membrane with 0.1 M NaOH.
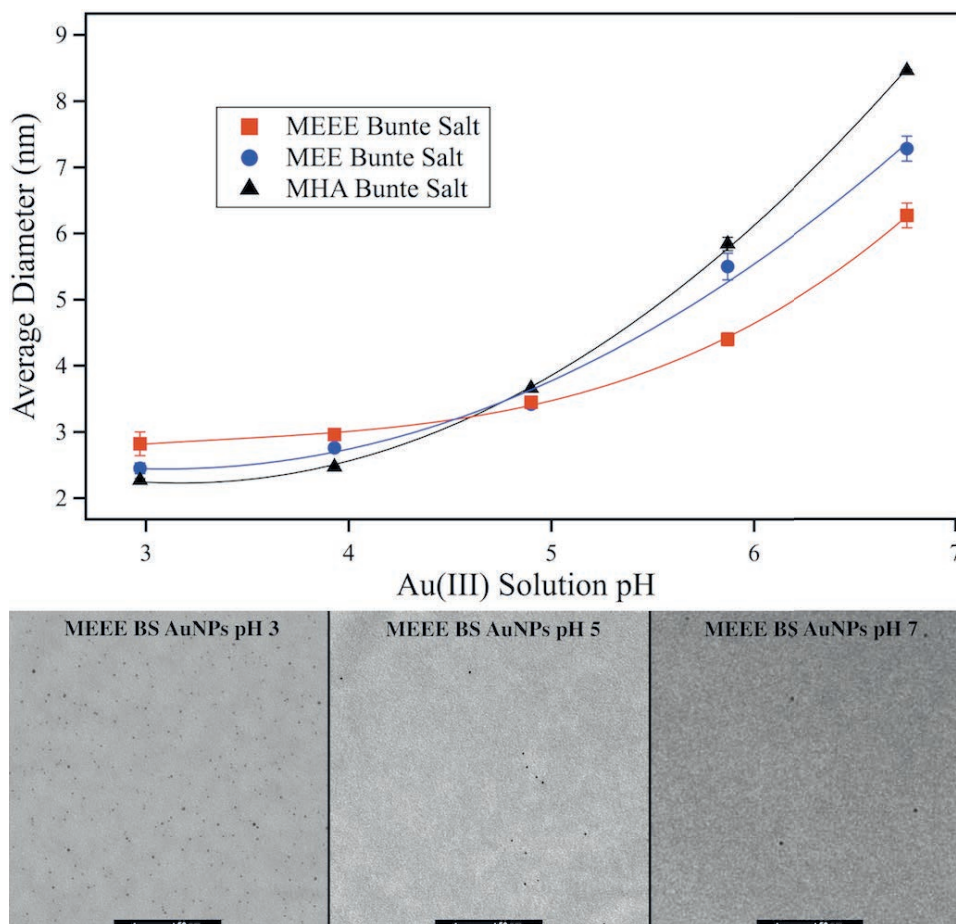
Figure 2. Average AuNP core diameters determined by small-angle x-ray scatting (SAXS) analysis synthesized in a microreactor system using different Au(III) solution pHs. TEM micrographs serve to verify particle circularity and uniformity to confirm the validity of the SAXS model. Each data point is the average of at least three synthetic runs. The traces connecting the points serve as guides to the eye and illustrate the non-linear dependence of the size on pH for each different ligand.

There is a different dependence of size on the pH for each of the three ligands examined in this study. At the highest pH, under the same reaction conditions, the identity of the ligand produces a change of over 2 nm in the core size. These findings are consistent with previous observations that ligands influence core growth during synthesis. In addition, at the extremes of pH, the dependence of size upon ligand type is reversed. At low pH, MEEE produces the largest NPs, whereas at high pH, MHA produces the largest cores. The combination of the ligand and pH effects upon core size makes it impossible to predict a priori what conditions are needed to produce a functionalized AuNP with a defined core size.

Given the smooth trend of particle sizes as a function of pH, we examined whether a continuous curve drawn through these points (a working curve) could be used to generate AuNPs with targeted core sizes.[†,42,45] These are particularly useful when describing complex trends or when mechanistic understanding is limited. Here the curves could be used to predict the pH needed to produce a particle with a specific core size for a selected ligand.

Given the interest in producing functionalized particles with defined core sizes, we tested the utility of the working curve shown for MHA in Figure 3 by attempting to synthesize 3.0, 5.0, and 7.0 nm functionalized AuNPs. From the working curve, we determined the appropriate Au(III) solution pH for the targeted core sizes and then synthesized AuNPs at each of these conditions through addition of NaOH to the Au(III) solution (Table S3). Size distributions determined by SAXS show that these syntheses produced AuNPs with diameters of 3.0, 4.9 and 6.9 nm respectively, with < 1% average variation in size between three runs. Each synthesis produced core diameters within 3% of targeted value. It was possible to target specific nanoparticle sizes for each of the

ligands used in this study (Supporting Information). These results suggest that the working

curves are descriptive of the trend in AuNP size vs. Au(III) solution pH, and facilitate

targeted synthesis of AuNPs across a continuous size range.
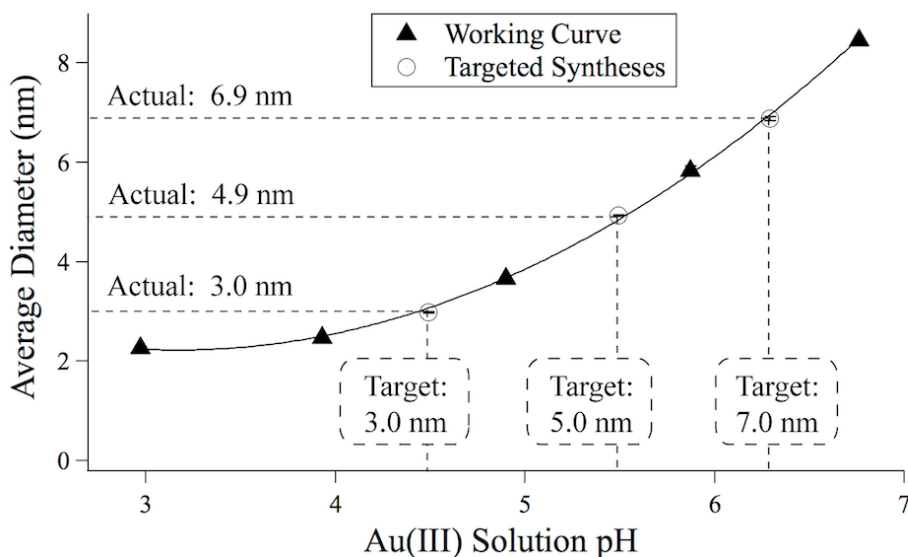
Figure 3. A working curve, fitted to the observed size data (using MHA Bunte salt ligand) guided the synthesis of AuNPs of a desired core diameter. Using the working curve to determine appropriate pH values for the Au(III) solutions, three particle sizes were targeted and synthesized within 3% of desired diameter.

The direct synthetic method described here utilizes systematic control of Au(III)

speciation using a variety of Bunte salt ligands targeting AuNP core sizes while

independently tailoring functionality. This is the first work to utilize Au(III) speciation as

a method for controlling the size of covalently-passivated AuNPs. The use of a

microfluidic reactor facilitated rapid, more reproducible syntheses compared to batch

reactions while an autosampler-equipped SAXS instrument provided rapid analysis of

AuNP core size as-synthesized.[33,35,44] Future studies that require specific nanoparticle core

sizes with different ligand shell functionalities should benefit from this method.

Bridge to Chapter IV

The microfluidic syntheses performed in Chapter III were a product of several rounds of optimization of reagent amounts, flow geometry and mixing. These advances afforded the ability to reproducibly synthesize functionalized nanoparticles that were stable across a wide range of conditions. In addition, the direct synthesis demonstrated here afforded nanoparticles that could be synthesized and purified very rapidly, aiding in subsequent investigations. All of these properties presented the possibility of capitalizing on this method for the design of functional nanoparticles that could be readily used as chemical reagents in subsequent reactions.

One challenge that remained was adapting the direct microfluidic synthesis for the production of mixed monolayer nanoparticles. An ideal nanoparticle reagent would make use of a mixed ligand shell to impart enhanced solubility and stability along with varying amount of additional functionality for the specific goals of a given application. The nanoparticles described in Chapter IV are the product of addressing these challenges and demonstrate the applicability of the design parameters uncovered in this chapter to other functional systems.

Notes

* Positively-charged nanoparticles were produced using this method; however, 100% positively-charged ligand shells yielded unstable particles susceptible to flocculation. This functionality was integrated in the ligand shell by including neutral diluent ligands during synthesis.

† Note that working curves are often used in analytical chemistry to describe empirical relationships between parameters.

CHAPTER IV

RAPID DIRECT SYNTHESIS OF WATER-SOLUBLE, MIXED MONOLAYER,

AZIDE FUNCTIONALIZED GOLD NANOPARTICLES

FOR USE AS CLICK CHEMISTRY REAGENTS

Note: Portions of Chapter IV are expected to appear in an upcoming publication co-authored with Zachary C. Kennedy, Zhenshuo Feng and James E. Hutchison. I designed the experiments and composed the manuscript corresponding to Chapter IV. In addition I performed the nanoparticle syntheses, purification, characterization by SAXS and fluorescence. Zachary C. Kennedy contributed substantially to the synthesis of functional ligands, NMR studies and aided in preparation of the manuscript; Zhenshuo Feng aided in ligand synthesis and click coupling reactions with AuNPs. James E. Hutchison was the principle investigator for this work and provided experimental and editorial guidance.

Functionalized monolayer protected nanoparticles are of interest in biomedical applications ranging from targeted contrast agents for imaging[1], to drug delivery[2] and sensing.[3] The current limitations of this class of materials is not related to their properties, but rather their cost / benefit ratio and reliable control of composition and structure.[4,5] Typically, a synthesis must be individually tailored to produce nanoparticles that possess the core and surface functionality needed for each application. An ideal nanoparticle building block (or reagent) would possess the desired core and stabilizing/solubilizing ligand shell, yet could be readily coupled to more complex building blocks to produce hybrid nanomaterials. This approach would be analogous to convergenet syntheses in organic chemistry where one uses a parallel convergent synthesis rather a linear strategy. Water-soluble AuNPs with terminal azides provide a stable versatile platform for further modification using the azide-alkyne cycloaddition (AAC) click reaction.[6]

To address the synthetic challenge of creating a clickable nanoparticle reagent we aimed to adhere to the stringent criteria set forth by Sharpless when he coined the concept of click chemistry. When one considers applying these concepts to the design of functional nanomaterials, merely the presence of reactive groups is not enough. Additionally, the entire synthetic process ought to be rapid, efficient, modular, use readily available starting materials, use only benign solvents, be insensitive to air and water and do so in high yields while only requiring simple non-chromatographic techniques for purification and isolation.[6]

To date, there have been several approaches for the production of azide functionalized AuNPs. Large (14-15 nm) citrate stabilized AuNPs[7] were prepared and the citrate exchanged with a thiolate ligand containing ω-azide functionality[8,9]. Click coupling was demonstrated, but inefficient, converting only 0.3% of the azide groups.[8] Several groups employed smaller (2-3 nm) AuNPs synthesized by the Brust-Schiffrin method.[10,11,12,13,14,15] In two cases,[10,11,12,14,15] hydrophobic alkane thiol-stabilized particles are first prepared, subjected to a time consuming ligand exchange, followed by a substitution reaction to introduce azides. This sequence of reactions takes approximately one week from start to finish. It was necessary to couple dendritic PEG chains to the terminal azides to impart water-solubility.[12] Workentin employed methyl terminated tetraethylene glycol thiols to produce water soluble AuNPs that must be exchanged with a ω-azide containing thiol. This process requires extensive washing with organic solvents to remove excess ligand.[13] In our hands similarly functionalized AuNPs could be suspended in water, but not without flocculation. Heroic efforts were needed to tailor reaction conditions to increase coupling efficiency with these azide terminated particles required the use of stoichiometric amounts of Cu(I)[11] or development of a new catalyst[10]. Although

these approaches produced functional materials in AAC reactions, none of these examples can be said to adhere to the principles of click chemistry. We sought a new approach where these considerations were integrated into the design of the synthesis.

Herein, we demonstrate a direct synthesis, purification, and isolation of water-soluble AuNPs with tailored reactive group densities and small (< 5 nm) core diameters. The envisioned benefits of click chemistry lie in the use of readily prepared reagents to be used as modular building blocks. The primary design criteria of the azide functionalized AuNPs was water solubility, therefore the majority of the ligand shell is derived from the triethylene glycol terminated ligand which has the added benefit of biocompatibility.[16] A triethylene glycol azide Bunte salt (**EG₃-azide BS**) was used to introduce the reactive azide group because the identical tethering chain would afford comparable kinetics of incorporation into the ligand shell. We confirmed that the azide group is not reduced during nanoparticle synthesis under these mild synthetic conditions (in water at RT).[17] The direct synthesis method illustrated in Scheme 1 shows our approach to introduce a small amount of azide ligand within an PEG shell to ensure that the particles will be water soluble and azides are dilute enough for efficient coupling reactions.[15]

Azide functionalized AuNPs with a mixed monolayer ligand shell were prepared in a single step using Bunte salt ligand precursors in a microfluidic reactor previously described with minor modifications to allow for the incorporation of the second ligand type.[18] Although the direct synthesis of AuNPs with Bunte salt precursors is compatible with traditional batch reactions, the formation of AuNPs occurs rapidly and mixing has been shown to have an effect on system dynamics in these cases.[19] The microfluidic reactor affords excellent reproducibility (SD of core diameter < 0.1 nm) across multiple batches as well as low (< 15%) polydispersity of the AuNPs produced (†ESI Table Sx).

Through control of the pH of the gold precursor solution prior to reduction, it is possible to control the diameter of the AuNPs.[18,20] In this work 3.5 ± 0.4 nm AuNPs were prepared by using a precursor solution pH of 5. All AuNP samples were purified using tangential flow filtration[21] as described in the ‡experimental and isolated as easily redispersible powders following lyophilization. The AuNP reagent can be synthesised and purified within 2.5 h.
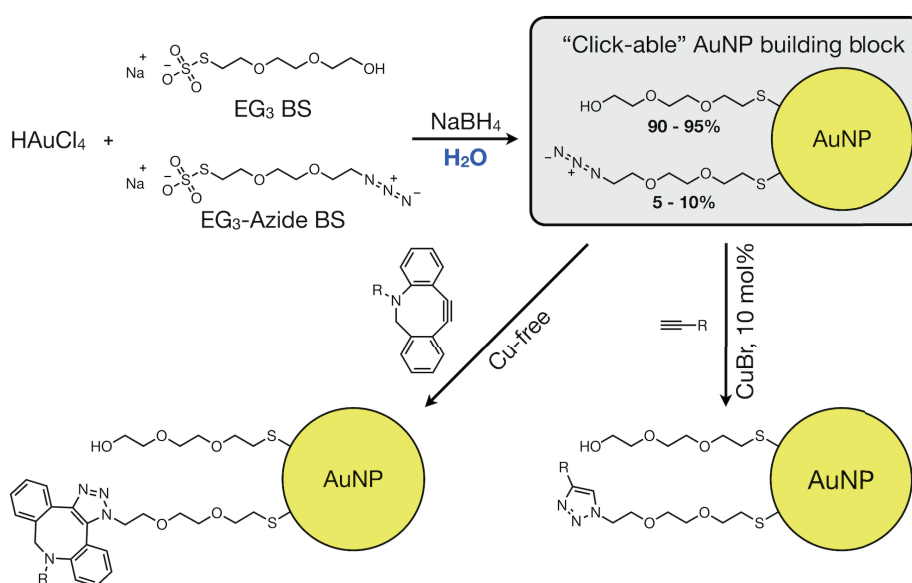
Scheme 1. Synthetic scheme for the direct synthesis of azide functionalized AuNPs and subsequent functionalization using the Cu-free or Cu-catalyzed Azide-Alkyne Cycloaddition (CuAAC) reaction.

To verify that the composition of the AuNPs ligand shell mirrors the feed ratio of ligands used we first synthesized AuNPs with 10% of the EG$_3$-azide BS and 90% of the EG$_3$ BS diluent ligand (**EG$_3$-azide/EG$_3$ (10:90)-AuNPs**). The composition of the AuNP ligand shell was determined by I$_2$ decomposition and subsequent NMR analysis and found to be comparable to the ratio expected from the feed ratio (†ESI Figure Sx). To maximize the efficacy of AAC reactions and further improve water solubility of click

65

products all subsequent investigations were performed using AuNPs with 5% EG_3-azide and 95% EG_3 (**EG₃-azide/EG₃ (5:95)-AuNPs**).

To illustrate the reactivity of the azide functionalized AuNPs the strain promoted alkyne-azide cycloaddition (SPAAC) was first used. DBCO-PEG₄-Alexa545 (**1**) was chosen as a model reactant as the long PEG tether and terminal fluorophore provide a ready handle for the characterization of a successful click reaction. The fluorescent AuNPs (**EG₃-triazole-DBCO-1**, Figure 1a) were obtained by reacting 15.59 mg of **EG₃-azide/EG₃ (5:95)-AuNPs** with 3 eq. of DBCO-PEG₄-Alexa545 in 2 mL of H_2O for 24 hours.
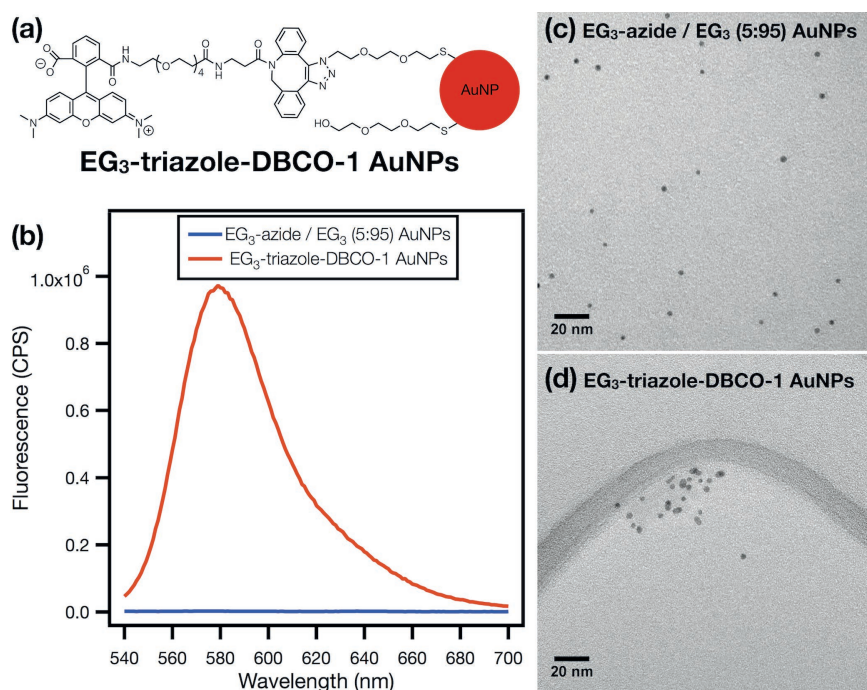
Figure 1. (a) The click product of **EG₃-azide/EG₃ (5:95)-AuNPs** and **DBCO-PEG4-Alexa545** (b) Fluorescence measurements of **EG3-triazole-DBCO-1 AuNPs** (c) TEM micrograph of **EG₃-azide/EG₃ (5:95)-AuNPs** (d) TEM micrograph of the click product **EG₃-triazole-DBCO-1**

The nanoparticle solution was then purified and isolated as a black powder as detailed in the ‡experimental. The complete removal of any unreacted DBCO-PEG$_4$-Alexa545 was verified by NMR, TLC and fluorescence measurements show that the coupling reaction was effective (Figure 1b). I$_2$ decomposition and further NMR analysis also showed the presence of the coupled product (†ESI Figure Sx). The reactant and product AuNP solutions were visualized by TEM under identical experimental conditions (Figure 1c-d). The behaviour of the nanoparticles as deposited is indicative of the change in surface chemistry following the coupling reaction. To avoid any ambiguity caused by deposition effects in TEM imaging, the size of the AuNPs were determined by SAXS.[22] Unlike TEM, SAXS can rapidly determine nanoparticle size information while in solution in high statistics, probing the bulk of the material analogous to optical measurements in solution. The azide functionalized AuNPs were found to remain stable, with the average core diameter of **EG$_3$-triazole-DBCO-1** (3.4 ± 0.7 nm) the same as **EG$_3$-azide/EG$_3$ (5:95)-AuNPs** (3.4 ± 0.4 nm) in contrast to other azide functionalized AuNPs.[10,12]

The versatility of these AuNPs was further shown by coupling to a variety of hydrophobic and hydrophilic moieties with alkyne functionalities (Chart 1) including organometallic species and a modified thymidine analog using low loadings (~10 mol%) of a simple copper catalyst (CuBr) in air. These included species that are of interest for electrochemistry (**5**) as well as those that could be used for biological imaging[23] (**7**) or coupling to biomacromolecules (**3**). In all cases, even when the incoming species was hydrophobic as is the case of (**6**) the AuNPs remained water-soluble, making the **EG$_3$-azide/EG$_3$ (5:95)-AuNP** reagent of potential interest for other biomedical applications such as the delivery of hydrophobic drug molecules.
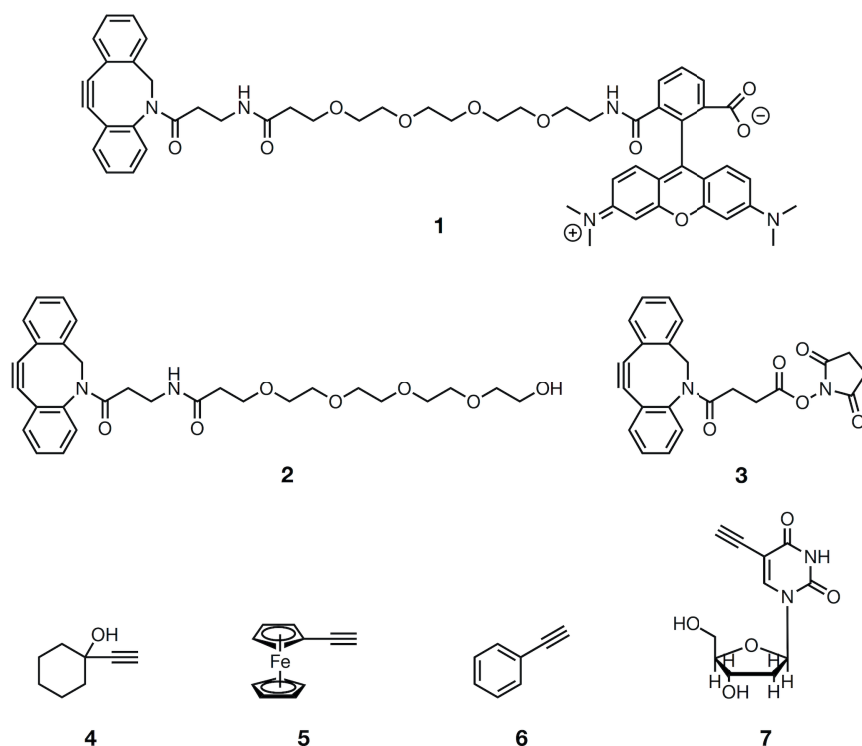
Chart 1. Alkyne containing species used to demonstrate the scope of the **EG$_3$-azide/EG$_3$ (5:95)-AuNPs** reactivity.

Conclusions

A single step direct synthesis of water-soluble, mixed monolayer, azide functionalized AuNPs was developed allowing for varied functional group density. These AuNPs were synthesized, purified, and isolated in high yield using only water as a solvent adhering to the stringent criteria of click chemistry. Further, the nanoparticles were amenable to both CuAAC and SPAAC reaction conditions, maintaining core diameter and water solubility making them ideal potential candidates for biomedical applications. Current studies are also underway investigating the use of these materials in the assembly of hybrid nanomaterials, especially in applications where stable, biocompatible nanoparticles are needed.

Bridge to Chapter V

The design of a AuNP reagent adhering to the principles of click chemistry built upon the advances in characterization of nanoparticles in solution, as described in Chapter II, along with improvements in reproducibility afforded by optimization of the micrcofluidic reactor used to perform the nanoparticle syntheses in Chapter III. The scalable syntheses developed for the production of functional nanoparticle reagents would be useful in the assembly of advanced nanomaterials for biomedical of sensing applications. However, these applications both harness properties of the nanoparticle ligand shell in addition to the nanoparticle core. Gold nanoparticle are also of interest for use as catalysts owing to unique size dependent reactivity. Although useful during synthesis for solubility as well as stability and obtaining a desired core diameter, in these applications the thiolate ligand shell proves to have deleterious effects on catalytic activity due to their passivation of the gold core. In these cases functionalized gold nanoparticles are still an attractive building block in the assembly of supported gold structures because ligand functionality can be designed to drive solution-based assembly. Chapter V describes a method of gently removing some of the ligands from supported gold nanoparticles while retaining nanoparticle stability. This approach further demonstrates some of the benefits of using monolayer protected gold nanoparticles as reagents in the construction of advanced nanomaterials.

Notes

‡ Experimental procedure: *Synthesis of **EG₃-azide/EG₃ (5:95)-AuNPs** and **EG₃-azide/EG₃ (10:90)-AuNPs:*** Mixed monolayer protected AuNPs with a core diameter of 3.5 ± 0.4 nm (by SAXS) were synthesized using our previous described microfluidic

reactor with minor modifications.[18] Briefly, aqueous solutions of each reagent were prepared in quantities to enable three successive syntheses using a single T-mixer. Thus, 1 mM stock solutions of EG$_3$ Bunte Salt and EG$_3$-azide Bunte Salt were prepared and used in a ratio of 27:3 or 24:6 depending on the desired AuNP monolayer composition, for a total volume of 30 mL. Then, 30 mL of 5 mM HAuCl$_4$ was prepared and 320 μL of 0.1 M NaOH was added raising the pH to 5. Finally, 505 μL of 1M NaOH was added to 60 mL of 1 mM NaBH$_4$. Reagents were mixed in Teflon T-mixers at a total flow rate of 60 mL / minute and the reaction mixture was purified using 30 volume equivalents of 18.2 MΩ water passed through a 10 kDa Pall Minimate tangential flow filtration capsule. The AuNPs were then isolated as a black powder following lyophilization before use in subsequent AAC reactions.

CHAPTER V

THE CONTROLLED REMOVAL OF THIOL LIGANDS FROM

SURFACE-CONFINED, MONOLAYER PROTECTED GOLD NANOPARTICLES

Note: Portions of Chapter V are expected to appear in an upcoming publication co-authored by Edward W. Elliott III, Richard D. Glover, and James E. Hutchison. I designed the high surface area support assembly and catalysis assay and developed the manuscript. Richard D. Glover developed the planar analysis platform and performed much of the XPS analysis; development of the ozone treatment apparatus and all other experiments were performed in collaboration. James E. Hutchison was the principle investigators for this work and provided experimental and editorial guidance.

Due to their size-dependent properties supported nanoparticles continue to find applications in hybrid functional structures. As more complex nanomaterials are developed for use in advanced applications[1] functional assemblies of gold nanoparticles (AuNPs) with unique catalytic activity[2,3] continue to garner interest as new selectivity is demonstrated but synthesis of functional materials has proved challenging.[2] Other recent applications of nanoparticles in renewable energy generation[4,5] emphasize the importance of carefully controlling particle spacing and core dimensions, as the optoelectronic properties of nanoscale metal are highly sensitive to changes in size.[6-10] There are several advantages to the use of functionalized monolayer protected nanoparticles as building blocks; careful synthesis affords the necessary size control before self-assembly, while the ability to tailor ligand chemistry allows for the directed attachment to a substrate. Although the use of ligands in synthesis and assembly provide many advantages the ligand shell is deleterious towards applications that aim to capitalize on the side

dependent properties of the core. It is particularly challenging to remove the ligand shell without changing the properties of the assembly through core growth and without loss of material from the support after assembly.[11] To address this challenge, we developed a mild chemical treatment that decreased the affinity of the ligand shell for the surface of the nanoparticle core. This facilitated the removal of ligands at room temperature to expose an active nanoparticle surface without compromising tethering to the support. Parallel platforms were developed to aid in the characterization of this processes, and the functional gold core following ligand removal was assayed using catalysis.

Several synthetic methods using coprecipitation or deposition-precipitation exist for the creation of supported gold assemblies without ligands, one significant limitation is the inability to finely tune the final gold particle size independently of the support material.[3] Alternatively, approaches for the creation of supported gold clusters using pre-synthesized AuNPs allow for precise control over the size and morphology of the gold core; however, in these cases the ligand shell must then be removed.[15] A survey of the literature reveals three approaches, often used in concert, for the subsequent removal of the ligand shell: thermal,[16] oxidative,[17,18] or solution-based (Figure 1).[15,17] Early approaches focused on heating the supported nanoparticles in order to vaporize the stabilizing ligands. These methods were effective for the removal of ligands, but induced varying degrees of particle growth during treatment.[19-23, 43] This growth obviates the advantage in size control when compared with other methods of generating supported gold clusters.

Solution-based approaches using thermal or oxidative treatments have also been investigated for the removal of ligands. These approaches make use of weakly passivation ligands, polyvinyl acetate (PVA) or triphenyl phosphine, to facilitate ligand shell removal;

however, a thermal treatment was still required.[15,17] For weakly passivating ligands (PVA) thermal treatment in water disrupts the ligand shell while limiting core growth, yet only removes ~20% of the ligands from the particles.[15] The approach is not well suited for particles with more strongly bound ligands, such as thiols. A solution-based treatment using an oxidant (t-butyl hydroperoxide) was shown to effectively remove triphenyl phosphine from gold clusters. However, these clusters underwent morphological changes and particle growth was significant.[17] Other oxidative approaches followed from the demonstration that UV/ozone treatment was effective for the removal of self assembled monolayers (SAMs) from planar gold substrates.[24,25] In these cases, UV irradiation leads to the production of O_3 which in turn oxidizes the organic ligands.[26,27] Studies of nanoparticles on oxide supports showed that once the ligand shell was oxidized, a subsequent thermal treatment was required to remove the ligand, resulting in slightly less core growth than thermal treatments alone.[18]
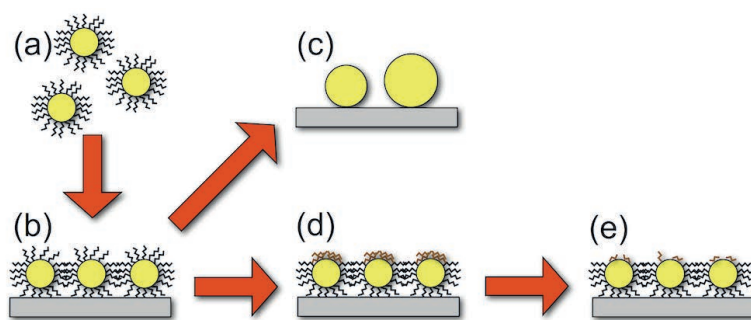
Figure 1. Illustration of two general models for the removal of ligands from supported nanoparticles. First, particles of the desired size are synthesized and purified (a) prior to assembly on a support (b). Ligands are typically then removed using harsh thermal and oxidative treatments leading to varying degrees of particle growth and/or loss (c). Alternatively, we demonstrate using a mild chemical treatment to reduce the affinity of ligand for the particle core (d) affording the room temperature removal of ligand using only water (e).

Supported gold was chosen for a model system because precise control over gold nanoparticle (AuNP) synthesis provides the ability to design well-defined, water-soluble, functionalized building blocks for self-assembly. The careful selection of functionalized nanoparticles maximizes attraction to the oxide support allowing for the creation of both planar analysis platform and a high surface area assembly.[12] Because the ligands are strongly bound it is possible to remove extraneous species following synthesis, which can complicate subsequent assembly steps.[3,13] In addition, terminal functionality can be tailored for specific applications through a ligand exchange reaction following nanoparticle synthesis.[14]

Herein, we report a general strategy for the removal of stabilizing ligands from nanoparticles assembled on a metal-oxide surface. Using the dual analysis approach we demonstrated the utility of gold monolayers as building blocks for self-assembly by tailoring the terminal functionality of the particles and the surface chemistry of the support. A mild chemical oxidation was then used to lower the affinity of the ligand for the surface of the nanoparticle facilitating removal at room temperature by water. In addition, the treatment decreases ligand coverage while maintaining core diameter providing access to an active metal core while retaining tethering to the surface. Given the success of this approach in removing these tightly bound ligands from metal nanoparticles we anticipate that the mild oxidative treatment outlined here may be applied to a wide variety of nanoassemblies.

Results and Discussion

The objective of this study was the removal of ligand from a gold nanoparticle surface with inducing growth in core diameter due to instability. Due to the inherent difficulties in characterizing assemblies of gold nanoparticles on a support material we sought to develop parallel systems in order to afford the use of complementary characterization methods. These platforms allowed for the removal of the ligand shell to be monitored by XPS, the stability of the core to be investigated by TEM, and the accessibility of the gold surface to be assayed by catalysis. Finally the versatility of this method was demonstrated by controlling the degree of ligand removal in order to assess the limits of nanoparticle stability.

AuNPs (d_{core} = 1.4 ± 0.4 nm) were functionalized with (2-mercaptoethyl)phosphonic acid (2-MEPA) and extensively purified prior to assembly. Next, those nanoparticles were assembled on high surface-area fumed silica and the planar SiO_2 windows of a silicon TEM grid.[29] These two types of surfaces were used to examine changes in the functional and structural characteristics of the assemblies upon mild chemical treatment to weaken ligand binding and gently remove those ligands from the surface. The stability of the AuNPs during ligand removal was then investigated by TEM and ICP-OES confirming that the gold core did not grow nor were nanoparticles removed from the surface. Following the mild oxidative treatment for ligand removal, catalysis was used as a method of assaying the available of the gold surface. Finally, the process of ligand removal following assembly was further investigated by characterizing the step-wise removal of ligands from the supported gold, maximizing gold core exposure without compromising the ligand tether to the SiO_2 surface.

We reasoned that the use of a mild chemical treatment to decrease the affinity of the ligand for the particle surface would facilitate the removal of ligand without changing the core size while keeping the attachment to the surface intact (Figure 1). To fully characterize ligand removal chemical transformation of the ligand shell, core size changes, any loss of material, and finally the existence of an active gold surface must all be tracked. SiO_2 was chosen as an inert support material which would not complicate analysis by catalysis.[28] High surface area supports may be used to facilitate experimental techniques that require enough material to demonstrate functional activity or to determine nanoparticle loading by inductively coupled plasma optical emission spectroscopy (ICP-OES). However, surface sensitive analytical techniques, such as X-ray photoelectron spectroscopy (XPS) or transmission electron microscopy (TEM), require an analysis platform with low surface roughness to fully characterize subtle changes to particle chemistry and morphology. XPS is an excellent complementary technique as it can determine the relative amounts of an element, such as sulfur, in various oxidation states. This allows for the characterization of the binding environment for the sulfur head groups of the ligand shell. Complete characterization of ligand removal therefore required the development of both a planar analysis platform as well as assembly of nanoparticles on a high surface area substrate with identical surface chemistry.

Assembly of 1.4 nm 2-MEPA AuNP "Building Blocks"

AuNPs (d_{core} = 1.4 ± 0.4 nm) were functionalized with (2-mercaptoethyl)phosphonic acid (2-MEPA) using a previously described method and utilized for all experiments in this study.[14] Nanoparticles were then extensively purified by diafiltration to ensure that free ligand and extraneous ions from the gold salt were

76

completely removed. Purification is important as the presence of free ligand would impede self assembly[13] and the presence of halides during ligand removal has previously been shown to encourage growth of the gold clusters during ligand removal.[30,31] Previous work by Hutchison and co-workers demonstrated the assembly of 1.4 nm 2-MEPA AuNPs on a Hf(IV) treated silica.[12,32] By synthesizing the AuNPs independently of the support the same batches of precisely defined particles could be deposited on both planar and high surface area SiO_2 surfaces.

Assembly of 1.4 nm 2-MEPA AuNPs on Both Planar and High Surface Area SiO₂ Supports

We developed both a planar analysis platform and a high surface area support to act as dual characterization platforms (Figure 2). A high surface area to volume (200 m^2/g) support was readily available in the form of pyrogenic silica (cab-o-sil) to facilitate high gold wt. % loadings. To create a planar substrate with the same surface chemistry as pyrogenic silica a process similar to that described for the preparation of SMART TEM grids was used.[29] Photolithography was used to create a silicon octagon, 3 mm in diameter, with one half covered in a grid of thermally grown SiO_2 electron transparent windows with minimal surface roughness (Figure 2). The surface chemistry of fumed silica is known to contain a high density of hydroxyl groups; however, previous reports indicate silanol density at the surface of thermally grown silica may be an order of magnitude lower than that of the fumed silica.[33] Thus, the planar substrates were treated with O_2 plasma prior to AuNP assembly in order to increase the silanol density at the surface.
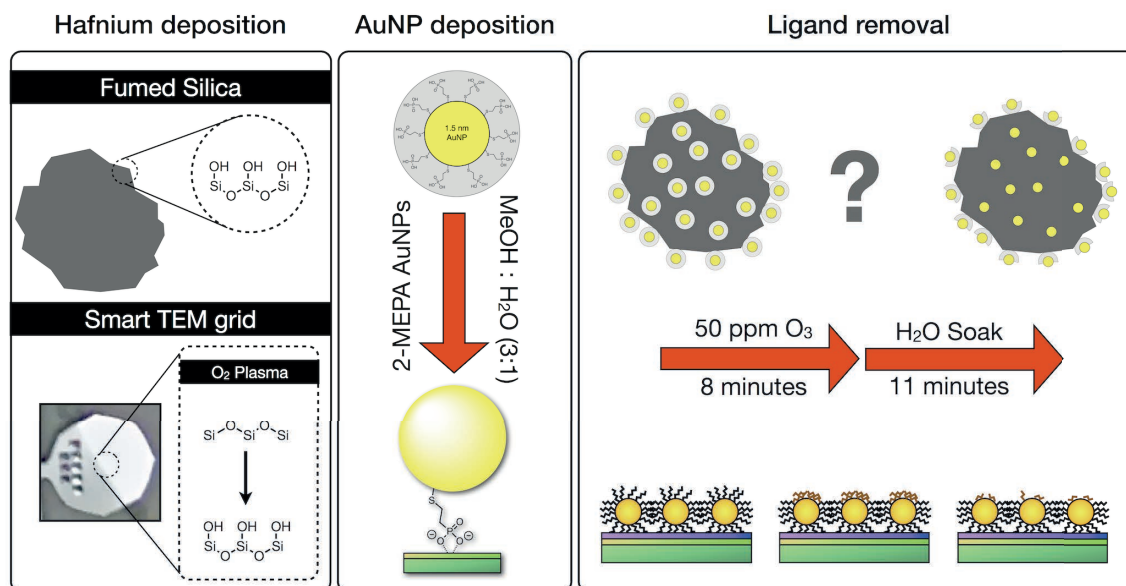
Figure 2. Illustration showing the assembly strategy of 2-MEPA functionalized AuNPs on both a high surface area (fumed silica) and planar (silicon wafer) support. The process is the same other than the required treatment of the TEM grid with O_2 plasma prior to Hf^{4+} treatment.

The silanol rich SiO_2 surfaces of the planar and high surface area substrates facilitated the deposition of Hf(IV), which serve as anchor points for the terminal phosphonate groups of the 1.4 nm 2-MEPA AuNPs.[32,34] Both substrates were soaked in 5 mM $HfOCl_2$ then rinsed with nanopure water. To deposit the nanoparticles both substrates were soaked in a 3/1 methanol:water solution containing 1.6 mg AuNPs per mL of solution. The gold deposition was confirmed on the fumed silica by comparing TEM micrographs before and after nanoparticle assembly (Figure 3). The micrographs of fumed silica did not allow for a statistically significant quantification of nanoparticle size. However, TEM micrographs of the AuNPs on the planar platform showed that coverage was similar and further analysis determined the diameter of the AuNPs following deposition to still be 1.4 ± 0.4 nm (Figure 4).[35] ICP-OES was performed on 6 mg of the

assembled high surface area support following digestion in aqua regia. Results from this experiment indicated a final gold loading of 2.1 wt %. These data all indicate that the directed assembly strategy for 1.4 nm 2-MEPA AuNPs is effective for multiple SiO_2 surface morphologies, both planar and high surface area, by utilizing the terminal chemistry of particle and surface-chemistry of the support material.
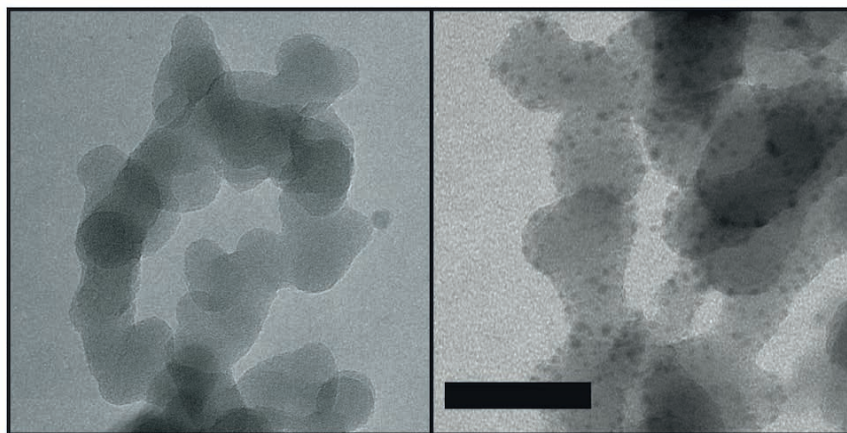
Figure 3. TEM micrographs of fumed silica (CAB-O-SIL) before (left) and after (right) 1.4 nm 2-MEPA AuNP assembly on the high surface area support, scale bar shown 50 nm. Assembly was accomplished by soaking in a 5mM $HfOCl_2$ solution to utilize the terminal phosphonate on the stabilizing thiol ligand (2-MEPA).

Removal of Ligands from Supported AuNPs Using a Dilute Ozone Treatment

Following self-assembly of AuNPs, for applications requiring an active gold surface, ligands must be removed while maintaining core size without the loss of material from the surface. We examined how oxidation of thiol ligands by O_3 could be used to remove the ligand shell while maintaining core attachment to substrate. 1.4 nm 2-MEPA AuNPs were treated with O_3 generated *ex situ* by a corona generator supplied with dry air allowing us to dilute the strength of the oxidant in order to precisely control ligand exposure. The ozone enriched gas stream was diluted 25-fold by nitrogen gas providing a

79

final O_3 concentration of 50 ppm. Both the planar and high surface-area assemblies were treated with the dilute ozone as described in methods. Despite the advantages offered by the use of pyrogenic silica as a high surface area support, the use of a high surface-area substrate presents several challenges related to morphology. Therefore, treatment times for each step of the ligand removal had to be varied to account for the higher surface area and increased steric hindrance.
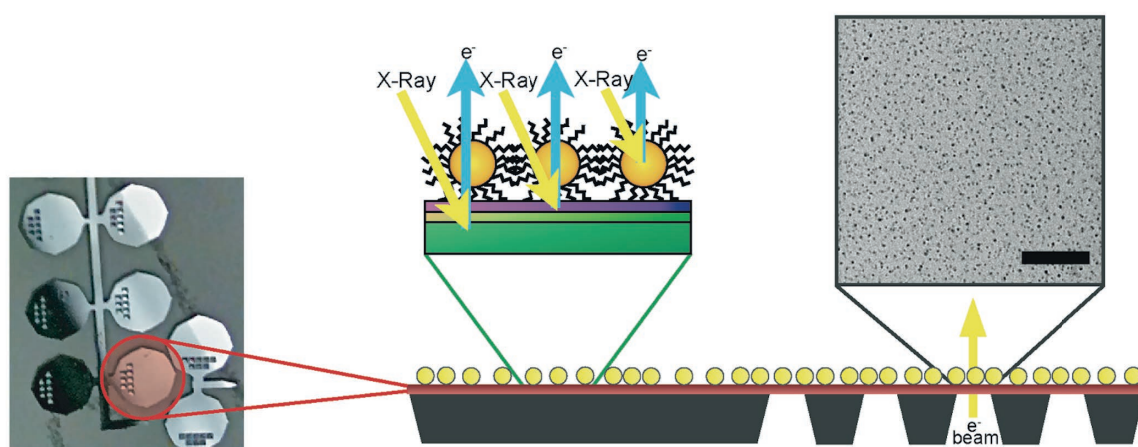
Figure 4. Schematic of the analysis strategy used to evaluate ozone mediated oxidative ligand removal on the planar assembly. 1.5 nm AuNPs were attached to custom SiO_2 TEM grids with only half of the surface containing windows (left) and gold loading was confirmed by TEM (right). The portion of the substrate without windows has a lower surface roughness increasing XPS signal (center). The portion with windows facilitated the direct observation of physical changes to the nanoparticle array using TEM. The combination of the substrates allowed us to visualize subtle morphological and chemical changes and tune the oxidative ligand removal to expose half of the gold surface whilst maintaining total particle size and tethering.

XPS analysis of treated 1.4 nm 2-MEPA AuNPs on the planar analysis platform showed changes in the amount and oxidation state of sulfur from the ligand shell over the course of treatment. The S2p peaks were initially difficult to quantify using curve fitting algorithms due to interference from the underlying silicon plasmon loss feature. To

address this we performed background subtraction from a sample without gold

nanoparticles resulting in flatter baselines. Following baseline correction the peak area,

representing relative amounts of bound reduced-sulfur (B.E. = 162 eV) and oxidized

sulfur (B.E. = 168 eV) were determined.[36-38] Changes to the type of sulfur species present

before treatment, after 10 minutes of exposure to 50 ppm ozone, and finally after the

subsequent water rinse were shown (Figure 5).
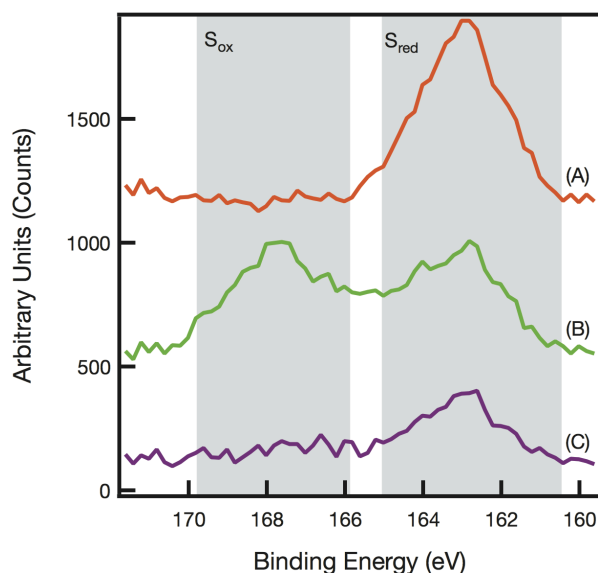
Figure 5. Stacked plot of high resolution XPS spectra over the S2p binding energy range. Red trace (A) represents nanoparticles as assembled on the planar substrate. Green trace (B) represents nanoparticles after eight minutes of dilute ozone treatment. Blue trace (C) represents oxidized sample following an 11 minute nanopure water rinse. Contributions from sulfur bound to gold appear near 162 eV (S_{red}) while oxidized sulfur species have a binding energy near 168 eV (S_{ox}). Each trace had the silicon loss feature removed via background subtraction using a the S2p trace from Hf(IV) treated substrate.

These data are consistent with a portion of the ligand shell being oxidized, as

evidenced by the presence of both bound thiolate and oxidized sulfur species following

exposure to dilute ozone. Previous literature indicated that the oxidized sulfur may be

strongly associated with the gold surface[18]; however, these data suggest the majority of oxidized sulfur products are easily removed at room temperature by water following treatment. The residual bound thiolate suggests that some of the ligand shell may remain intact tethering the AuNPs to the support.

Quantifying Nanoparticle Stability Over the Course of Ligand Removal

Following ozone treatment and removal of oxidized ligand by soaking in water, TEM analysis of the planar substrate suggested no significant nanoparticle loss (Figure S1). To quantify the amount of gold that may have been lost the pyrogenic silica was used for analysis by ICP-OES. Given the much higher surface area and increased hindrance to accessing the surface compared to the planar system, the ozone treatment time was increased to 20 minutes. Following ozone treatment the high surface area support assembly was soaked in nanopure water for 11 minutes and the supernatant was collected and analyzed by ICP-OES. The supernatant recovered indicated a negligible amount of gold loss (< 0.2 wt %). These data are consistent with the thiolate ligand that remains after ozone treatment strongly tethering the AuNPs to the surface even preventing particle loss.

Applications leveraging the size-dependent properties of supported AuNPs would be comprised by particle growth during treatment. To confirm the stability of the AuNPs during ligand removal we exposed planar assemblies to the dilute ozone stream for up to 16 minutes. These samples were then soaked for 11 minutes in 20 mL of nanopure water, dried under a stream of argon, and finally analyzed by TEM (Table 1). The uniform surface of our planar system allowed us to capture micrographs from a large area in order to examine a large population of particles. For treatment times through 8 minutes 1.4 nm

2-MEPA AuNP size remained constant even after the removal of oxidized ligand. Only after the planar system was exposed to dilute ozone for twice that time did the particles exhibit slight growth following the water soak (from 1.4 ± 0.4 to 1.6 ± 0.6 nm). Treatments times of 8 minutes or below were successful for ligand removal without associated core growth that would jeopardize the size-dependent properties of the supported AuNPs.

Table 1. 2-MEPA AuNP core diameter following ligand removal

Ozone treatment	Size following treatment and rinse[a]
No Treatment	1.4 ± 0.4 nm
4 Minutes	1.4 ± 0.3 nm
8 Minutes	1.4 ± 0.4 nm
12 Minutes	1.6 ± 0.6 nm

[a] Gold nanoparticle diameter and polydispersity were determined by TEM analysis of the planar assembly during ozone treatment between 4 and 16 minutes, followed by an 11 minute soak in nanopure (18.2 M) water to remove oxidized ligand. The particles size did not change during treatment. Limited growth was observed only after extended ozone exposure.

Corroborating the Successful Removal of Ligands from AuNPs

To confirm that an active gold surface is available, catalysis was used as a functional assay to corroborate the XPS analysis indicating successful ligand removal from the 1.4 nm 2-MEPA AuNPs following ozone treatment. Given the limited amount of material supported on the planar analysis platform, the high surface area substrate was used for this demonstration. The room temperature oxidation of $CO_{(g)}$ was chosen, as the reaction is sensitive to both the preparation method of the supported AuNPs as well as the

final gold cluster size.[30] In addition, any catalytic activity observed is unlike to be influenced the SiO_2, which is generally thought to be non-participating.[3] Control experiments, using both bare pyrogenic silica and AuNP assemblies on the high surface area support before ozone treatment, were performed by adding 0.1 g to an IR gas cell flushed with $N_{2(g)}$ before the addition of equal molar concentrations of $O_{2(g)}$ and $CO_{(g)}$. Neither of these untreated samples demonstrated catalytic activity. Finally, the high surface area assembly was treated with dilute ozone and rinsed as described previously. Following lyophilization 0.1 g was added to the IR gas cell, flushed as before, and conversion of the $CO_{(g)}$ to $CO_{2(g)}$ was monitored until the reaction had gone to completion (Figure 6).
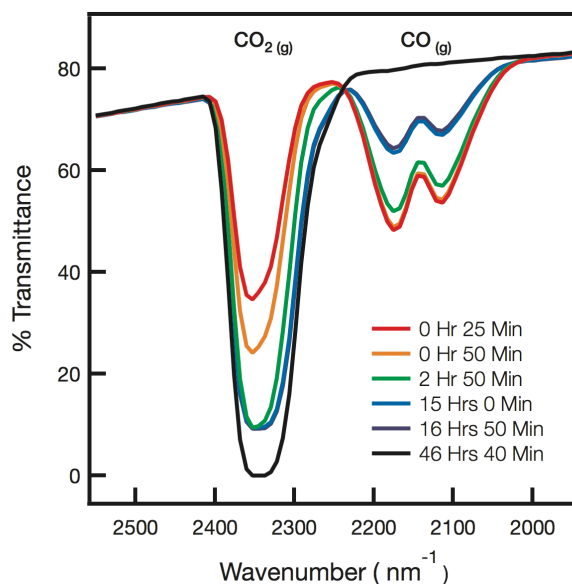
Figure 6. FT-IR spectra from gas cell containing activated AuNP decorated fumed silica to which 3mL each $O_{2(g)}$ and $CO_{(g)}$ were added. The catalytic oxidation of $CO_{(g)}$ was monitored by the decreasing peaks at 2150 cm^{-1} to complete conversion to $CO_{2(g)}$ indicated by the increasing peak at 2450 cm^{-1}. Spectra were y-shifted to normalize the baseline at 2600 nm^{-1} to correct for flow cell movement

Given the poisoning effect of thiols for gold catalysis, the catalytic activity

observed confirms the availability of an active gold surface following the ozone treatment.

These data provide a picture of the of the physical and chemical changes that occur over

the course of ligand removal from supported AuNPs. A portion of the ligand shell is

oxidized during treatment and we hypothesize that the ligands remaining may continue

to tether the particles to the surface and the oxidized sulfur may be rinsed away with

water in order to afford access to the active gold surface.

The restoration of 2-MEPA ligand on the particles would corroborate the removal

of ligands from the surface and suggests the utility of this treatment for the placement of

ligands on the bare gold surface. To show the ease and rapid rate of ligand replacement

on the surface, a sample of our planar analysis platform, containing particles that were

ozone treated and rinsed, were placed in a 1mM 2-MEPA ligand solution for 1 and 10

minutes and characterized using high resolution XPS scans of the S2p region (Figure S3).

The results indicated an increase in reduced sulfur and loss of the small amount of

oxidized sulfur remaining on the surface after ozone treatment, highlighting the success of

the ligand replacement. As a corollary this replacement happened within 1 minute of

placing the sample in the ligand solution and we observed no change in the S2p region

after 10 minutes of soaking. In contrast, place exchange reactions of thiol typically reach

equilibrium on the order of hours to days.[39] This method may therefor afford a facile

method for installation of other ligand functionalities without lengthy treatment times.

Characterizing the Step-Wise Removal of Ligands from Supported 1.4 nm 2-MEPA AuNPs

To further characterize the details of the ligand removal process over time we

used the TEM and XPS analysis capability of the planar characterization platform to

tune the degree of ligand removal. The duration of ozone exposure as well as the

subsequent rinse time was optimized to expose as much of the active gold surface as

possible while maintaining a covalent tether to bind the AuNPs to the support without

causing a change in the average particle size. Multiple samples, decorated with 1.4 nm 2-

MEPA AuNPs, were introduced into the dilute ozone gas stream. The samples were

removed two at a time over the course of treatment, and one sample was then analyzed

by XPS and TEM while the other was first rinsed with nanopure water before analysis

(Figure S2). The ratio (as a percentage of total sulfur) of oxidized sulfur (B.E. 168 eV) to

bound thiolate ligand (B.E. 162 eV) was determined (Figure 7).
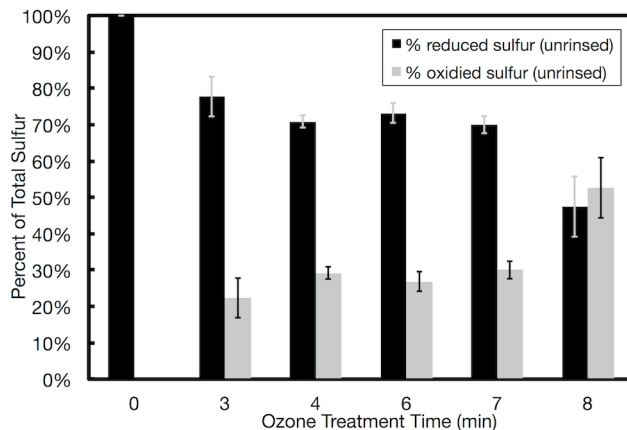
Figure 7. Graphical interpretation of the S2p peak area ratios between reduced sulfur
(thiolate) and oxidized sulfur (sulfate) species resulting from zero to eight minutes
exposure in dilute ozone followed by nanopure water rinse. Each treatment time was
sampled over three spots to account for surface variation and error bars represent one
standard deviation from the mean. Peaks were fit to S2p trace and each percentage
calculated from the sum of oxidized (168 eV) and reduced (162 eV) calculated area.

A dilute ozone treatment time of 8 minutes was chosen as an ideal treatment point

from the observed crossover between oxidized and reduced sulfur at this point contrasted

to the roughly 20% oxidized it had attained after only about 3 minutes of ozone

treatment and a relatively steady 30% oxidized over the next 5 minutes. The removal of

the oxidized ligands by rinsing with water was then tuned by exposing several samples to

dilute ozone for 8 minutes. These samples were then placed in 20 mL of nanopure water

and allowed to soak for between 1 to 20 minutes. The samples were removed one by one,

dried under a dilute stream of argon, and then analyzed by XPS. Analysis of these

samples showed that the amount of oxidized sulfur remaining leveled off after 11 minutes

in water, so this was taken as the optimal rinse time (Figure 8).
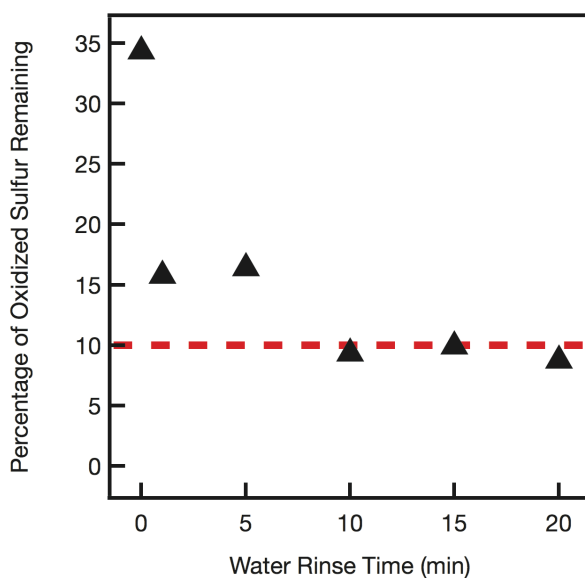
Figure 8. Percentage of oxidized ligand remaining on the gold nanoparticle surface versus the rinsing time, in minutes. After 10 minutes the number of ligands remained stable at 10% as designated by the dashed line. The percentage of ligands was calculated from XPS ratios of oxidized to reduced sulfur 2p peaks.

We were able to use the relative amounts of reduced and oxidized thiol

throughout the treatment to determine the number of ligands involved in each process

(Figure 9). 1.5 nm 2-MEPA functionalized AuNPs have previously been well

characterized by the Hutchison lab showing that on average each has 35 ligands bound to

the surface of the gold core.[14] Given confirmation that the average particle size does not change over the course of treatment (Table 1) we calculated the number and type of ligands involved in each treatment step. Initially, all 35 ligands are in the form of bound thiolate. Following 8 minutes of exposure to the 50 ppm ozone gas stream the *average* particle contains 52.6% oxidized sulfur and 47.4% bound thiolate indicating that 17 ligands remain unchanged while 18 of the ligands have been oxidized. Although oxidation to sulfonate cannot be ruled out by XPS data alone, cleavage of the C-S bond resulting in sulfate and a remaining oxidized ligand fragment would be consistent with previous literature reports characterizing the removal of thiolate SAMS from planar gold.[27,40] Additionally, reports using sum frequency spectroscopy on much larger AuNPs (>15 nm) the initial stages of AuNP oxidation were shown to result in the asymmetric ligand removal. Taken together with our data this suggests the preferential oxidation of ligand from the top half of gold nanoparticles.[41] After 11 minutes of water soaking, the average particle was shown to consist of 33.1% oxidized sulfur and 66.9% bound thiolate. We assumed that the 66.9% thiolate signal comes from the same 17 bound thiolate ligands, that is no thiolate is rinsed away. It follows that there were still approximately 8 oxidized sulfur atoms remaining following treatment. We can therefore reason that the mild ozone treatment followed by a room temperature water soak, was able to remove 10 of the 35 thiols initially found in the ligand shell of a 1.5 nm 2-MEPA functionalized AuNP, revealing an active gold surface.
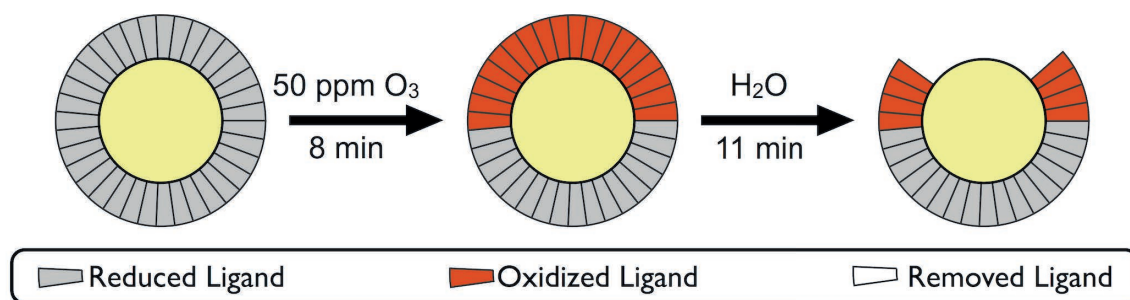
Figure 9. Schematic depicting the changes in the ligand shell following 8 minutes of exposure to 50 ppm ozone and the subsequent 11 minute rinse in nanopure water. Each section represents one 2-MEPA ligand based on an average 1.5 nm gold nanoparticle. These values were calculated using the XPS peak area ratios for oxidized and reduced sulfur.

Conclusion

We demonstrated the successful removal of thiolate ligand from AuNPs tethered on various oxide supports. While ligand protected nanoparticles offer considerable synthetic benefits, including size-control and the introduction of a wide-variety of terminal functionality, their use also introduces the challenge of ligand removal following assembly. Utilizing well-defined nanomaterials as building blocks, we demonstrated a general strategy for the removal of the ligand shell at room temperature following self-assembly of functionalized nanoparticles. By using dilute ozone, as a gentle chemical treatment to lower the affinity of the ligands for the nanoparticle surface, ligands can be removed at room temperature without causing core growth or loss of material from the support. This approach was illustrated using gold nanoparticles as assembly with water-soluble functionalized nanoparticles offers several advantages over other methods previously demonstrated for creating supported gold clusters. In addition, the choice of terminal functionality for the AuNPs enabled the tailoring of assembly behavior to the support material used. The removal of ligands from 2-MEPA protected AuNPs was

confirmed by using catalytic activity to demonstrate the availability of the gold core. The high activity of these supported AuNPs is indicative of the efficacy of the ligand removal.

This study also showed the advantages of considering and addressing characterization challenges during experimental design. To this end, 1.4 nm 2-MEPA AuNPs were assembled on parallel, planar and high surface area, SiO_2 substrates. This study utilized the benefits of using a multi-platform approach to apply complementary characterization techniques, which provided new insight into the chemical transformations of the ligand shell during oxidative ligand removal. We quantified the removal of ligand over time in order to expose an active gold surface. XPS analysis confirmed that some thiol remained on the AuNPs to act as a tether to the SiO_2 surface even after oxidation and rinse. In addition TEM size analysis showed no particle growth and ICP-OES confirmed that AuNPs were not lost during treatment. Given the ability of this mild oxidative treatment to remove strongly binding thiolate ligands, this method is likely to be a successful general strategy for ligand removal following nanoparticle assembly with any ligand susceptible to oxidation.

Methods

Gold Nanoparticle Synthesis

The nanomaterials used for experiments were all 1.4 nm gold nanoparticles (AuNPs). Synthesis of triphenyl phosphine stabilized particles was accomplished through a sodium borohydride reduction of $HAuCl_4$, triphenylphosphine, and TOAB in water and toluene following literature preparation.[14] Biphasic ligand exchange was performed with (2-mercaptoethyl)phosphonic acid (2-MEPA) ligand synthesized from a literature preparation.[12] Exchanged particles were washed using a diafiltration membrane[13] with

100 volume equivalents of nanopure water. Following washing 1.4nm 2-MEPA AuNPs were concentrated, lyophilized, and stored in the freezer until use.[12]

Hafnium Decoration of Fumed Silica

Two aliquots of 0.5 g fumed silica were each placed in a 20 mL centrifuge tube. A 15 mL solution containing 5 mM $HfOCl_2$, was added to the silica with a stir bar. This solution was stirred for two days. Hf decorated fumed silica was pelleted by centrifugation and resuspended in nanopure water this process was repeated three times to adequately rinse the sample.

Gold Nanoparticle Assembly on Fumed Silica

In each centrifuge tube of Hf(IV) functionalized silica 15mL of gold soak soution (1.6 mg of 1.4 nm 2-MEPA AuNPs)/(1mL of 3/1 $MeOH/H_2O$) were added and stirred for 2 days. The 2-MEPA AuNP decorated fumed silica was pelleted by centrifugation and resuspended in 15 mL nanopure water this process was repeated three times to rinse the sample. Material was lyophilized and stored in the freezer until use.

Planar Analysis Platform Preparation

To prepare a silica surface for TEM and XPS analysis a silicon wafer was diced into chips and an thermal oxide layer grown by heating to 1100°C in O_2 for 13min. Positive photoresist used to establish window boundaries. Oxide was etched in diluted buffered oxide etch and unwanted silica was etched away soaking in 10% TMAH solution at 60°C for 8 hours to reveal windows.[29]

Tethering 1.4 nm 2-MEPA Gold Nanoparticles to Analysis Platform

Grids were cleaned with oxygen plasma and soaked for 15 minutes in a dilute NH_4OH and H_2O_2 solution to maximize surface silanol concentration. Grids were rinsed in nanopure water prior to soaking overnight in 5mM Hf(IV) to generate anchors. AuNP tethering was afforded with an overnight soak (1.6 mg-1.4 nm 2-MEPA AuNPs)/(1mL-3:1 MeOH:H_2O).[12]

Ex situ Ozone Generation and Dilution

Ozone was produced by pumping dry air into a corona generator. Undiluted ozone concentration was determined to be 500 ppm by an Ozone 10/a Draeger tube and UV-Vis absorbtion at 253.7 nm. By diluting ozone enriched gas stream with $N_{2(g)}$ 25 fold concentration was lowered to approximately approximately 50 ppm ozone measure by 10/a Draeger tube and UV-Vis absorption at 253.7 nm.

Removal of Ligand from 1.5nm Gold Nanoparticles Tethered to Fumed Silica

To activate our material 0.9 g fumed silica was placed in a 50 mL crystallization dish with a stir bar inside a sealed ozone treatment chamber and stirred. Ozone was flowed into the chamber over 20 minutes. Following ozone treatment the chamber was flushed with $N_{2(g)}$. Material was removed from chamber and rinsed using nanopure water into a centrifuge tube and rinsed three times with 15 mL nanopure water.

Assaying the Nanoparticle Surface

To validate the bare gold surface, 0.1g dry activated fumed silica was added to a IR gas cell with CaF_2 windows that had been flushed with N_2(g), the IR sample chamber

was again flushed with $N_{2(g)}$ for 20 minutes and a background spectrum was taken. 3 mL $O_{2(g)}$ and 3 mL $CO_{(g)}$ were injected into the IR cell and the sample spectrum was shown with background subtracted. FT-IR spectra were collected using a Thermo Scientific Nicolet 6700 spectrometer at a resolution of 16 cm^{-1} to improve signal-to-noise for the determination of $CO_{(g)}$ [42]

XPS Chemical Characterization

XPS spectra were taken at 20 eV pass energy with a ThermoFisher ESCALab 250 with a monochromated Al K-alpha, using a 400 µm spot size. The number of scans was determined empirically to obtain optimal signal/noise.

XPS Sulfur 2p Background Subtraction

To quantify the oxidation of sulfur 2p peaks using XPS we adjusted for the presence of the silicon loss feature in our spectral window. Baseline correction was performed by taking spectra from Hf functionalized platform (blank) and subtracting these spectra from samples of interest. Gain correction was required to adjust for differences in peak intensity, but peaks were not shifted on the binding energy scale. Background subtraction was performed in the program *Avantage* for ease of comparison with other peaks (Figure S4). This technique facilitated quantification of a signal masked by the silicon shake up feature present due to our silica platform.

TEM Microscopy and Nanoparticle Size Determination

Bright-field TEM micrographs were taken using FEI Tecnai Spirit TEM operated at 120 kV or FEI Titan TEM operated at 300 kV. Size distributions were generated using

ImageJ to perform a bandpass filter on the samples and manually applying a threshold so that the final images were representative of the original scanned photos when overlaid.[35]

Determination of Gold Loading

Aqua regia was made from concentrated, high purity, 3/1 nitric/hydrochloric acid. Three samples, 6 mg AuNP decorated fumed silica were digested in 0.75 mL aqua regia. Samples were then diluted to 15 mL and analyzed by ICP-OES. 1 mL of the rinse solution following activation was digested in 0.3 mL aqua regia, then diluted to 15mL, and analyzed by ICP-OES. ICP-OES data was taken on a Teledyne Leeman Prodigy running with standard operating parameters in axial mode.

Bridge to Chapter VI

The successful application of monolayer protected gold nanoparticle as reagents for the construction of a complex nanomaterial was demonstrated. The general strategy of utilizing already functionalized nanoparticles in a convergent synthesis, where synthetic challenges may be compartmentalized to either parallel branch, was further vindicated. While Chapter IV made use of the ligand shell to add additional properties to the nanoparticle building blocks, in Chapter V the novel size dependent properties of the metal core were utilized. Chapter VI will summarize the approach to this design strategy and enumerate some of the benefits therein.

CHAPTER VI

CONCLUDING SUMMARY

In this dissertation the concept of functionalized nanoparticles as reagents for use as building blocks in the design of complex nanomaterials was explored. The intent was to provide a framework planning the design, synthesis, modification, and characterization of functional nanomaterials in an efficient way. The roadblocks to the actualization of gold nanoparticles in new applications were identified including nanomaterial definition, characterization challenges and difficulty with reproducibility during synthesis. By considering these issues with a modular approach it was possible to utilize the unique properties of gold nanoparticles without further complicated the synthetic route required. The optimization of the microfluidic reactor described in Chapters III and IV, along with rapid solution phase characterization by SAXS, made it possible to rapidly explore the synthetic parameter space in order to maximize stability and function. This general design strategy was applied to the synthesis and utilization of gold nanoparticles for use as both chemical reagents (Chapter IV) and nanomaterial building blocks (Chapter V). These methods will allow for more rapid iterations through phases of new nanomaterial discovery, definition and characterization, and utilization for functional applications.

Chapter II describes the challenge of defining a nanoscale material. Examples of corroborative and complementary characterization techniques applied to a multitude of different nanomaterials in solution were provided. The importance of careful definition of nanomaterial properties was also highlighted. By considering the challenges of

characterization during nanomaterial design significant savings in both cost and time may be realized.

Chapter III demonstrated a new synthetic method for the direct synthesis of functionalized thiolate protected gold nanoparticles. Critically, the ability to tune the core diameter independently of the desired ligand functionality was made possible when Bunte salts were used as ligand precursors. The development and optimization of a microfluidic reactor also provided improvements in batch-to-batch reproducibility and scale up. Lessons learned during these studies made it possible to design a nanoparticle reagent that took advantage of the properties of the ligand shell as a scaffold for further organic coupling reactions. This synthetic approach is an analog of the convergent syntheses used in organic chemistry. By compartmentalizing the synthetic challenges to either building block many of the challenges faced by nanoscientists may be addressed.

In Chapter IV an azide functionalized, water-soluble, gold nanoparticle chemical reagent was designed and synthesized according the parameters of click chemistry. Rapid synthesis and characterization previously developed afforded ease of investigations into how ligand shell composition affected solubility and reactivity. The reactivity of these nanoparticle reagents was demonstrated by coupling a variety of cyclooctyne terminal alkynes to the ligand shell. Critically, the products of these coupling reactions remained stable in solution and could be readily purified using tangential flow filtration, and were subsequently isolated by lyophilization.

The ligand shell of a nanoparticle provides control of final core diameter during synthesis and allows for the addition of new properties to the particle. However, one major draw to gold nanoparticles specifically is the existence of novel size-dependent properties such as catalytic activity. For these applications an in tact ligand shell is

detrimental to the utilization of the metal core. To address these challenges we developed

a general method of the removal of ligands susceptible to oxidation form the core of

nanoparticles. Using a dilute ozone treatment we were able to characterize the tunable

removal of ligands from the nanoparticle surface, while maintaining the stability of the

tethered nanoparticle more.

The general strategies laid out will allow for new nanomaterials to be designed

and synthesized rapidly. These methods are necessary as researchers continue to address

specific needs by tailoring nanomaterial properties to address them. As libraries of

nanoparticle reagents are developed there are likely to be compounded benefits to the

field.

APPENDIX A

SUPPORTING INFORMATION FOR CHAPTER III:

SIMULTANEOUS CONTROL OF LIGAND FUNCTIONALITY AND CORE SIZE

DURING DIRECT SYNTHESIS OF 2-10 NM WATER-SOLUBLE GOLD

NANOPARTICLES

Materials and Analytical Methods

Hydrogen tetrachloroaurate hydrate ($HAuCl_4 \cdot xH_2O$, 99.9%) was purchased from

Strem and used as received. Water used for syntheses was purified with a Barnstead

NANOpure filtration system (18.2 MΩ resistivity). Bunte Salt ligands were prepared

using known procedures, or slight modifications thereof.[1] Briefly, 1 molar equivalent of

appropriate alkyl halide precursor was dissolved in nanopure water. Sodium thiosulfate

(0.8 molar equivalents) was added and the solution was refluxed for 3 hours. Water was

removed in vacuo, then the crude product was dissolved in ethanol and filtered to remove

salt impurities. All other reagents and solvents were purchased from Sigma-Aldrich or

Macron Chemicals and used as received.

The nanoparticle sizes in solution were determined by SAXS. Details are provided

in our recent publication.[2] Briefly, AuNP samples were analyzed as synthesized and

exposed to monochromated X-rays from a Long Fine Focal spot (LFF) sealed X-ray tube

(Cu 1.54 Å) powered by a generator at 2 kW focused by multilayer optics, measured with

a Roper CCD in a Kratky camera. The Anton Paar SAXSess, in line collimation mode,

was set to average 50 scans of 20 sec for all samples. The corresponding dark current and background scans were subtracted from the data before desmearing was performed using the beam profile in Anton Paar SAXSQuant software. The desmeared data were imported to IGOR Pro (v. 6.22A) software for modeling with 3rd party macros. The size distribution of the sample was determined by using the Modeling II macros in the IRENA package (v. 2.49).[3] The SAXS patterns were fitted using least-squares fitting (LSQF), a size distribution model, a spheroidal form factor (Aspect Ratio = 1), a Gaussian distribution, and a dilute system (Structure Factor = 1). For each sample, reported polydispersity and average core size values were determined through optimization of volume, mean size, and distribution width values to produce the lowest χ^2 value for the model fit to the data.

Transmission electron microscopy (TEM) was performed on an FEI Tecnai Spirit instrument, operating at 120kV accelerating voltage. Amine-functionalized SiO_2 SMART Grids (Dune Sciences) were used for all TEM analysis. TEM grids were prepared by floating the grid on top of a small droplet of the as-synthesized AuNP sample for ~ 30 sec. After removal from the droplet excess liquid was wicked away using a Kimwipe. TEM images were processed using Fiji software as discussed previously.[4] All AuNP samples were analyzed by UV/visible spectroscopy (Ocean Optics) for determination of particle concentration and qualitative determination of particle stability. Ligand precursors and final Bunte Salt products were analyzed by ^{1}H NMR (300 MHz, Varian). For XPS and TGA analysis, excess ligand and salts were removed from solution by diafiltration using a 75 kDa membrane (Pall).[5] XPS spectra were taken at 20 eV pass energy on a ThermoFisher ESCALab 250 with a monochromated Al K-alpha, using a

400 µm spot size. Spectra were corrected to Au 4f at 84.95 eV. Peak fitting was performed

using ThermoFisher Avantage software. TGA measurements were conducted on a TA

Instruments Q500 TGA under nitrogen atmosphere. Samples were run from 25°C to

500°C at a ramp rate of 10°C/min. Gold nanoparticle samples were prepared by placing

~ 0.5 - 2 mg of lyophilized nanoparticles into a tared pan. The sample was then

immediately analyzed.
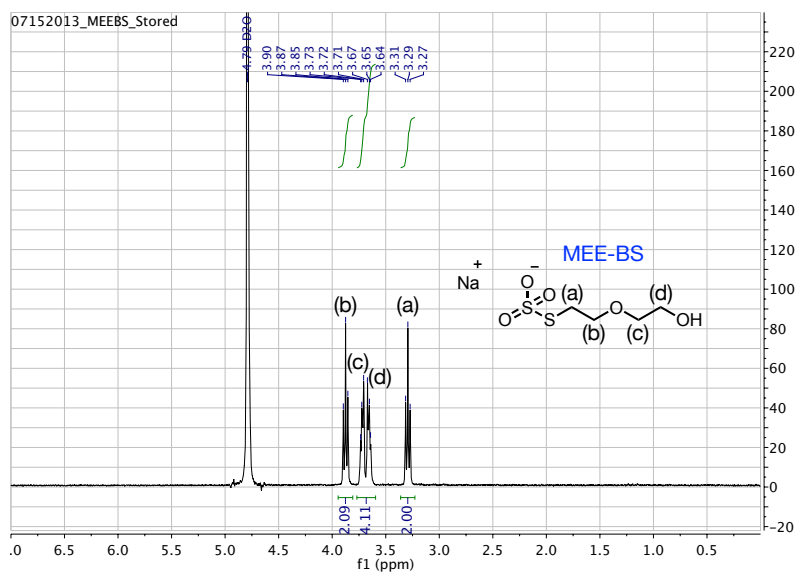
Figure S1. NMR spectrum for MEE Bunte salt ligand.
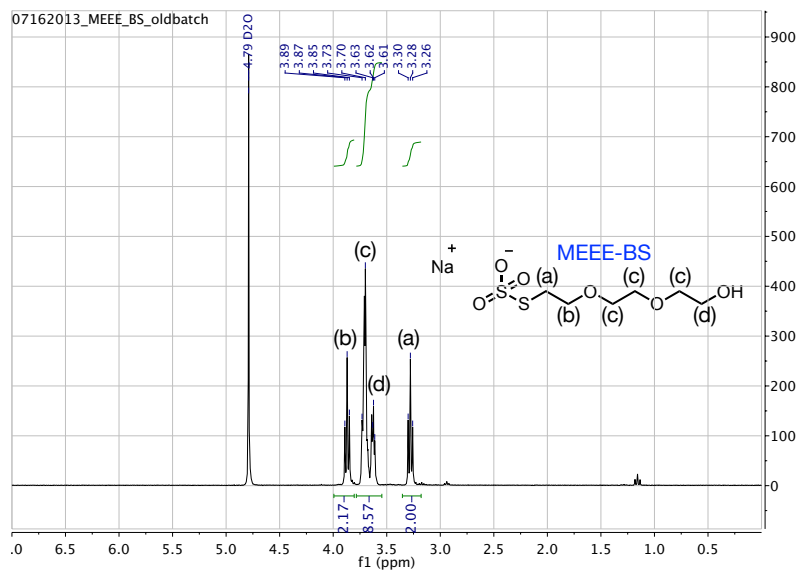
Figure S2. NMR spectrum for MEEE Bunte salt ligand.
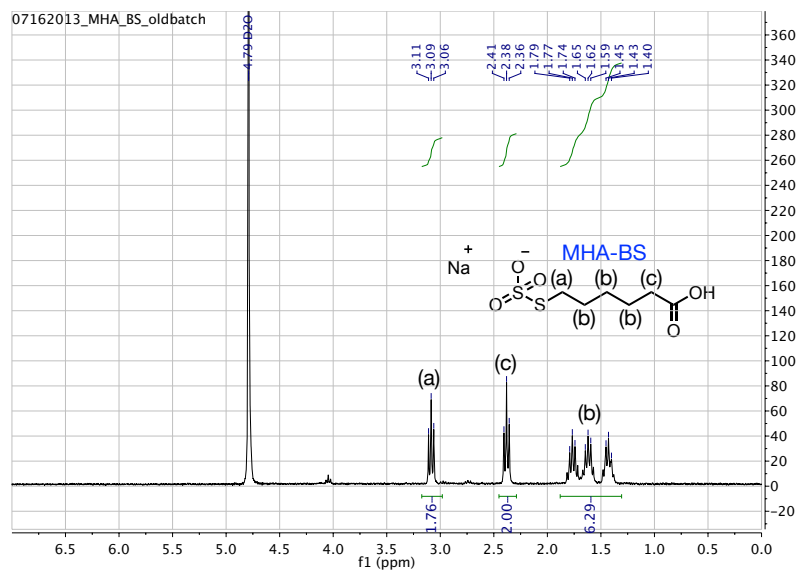
Figure S3. NMR spectrum for MHA Bunte salt ligand.

Experimental Details for Microreactor Synthesis

Three syringe pumps each equipped with 3-way distribution valves were purchased from Kloehn (Versa 6, 48k model with rotary valve). All other microreactor components were purchased from IDEX Health and Science. FEP tubing (1/16" outer diameter, 0.030" inner diameter), T-mixers (1/16", 1/4-28, 0.020" Thru, ETFE), 15 psig check valves, and appropriate fittings (1/4-28) and ferrules were assembled with the syringe pumps as shown to enable microfluidic generation of AuNPs. Tubing and T-mixers were swapped out if material deposition occurred. Solutions were pumped at a total flow rate of 60 mL/min, with tubing lengths selected to allow for sufficient mixing time in the microfluidic system.

Aqueous solutions were prepared to enable three successive microfluidic syntheses at each reaction condition. Thus, 30 mL of 5.0 mM $HAuCl_4$, 30 mL of 1.0 mM Bunte Salt ligand, and 60 mL of 1.0 mM $NaBH_4$ were prepared. A total of 0.825 mL of 1.0 M NaOH was added to these solutions, split between the $HAuCl_4$ and $NaBH_4$ solutions. The desired amount of NaOH (ranging from 0.127 mL – 0.510 mL) was first added to the $HAuCl_4$ solution, determining the initial Au(III) speciation and effectively controlling the final AuNP dimensions. Corresponding Au(III) pH values and added volumes of NaOH are summarized in Table S1. The remaining amount of total NaOH (ranging from 0.698 mL – 0.315 mL) was added to the $NaBH_4$ solution to maintain final pH of the system. It is advantageous to prepare the $HAuCl_4$ solution first, as it can take up to 20 min to reach equilibrium at high pH. Additionally, the $NaBH_4$ solution should be prepared last, as this reagent also undergoes undesirable hydrolysis in water, albeit slowly.[6] Note that 0.012 mL of additional 1.0 M NaOH was added to the 30 mL of 1.0 mM

MHA ligand solution to ensure the acid group was deprotonated at all conditions (a total of 0.837 mL base were added for these syntheses).

Table S1. Summary of NaOH volumes added to precursor solutions to tune Au(III) pH and achieve AuNP size selectivity.

Au(III) pH	Au(III) pH Abbreviation	1M NaOH added to HAuCl4 solution (mL)	1M NaOH added to NaBH4 solution (mL)
2.97	~ 3	0.127	0.698
3.93	~ 4	0.225	0.6
4.9	~ 5	0.325	0.502
5.87	~ 6	0.42	0.405
6.76	~ 7	0.51	0.315

Once the appropriate amount of base was added to the respective solutions, each of the three solutions was aspirated by the three syringe pumps as shown in Figure 1 in the manuscript. The 20 mL of NaBH$_4$ solution was dispensed at 30 mL/min, mixed with a stream of 10 mL of ligand solution flowing at 15 mL/min, mixed along a 1.64 m length of tubing (1 second of residence time), before introducing the third stream of 10 mL of Au(III) solution flowing at 15 mL/min. Two simple T-mixers were used to mix the reagents. 15 psig check valves were utilized at each of the 10 mL syringes to avoid backflow. At a total flow rate of 60 mL/min, the final mixed solution is allowed to flow through the reactor for ~ 2 seconds (~ 5 m of tubing) before being collected. Small fractions at the beginning and end of each reaction were discarded. The microreactor

system was rinsed with nanopure water three times (full aspirate/dispense cycles of the

syringe pumps) after each synthesis. Each synthesis was repeated another two times, using

the remainder of the prepared solutions, to determine reproducibility. After each set of

three syntheses, the downstream T-mixer that introduces the Au(III) solution was replaced

with a clean mixer. The used mixers are later cleaned with aqua regia and water to

remove any plated Au material left behind. If any plated material was evident in the

reactor tubing, it was discarded and replaced with fresh tubing.

Nanoparticle Characterization

Transmission electron microscopy. TEM analysis was performed across the size range for

each working curve shown to determine particle morphology. AuNPs synthesized at all

pH values were observed to be spherical. The following are representative images for
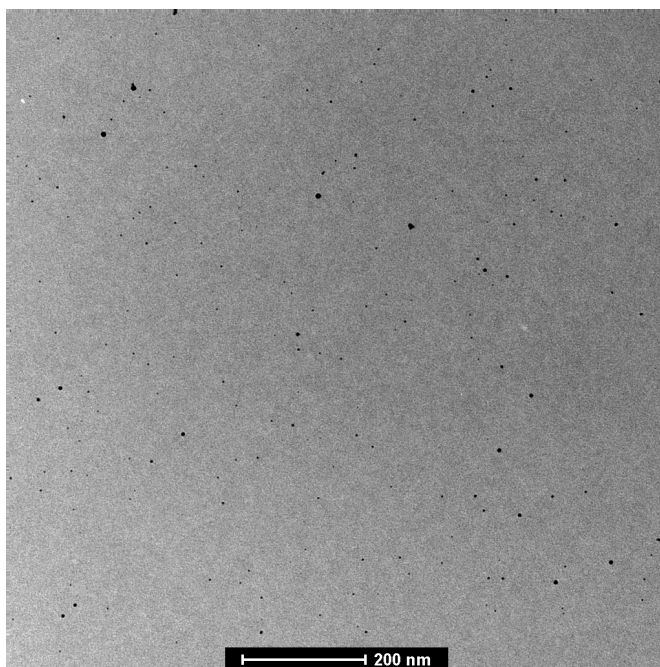
each AuNP working curve.
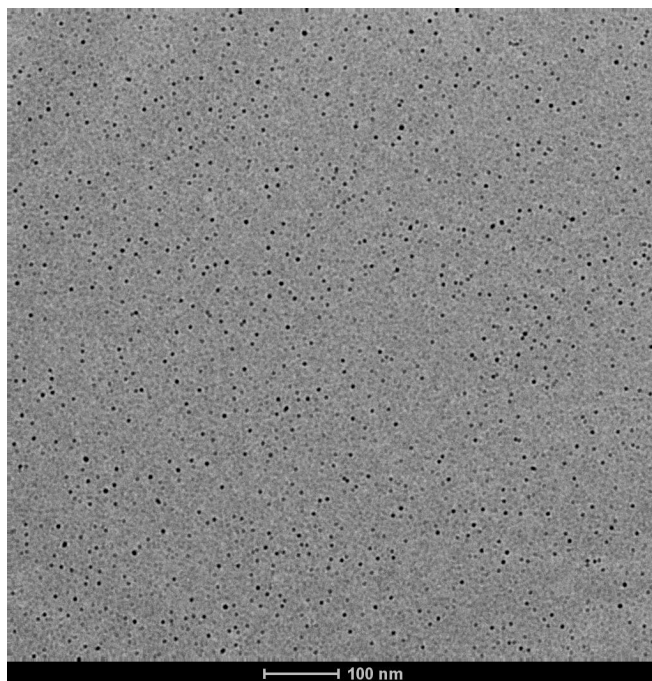
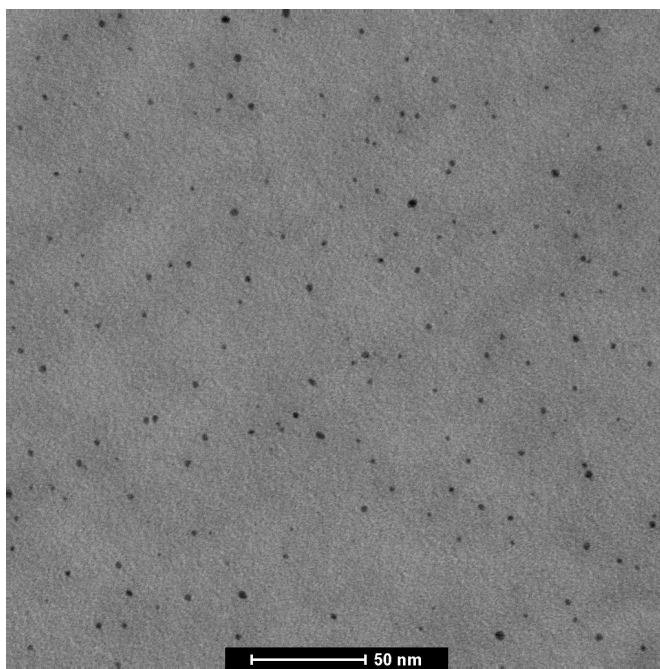**Figure S4.** TEM micrograph of MHA-passivated AuNPs synthesized at Au(III) pH ~ 3.
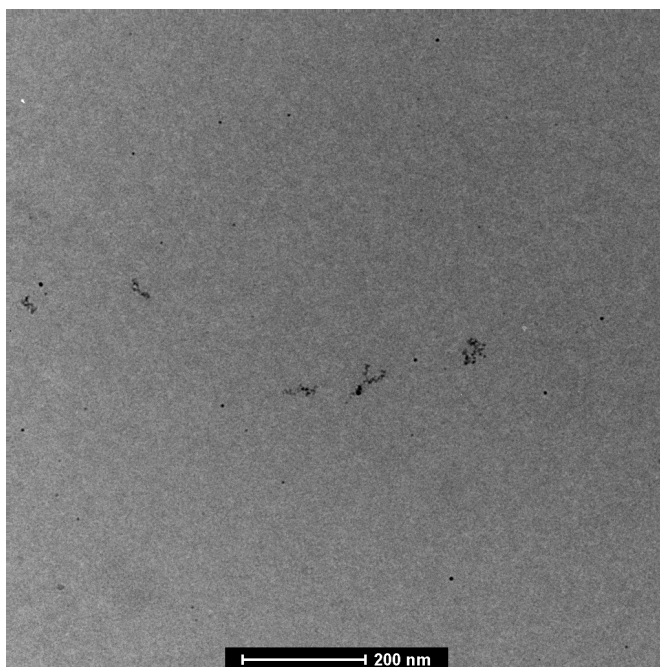
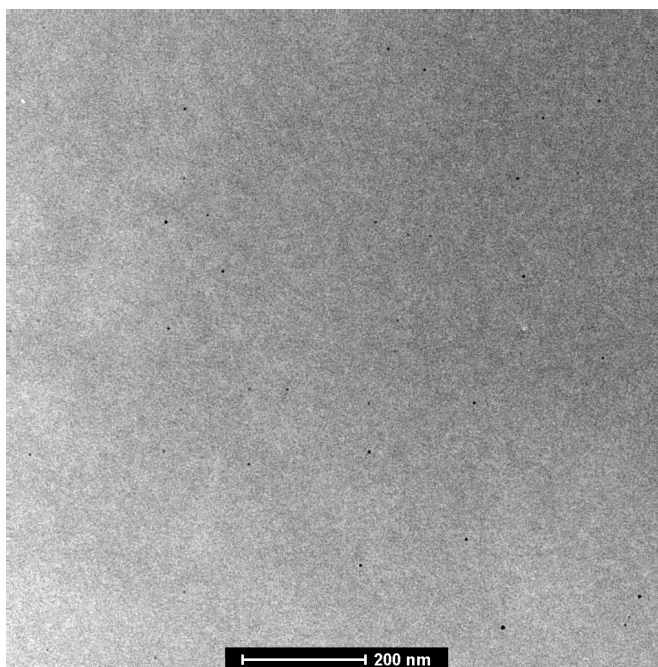**Figure S5.** TEM micrograph of MHA-passivated AuNPs synthesized at Au(III) pH ~ 7.
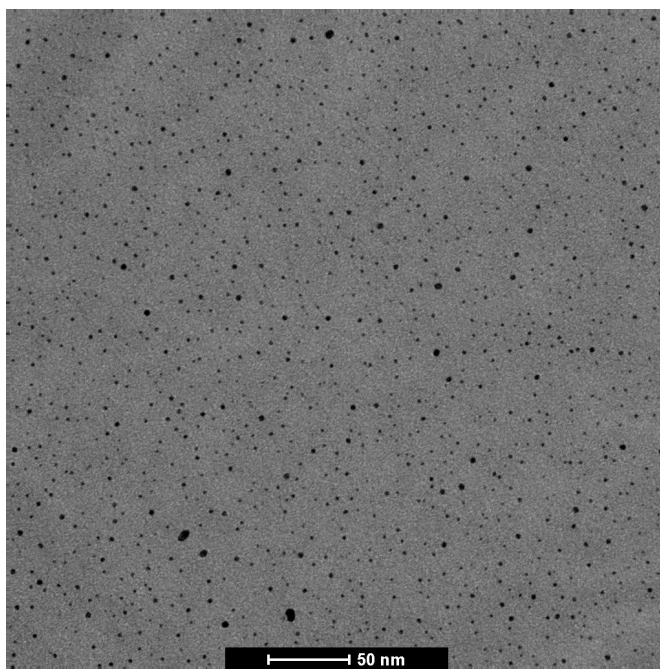
Figure S6. TEM micrograph of MEE-passivated AuNPs synthesized at Au(III) pH ~ 3.

Figure S7. TEM micrograph of MEE-passivated AuNPs synthesized at Au(III) pH ~ 7.

Figure S8. TEM micrograph of MEEE-passivated AuNPs synthesized at Au(III) pH ~ 3.

Figure S9. TEM micrograph of MEEE-passivated AuNPs synthesized at Au(III) pH ~ 7.

Thermogravimetric Analysis of AuNPs. TGA data were collected to determine the relative coverage of ligand on AuNPs at the extremes of the observed pH range. Beginning and end of ligand mass loss was determined by identifying when the derivative of mass loss vs. temperature had a slope of zero before and after the first major mass loss peak. All values match well to expected values.

Table S2. Comparison of calculated expected mass loss and observed mass loss for thiolate-passivated AuNPs.

| Sample	Expected Mass Loss	Observed Mass Loss
MEE-AuNPs pH ~ 3	10.5%	11.4%
MEE-AuNPs pH ~ 7	4.2%	5.1%
MEEE-AuNPs pH ~ 3	11.9%	15.8%
MEEE-AuNPs pH ~ 7	6.1%	6%
MHA-AuNPs pH ~ 3	13.1%	13.1%
MHA-AuNPs pH ~ 7	4.4%	6.1%

[a] - Expected mass loss calculated for complete thiolate monolayer on AuNP surface
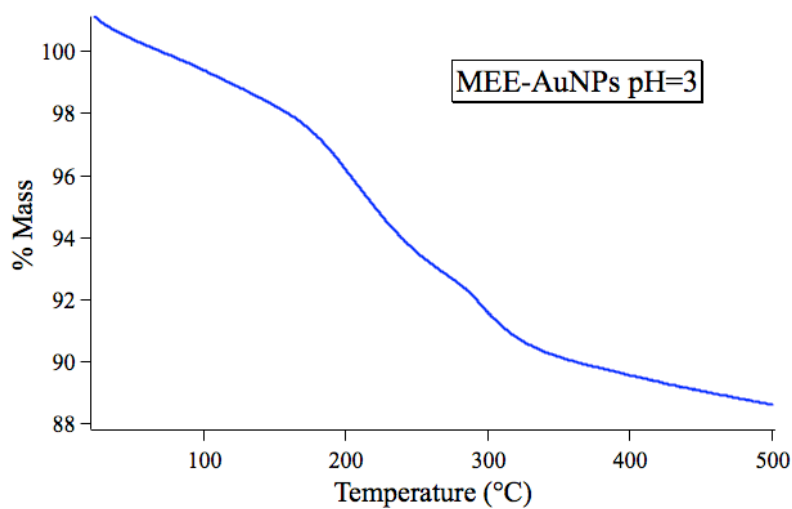
Figure S10. TGA data for AuNPs synthesized at Au(III) solution pH ~ 3 using MEE Bunte salt ligand.
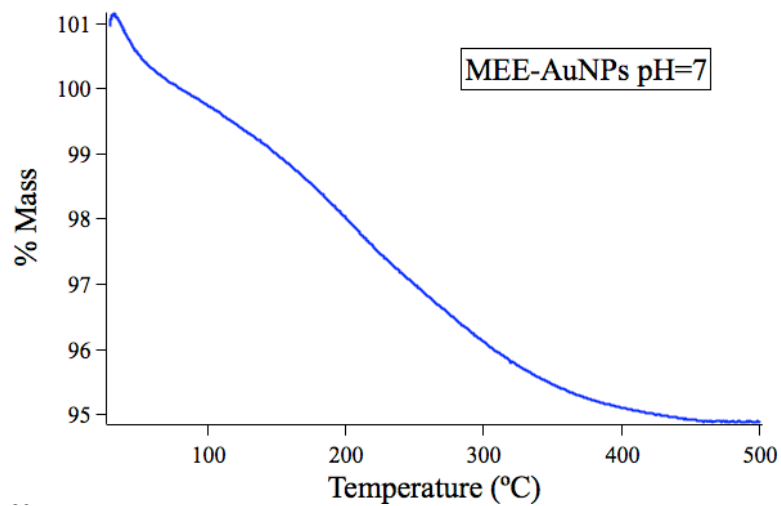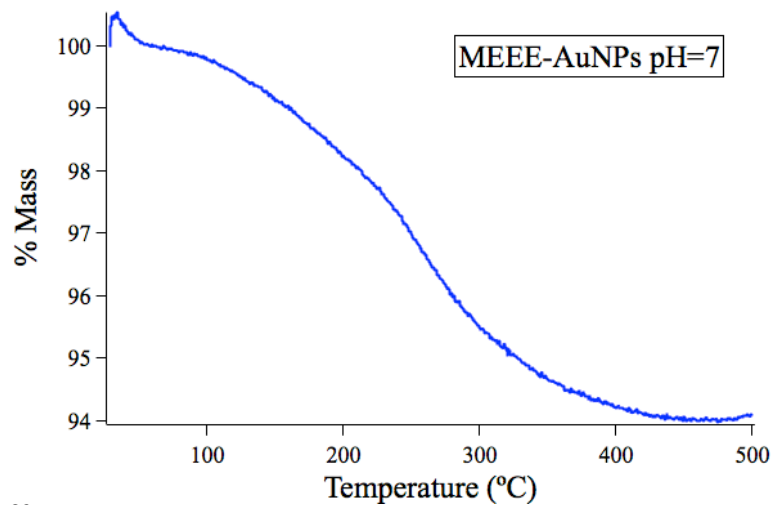
Figure S11. TGA data for AuNPs synthesized at Au(III) solution pH ~ 7 using MEE Bunte salt ligand.
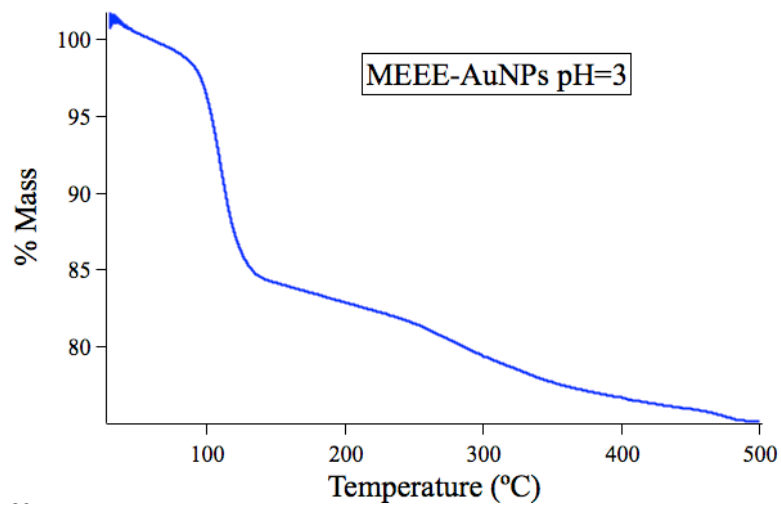
Figure S12. TGA data for AuNPs synthesized at Au(III) solution pH ~ 3 using MEEE Bunte salt ligand.

Figure S13. TGA data for AuNPs synthesized at Au(III) solution pH ~ 7 using MEEE Bunte salt ligand.
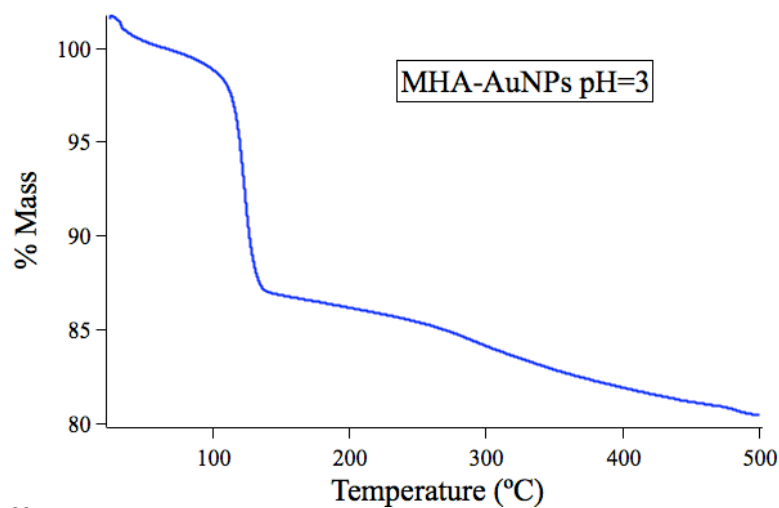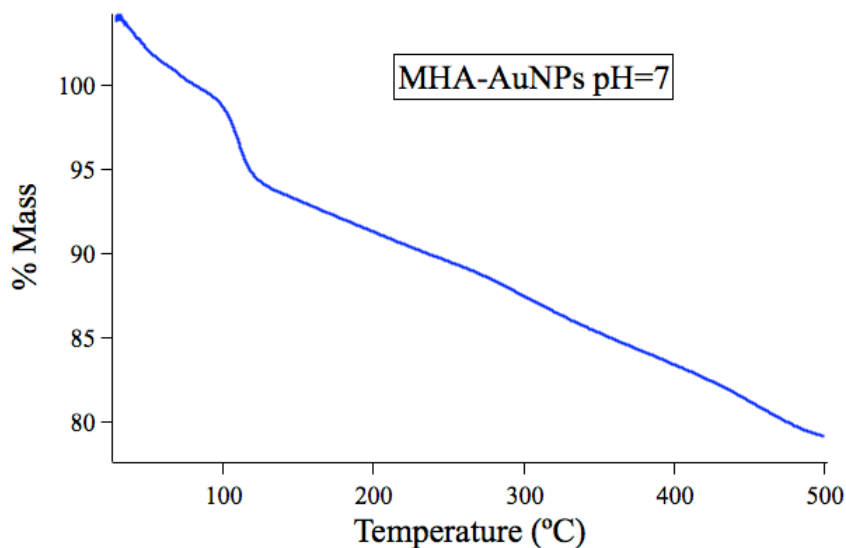

Figure S14. TGA data for AuNPs synthesized at Au(III) solution pH ~ 3 using MHA Bunte salt ligand.

Figure S15. TGA data for AuNPs synthesized at Au(III) solution pH ~ 7 using MHA Bunte salt ligand.

X-ray Photoelectron Spectroscopy. XPS spectra were collected to ensure that thiolate linkages had been formed on the AuNP surface for AuNPs from each of the working curves. Peaks at ~163 eV correspond to thiolate linkages to the AuNP surface. Peaks observed at ~169 eV correspond to small amounts of oxidized sulfur, either from atmospheric oxidation or residual thiosulfate trapped in the ligand shell. These oxidized peaks comprise less than 10% of the sulfur in all cases.
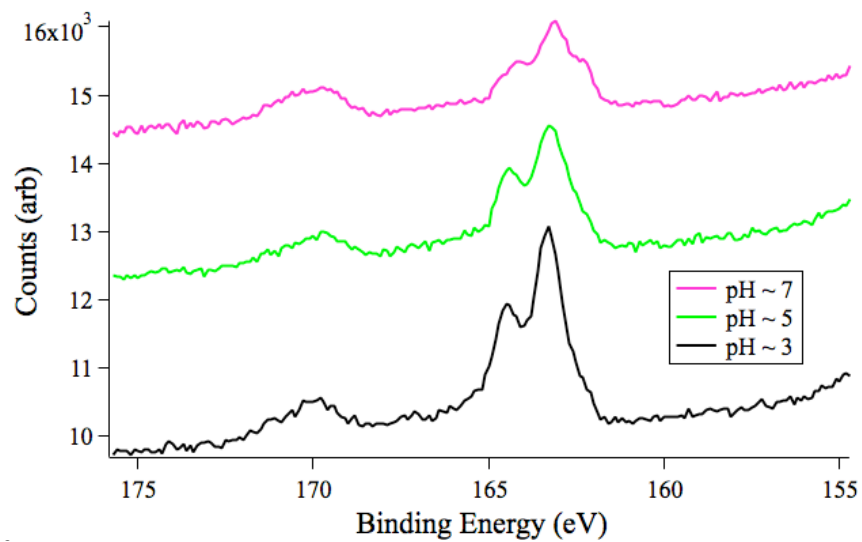
Figure S16. Representative XPS spectra for AuNPs synthesized using MEE Bunte salt ligand.
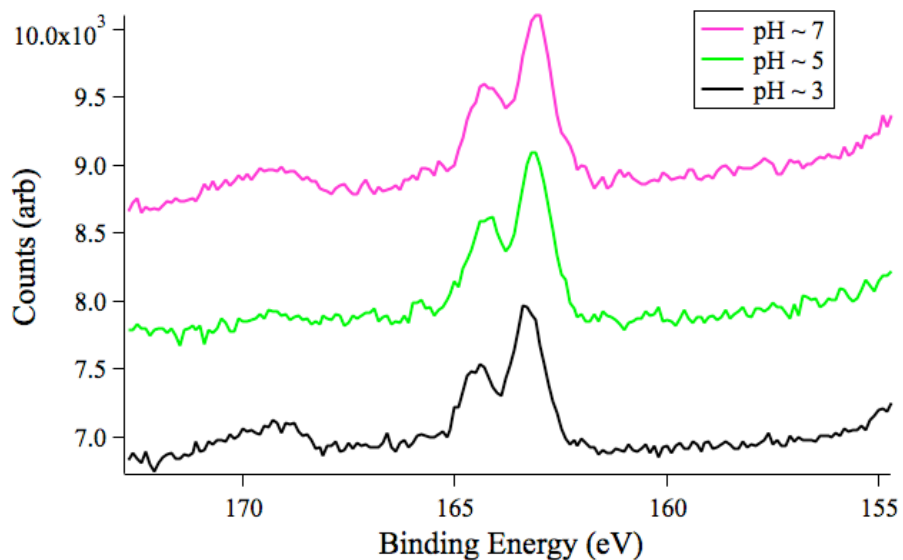

Figure S17. Representative XPS spectra for AuNPs synthesized using MEEE Bunte salt ligand.
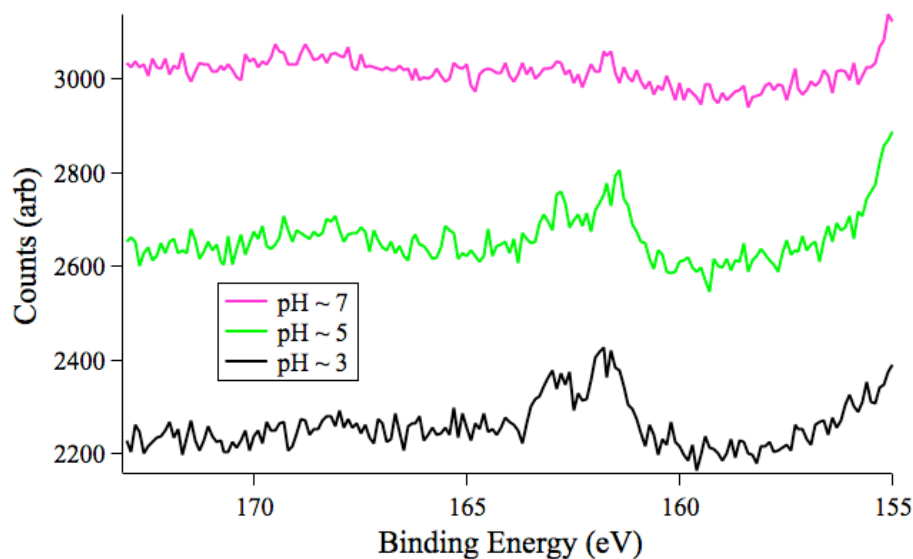
Figure S18. Representative XPS spectra for AuNPs synthesized using MHA Bunte salt ligand. Signal-to-noise is lower for these samples than the MEE- or MEEE-functionalized AuNPs due to a shorter collection time on the XPS instrument.

Determining Au(III) pH Dependence

UV/visible Spectroscopy. UV/vis was performed to corroborate other analyses and ensure that particles were stable in solution without flocculation. A plasmon lambda-max shift to higher wavelengths (~ 500 nm to ~ 520 nm across the range) as Au(III) solution pH increases was observed in all sample sets. This shift to higher lambda-max corresponds to observed increases in particle diameter by SAXS.
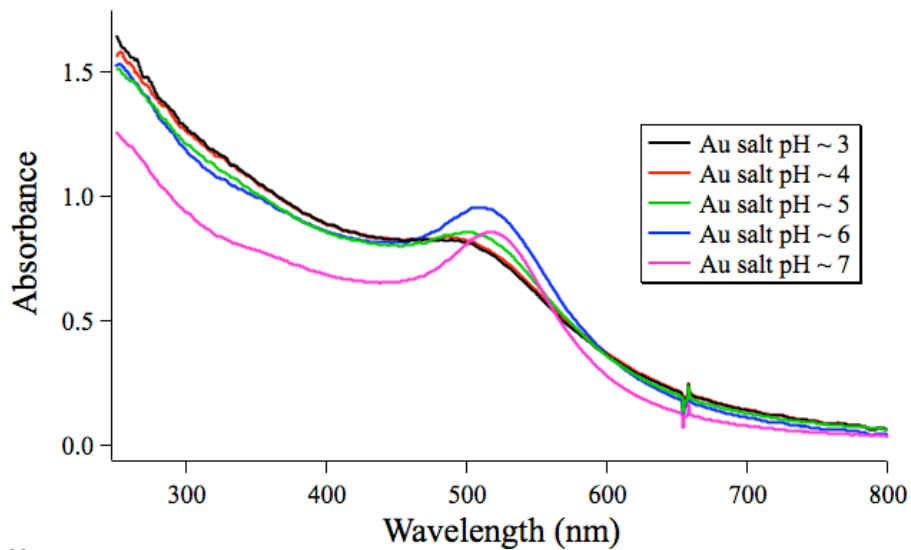
Figure S19. Representative UV/vis spectra of AuNPs synthesized with MEEE Bunte salt ligands. The samples shown were included in the sample set used to determine the MEEE Bunte salt working curve.
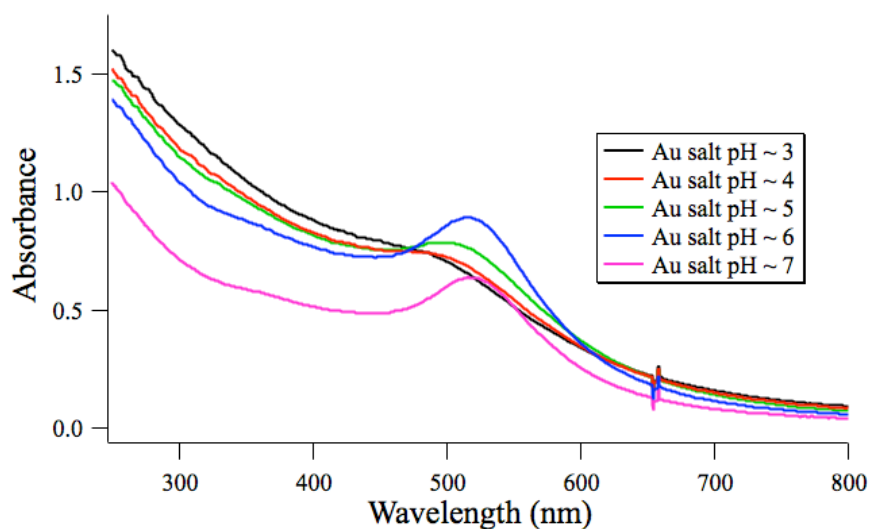
Figure S20. Representative UV/vis spectra of AuNPs synthesized with MEE Bunte salt ligands. The samples shown were included in the sample set used to determine the MEE Bunte salt working curve.
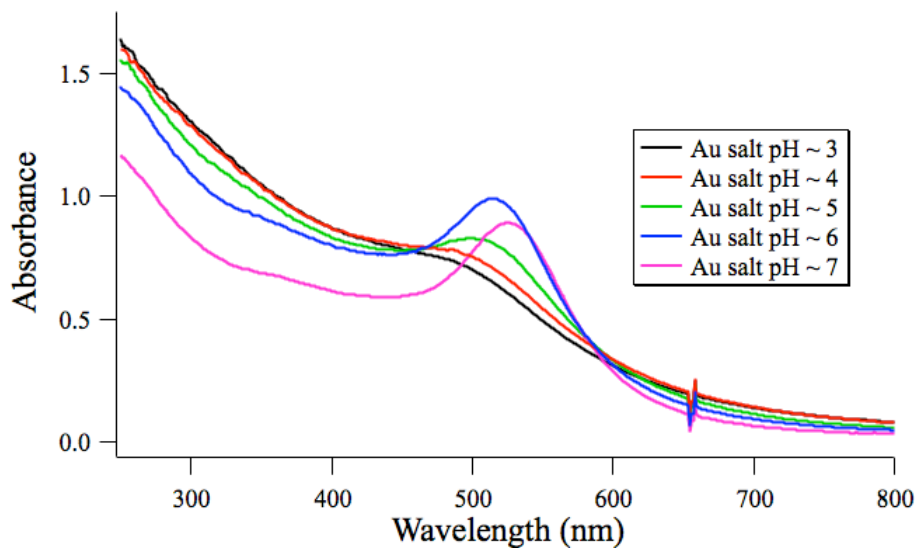
Figure S21. Representative UV/vis spectra of AuNPs synthesized with MHA Bunte salt ligands. The samples shown were included in the sample set used to determine the MHA Bunte salt working curve.
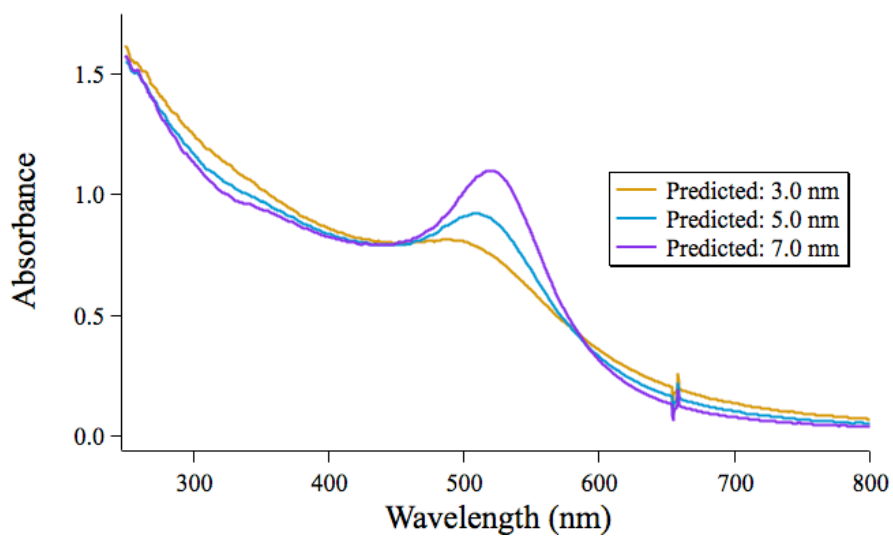
Figure S22. Representative UV/vis spectra of AuNPs synthesized with predictive sizes using MHA Bunte salt ligands. The samples shown were not included in the working curve fit, but match well to the observed trend (Figure 3).

Raw SAXS Data. All working curves were based off of modeled SAXS data. Below are representative SAXS patterns for each pH point on the three working curves shown in this study. Data points in these graphs represent raw data while solid traces represent models from which size distributions were determined. Traces are offset for clarity.
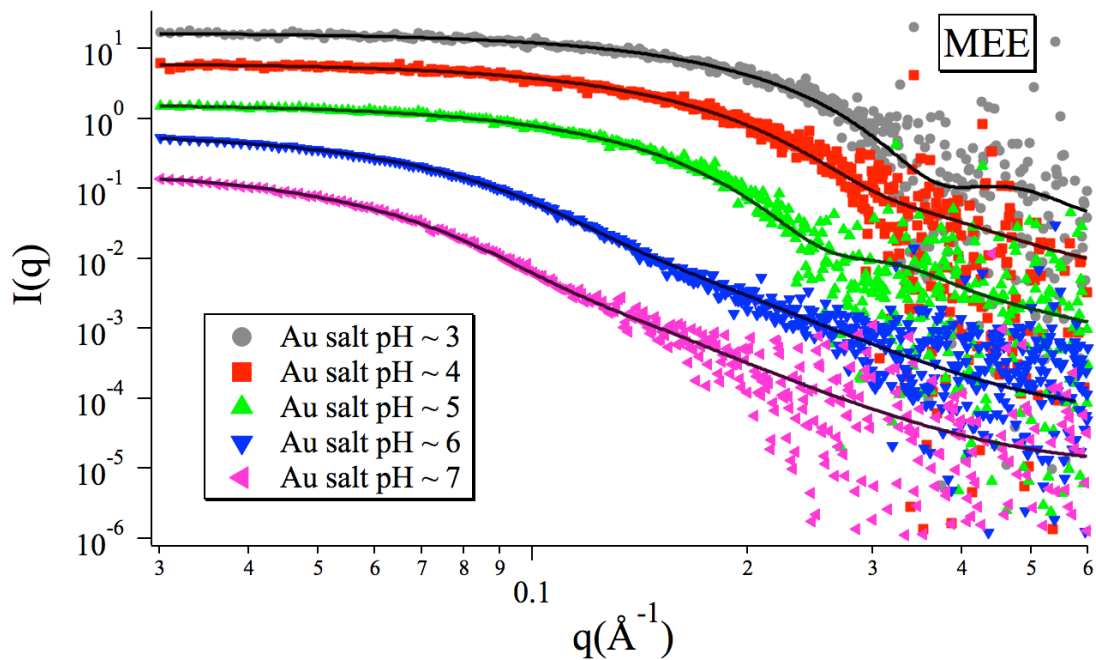
Figure S23. Raw SAXS data for the AuNP working curve using MEE Bunte Salt as ligand.
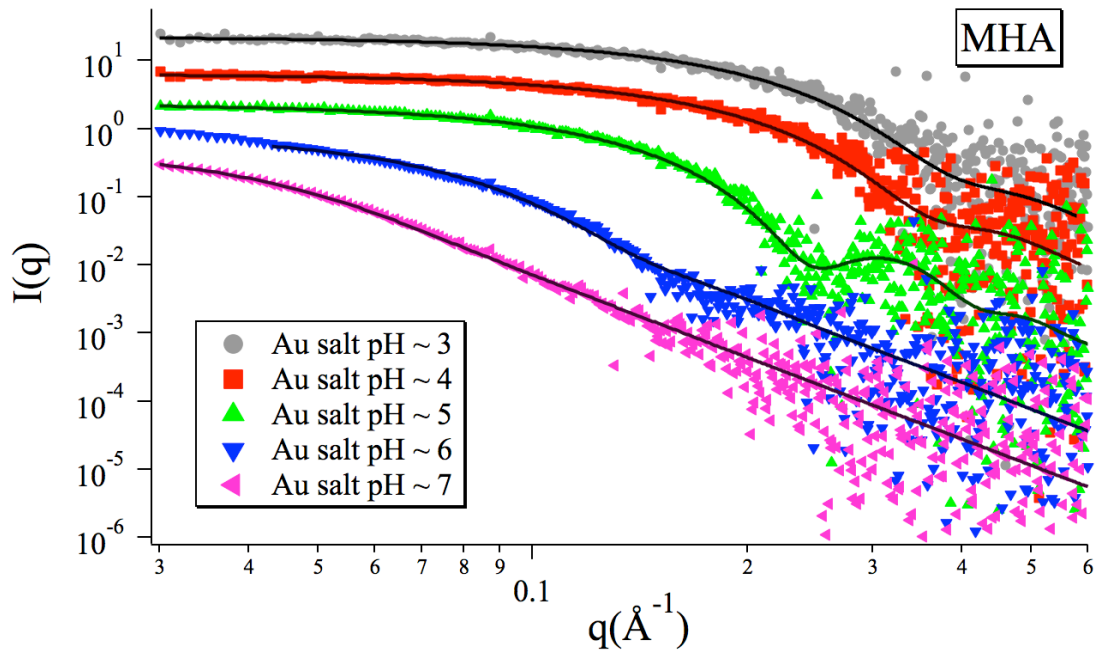
Figure S24. Raw SAXS data for the AuNP working curve using MHA Bunte Salt as ligand.
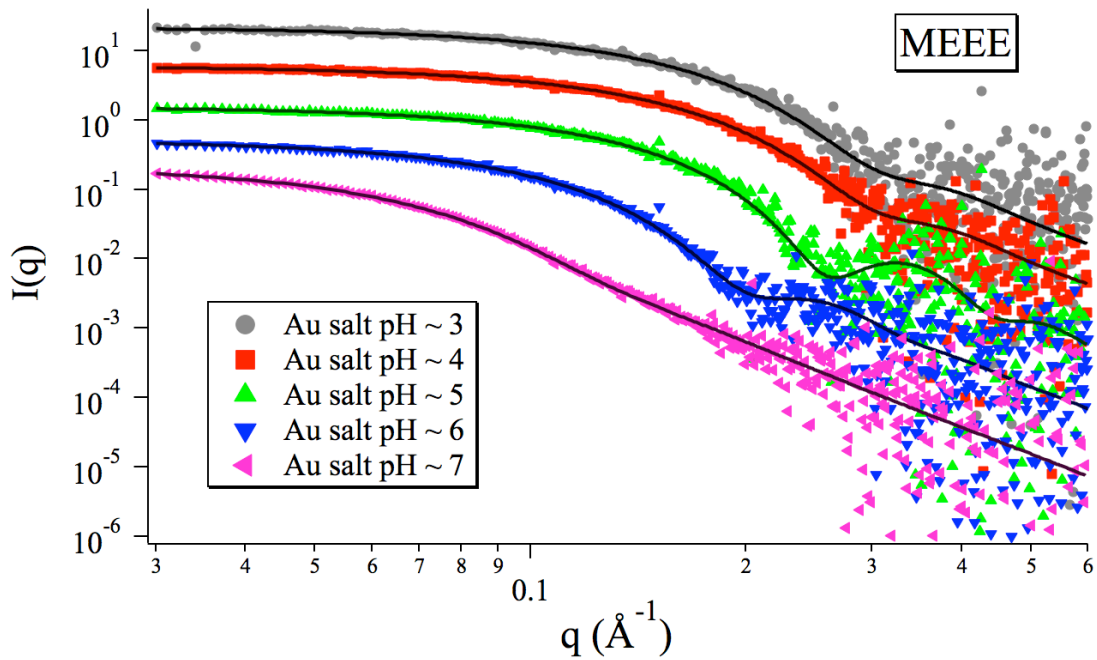
Figure S25. Raw SAXS data for the AuNP working curve using MEEE Bunte Salt as ligand.
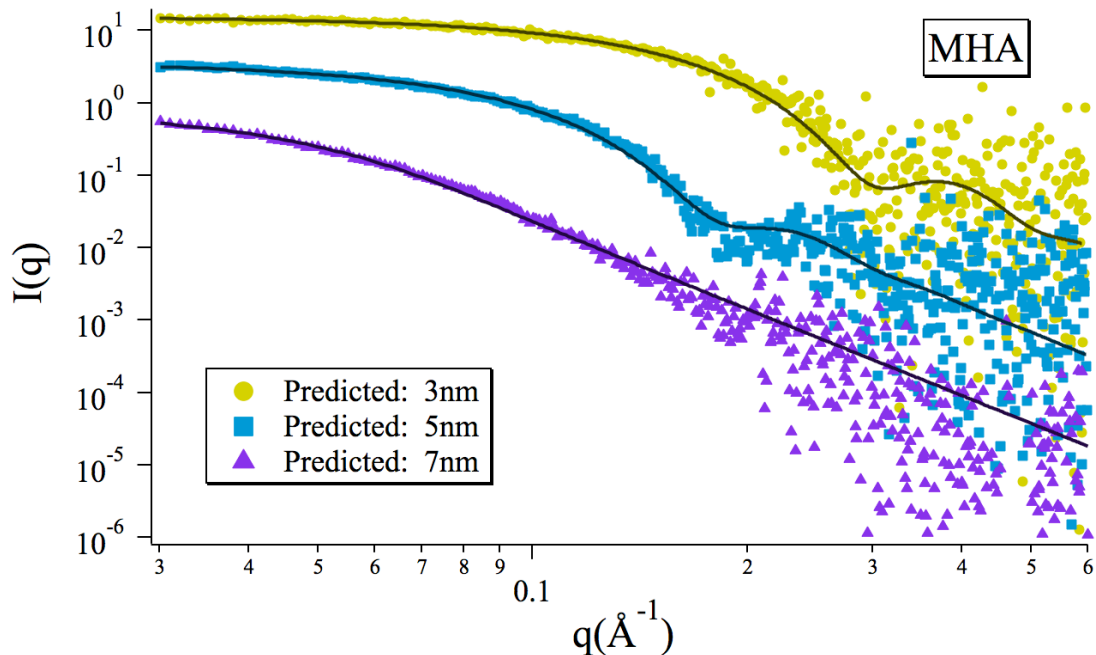
Figure S26. Raw SAXS data for the predictive AuNP syntheses (expected 3.0, 5.0, and 7.0 nm) using MHA Bunte Salt as ligand. Modeled AuNP diameters were found to be 3.0, 4.9, and 6.9 nm.

Working Curve Functions. Nanoparticle core sizes were determined by SAXS for each sample produced for a given ligand across the range of pH from 3 to 7. Smooth working curves through these data were produced using a 3-variable polynomial function. For the following, equation (1) corresponds to the MHA ligand working curve while equations (2) and (3) correspond to MEE and MEEE ligand working curves, respectively:

$$D = 0.486(x^2) - 3.09\text{e-}2(x) + 7.12 \tag{1}$$

$$D = 0.366(x^2) - 2.26\text{e-}2(x) + 5.94 \tag{2}$$

$$D = 0.0716(x^3) - 0.722(x^2) + 2.60(x) - 0.410 \tag{3}.$$

D represents average AuNP core diameter as determined by SAXS. The value x represents the Au(III) solution pH. Interested readers should note that size trends using other ligands might fit functional forms other than the polynomial fits utilized here.

Fitted curves, however, should be smooth with no local minima or maxima between data points. To determine the appropriate amount of NaOH to add to a 30 mL solution of 5.0 mM HAuCl₄, a titration using 1.0 M NaOH was performed. Corresponding Au(III) solution pH values for NaOH additions are listed below in Table S3. Working curves were based on AuNP diameter vs. Au(III) solution pH. This titration was used to determine appropriate volumes of NaOH to add to adjust Au(III) solution pH to desired values.

Table S3. Titration of 1.0 M NaOH into 30 mL of 5.0 mM HAuCl₄.

Vol. 1M NaOH (uL)	Au(III) pH	Vol. 1M NaOH (uL)	Au(III) pH	Vol. 1M NaOH (uL)	Au(III) pH
0	2.47	140	3.09	280	4.53
10	2.47	150	3.16	290	4.64
20	2.5	160	3.24	300	4.78
30	2.53	170	3.33	310	4.87
40	2.57	180	3.43	320	4.98
50	2.6	190	3.54	330	5.04
60	2.64	200	3.68	340	5.17
70	2.68	210	3.76	350	5.26
80	2.72	220	3.87	400	5.75
90	2.77	230	3.98	450	6.17
100	2.82	240	4.09	500	6.59
110	2.88	250	4.2	550	7.02
120	2.94	260	4.31		
130	3	270	4.42		

Individual working curves with polydispersities. Here each working curve is shown individually to demonstrate predictive ability and observed polydispersities across the pH range. Working curve data points are solid and predictive data points are open. For each data point, 3 syntheses were performed where corresponding SAXS size analyses were averaged to determine average diameters and standard deviations.
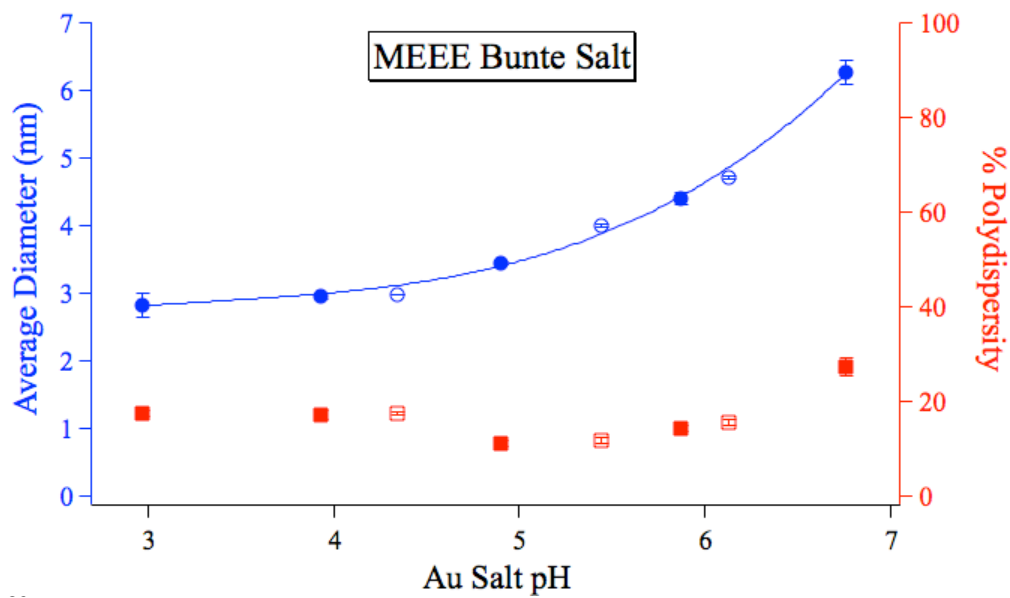
Figure S27. Combined SAXS data for AuNP working curve using MEEE Bunte salt as ligand.

120
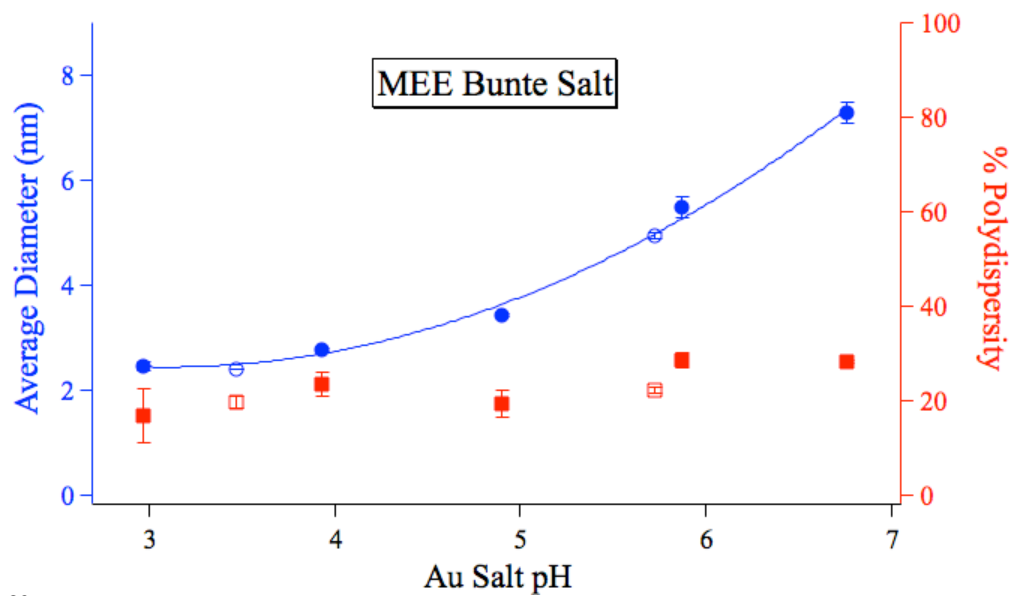
Figure S28. Combined SAXS data for AuNP working curve using MEE Bunte salt as ligand.
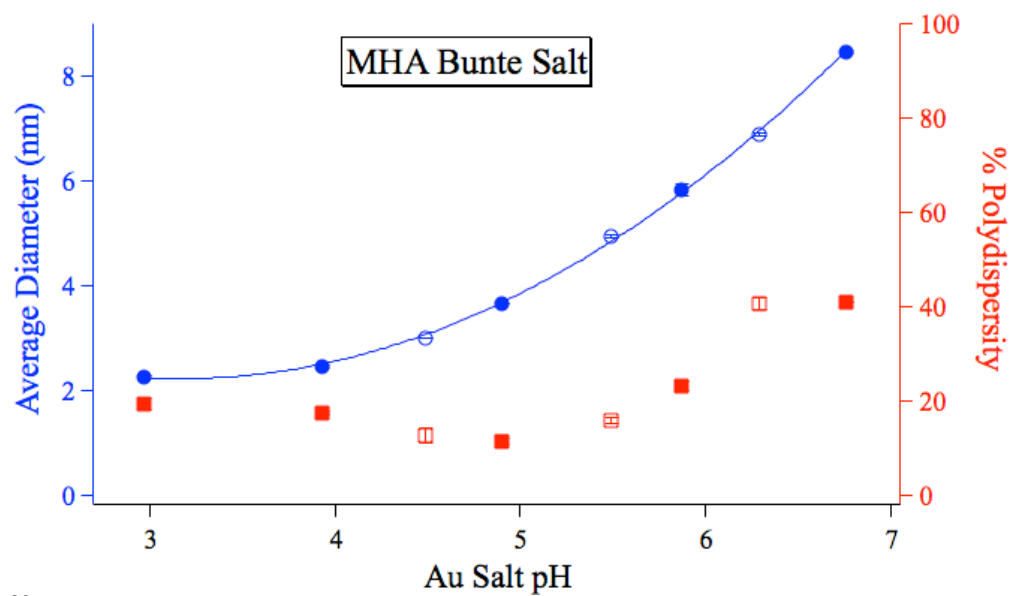
Figure S29. Combined SAXS data for AuNP working curve using MHA Bunte salt as ligand.
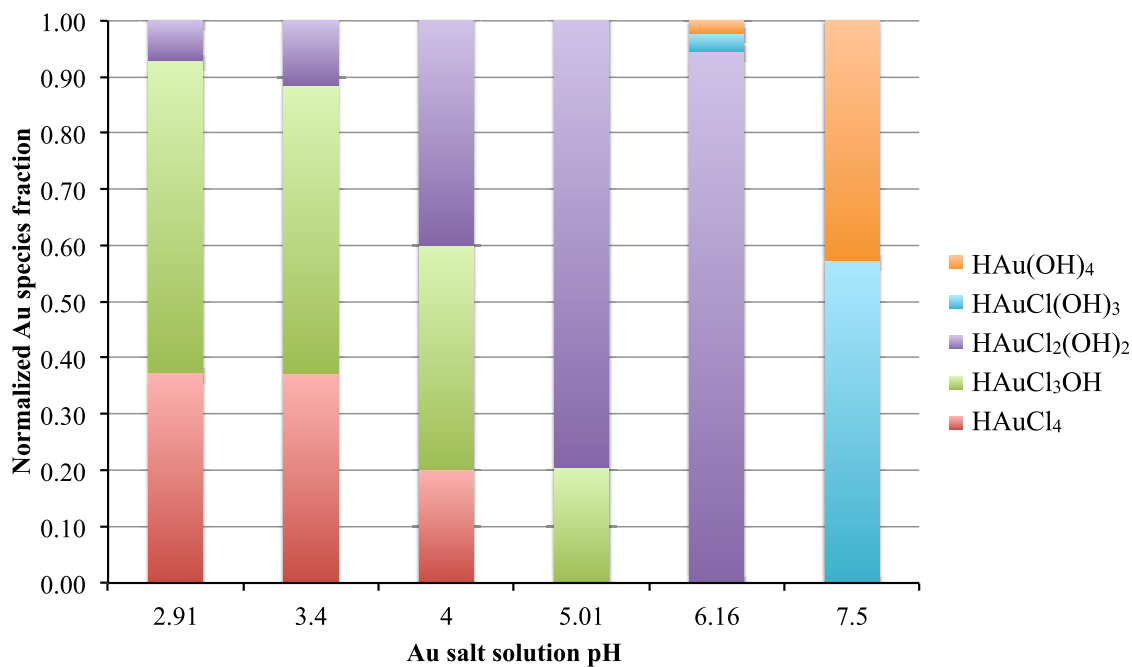
Figure S30. Normalized ratios of Au(III) species at varied pH, determined from ion chromatography by Wang et al.[7] Species with more chloro ligands exhibit higher reduction potentials and contribute more to AuNP formation.

Attempts to Vary Core Size in the Presence of Thiols and Disulfides

AuNPs were synthesized in flow using MEEE thiol ligand across the Au(III) pH range of interest (pH ~ 3 - 7) to determine if particle core size varied. AuNPs made in the presence of disulfide were only synthesized at extremes of this pH range. MEEE thiol was synthesized according to known procedures.[8] Briefly, 2 molar equivalents of thiourea were added to 1 equivalent of 2-(2-chloroethoxy)ethanol in 40 mL nanopure water with Ar(g) bubbling through solution. The solution was refluxed for 20 hours, then 20 mL of 5 M KOH was added and the solution was allowed to reflux for another 3 hours. The solution was then brought to pH ~ 1 with HCl. The acidified solution was extracted with

122

chloroform, then the organic layer was extracted with brine solution. Chloroform was removed in vacuo. A 1 mM solution of MEEE thiol in sparged nanopure water was used as ligand solution in the described microfluidic synthesis (See Experimental Details above). This solution was then left open to air at pH = 10 for 48 hours to generate a 0.5 mM solution of MEEE disulfide. A second, 1 mM disulfide solution was also made in this fashion.
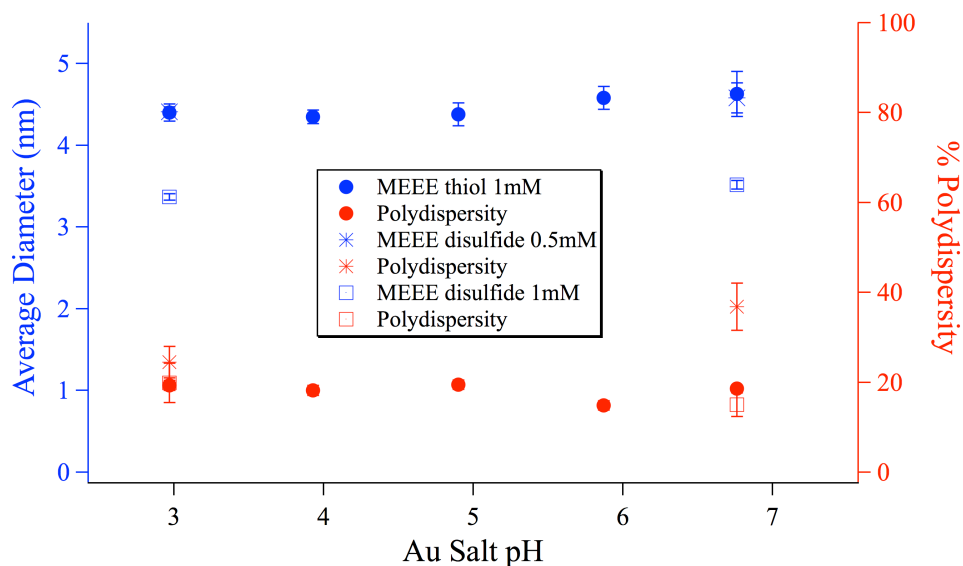
Figure S31. SAXS data of AuNPs synthesized in a microfluidic system across the Au(III) solution pH range of interest. No size selectivity is observed across this pH range. All syntheses performed with 1 mM MEEE thiol or 0.5 mM MEEE disulfide produce d_{CORE} ~ 4.5 nm AuNPs, With a 1 mM ligand solution of MEEE disulfide, smaller (d_{CORE} ~ 3.5 nm) AuNPs are generated than with 0.5 mM disulfide solution. Note that AuNPs made with these ligands show no significant core size variation across this pH range while all Bunte salts investigated show significant differences in core diameters.
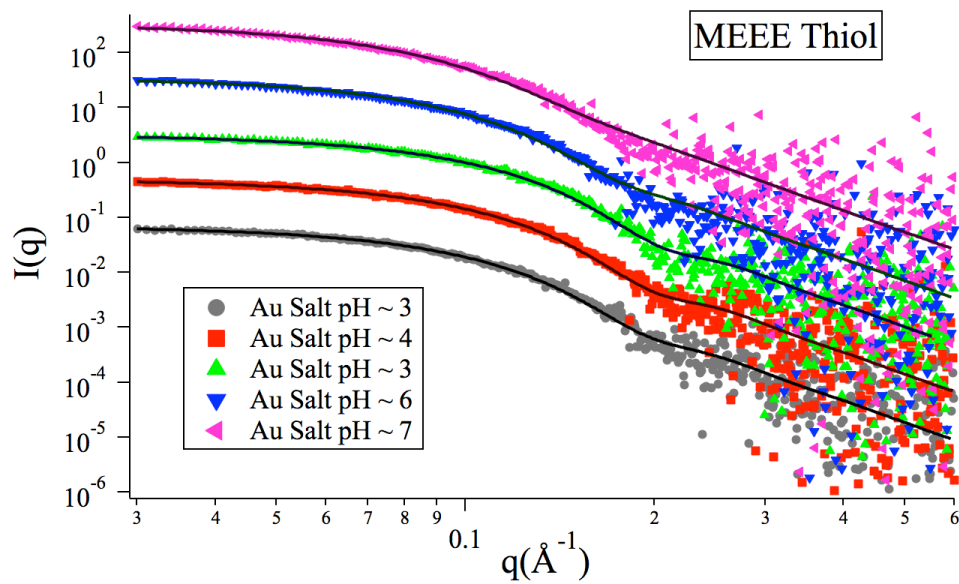
Figure S32. Raw SAXS data for AuNPs synthesized with MEEE thiol across Au(III) pH range. Models of these patterns yield average AuNP diameters that are very similar across the pH range. This result is surprising in comparison to AuNPs synthesized with analogous Bunte salt ligands where large differences in AuNP diameter are observed across this range.
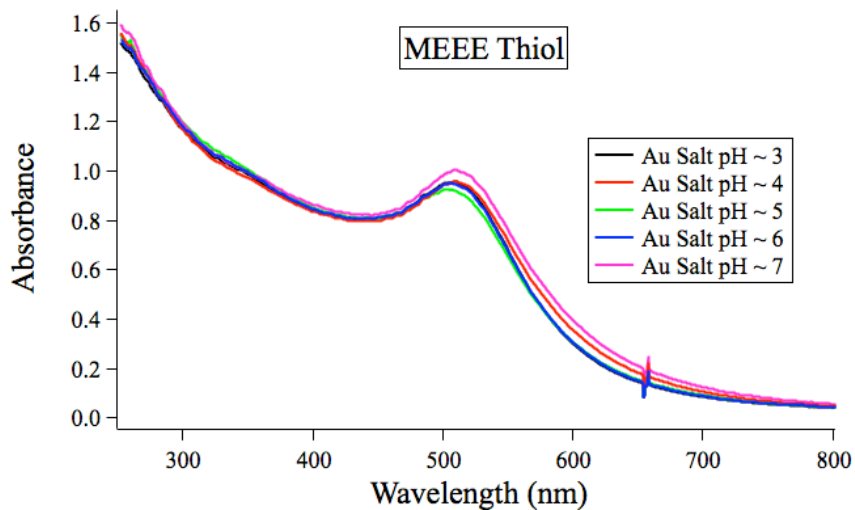
Figure S33. UV/vis spectra for AuNPs synthesized with MEEE thiol across the range of Au(III) pH ~ 3 - 7. Minimal differences in plasmon lambda max correlate well to similar observed AuNP sizes determined by SAXS.
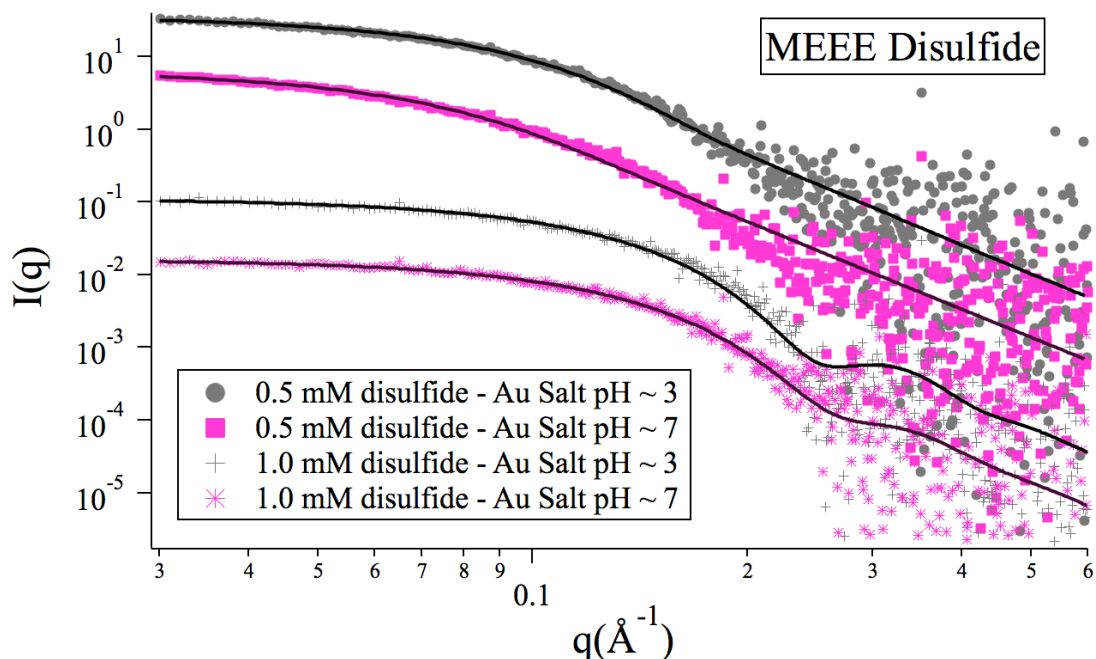
Figure S34. Raw SAXS data for AuNPs synthesized with two different concentrations of MEEE disulfide at two Au(III) pH values. Models of these patterns yield average AuNP diameters that are very similar at different pH values when the same ligand concentration is used.
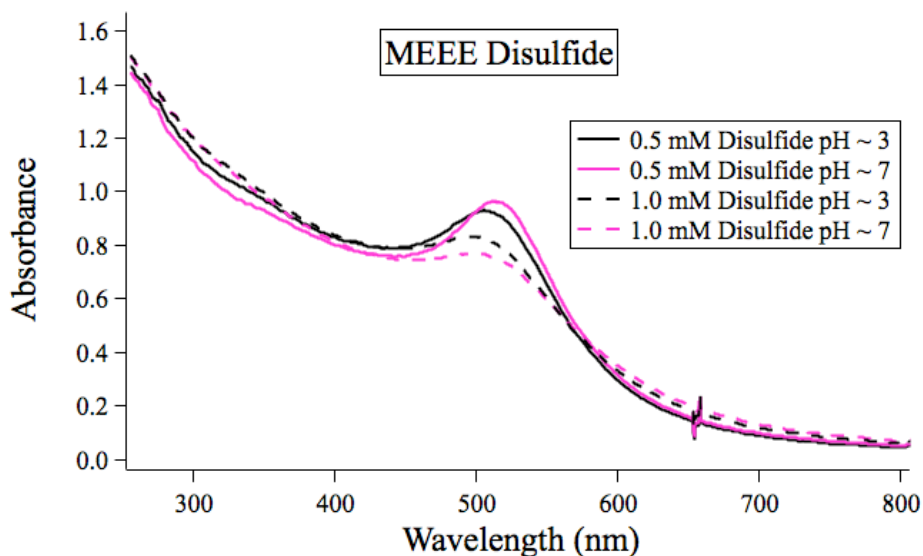
Figure S35. UV/vis spectra for AuNPs synthesized with MEEE disulfide at Au(III) pH ~ 3 and 7. Minimal differences in plasmon lambda max correlate well to similar observed AuNP sizes determined by SAXS.

Comparison of Batch and Microfluidic Syntheses
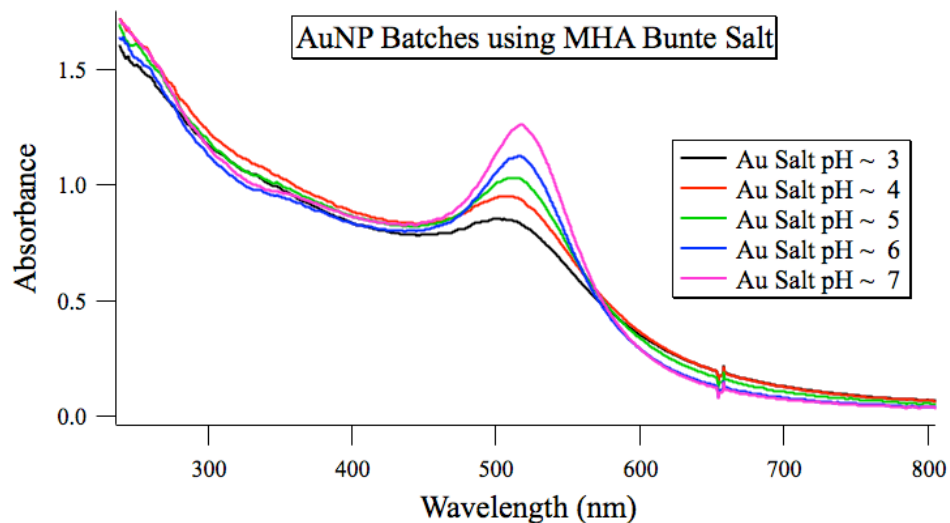
Figure S36. Selected UV/visible spectra for AuNPs synthesized in 80 mL batches using MHA Bunte Salt as ligand. A clear size trend, evidenced by increasing wavelength of the plasmon absorbance lambda-max, exists across the pH range, with higher Au(III) solution pH's resulting in larger AuNPs.

SAXS Working Curve for AuNPs Made in Batch

SAXS data were collected for AuNPs synthesized in 80 mL batches. For each data point, 3 syntheses were performed where corresponding SAXS size analyses were averaged to determine average diameters and standard deviations.
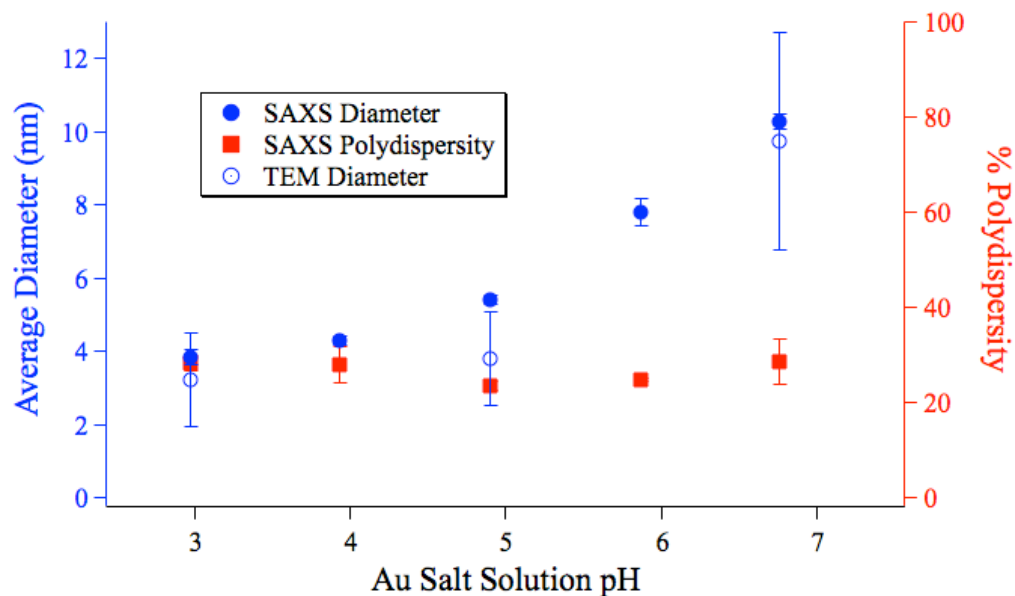
Figure S37. Combined SAXS data for batch AuNP working curve using MHA Bunte salt as ligand. These data correlate well to observed UV/vis trend. Sizes determined by TEM show much larger error bars than analogous SAXS analyses.

Comparison of Variability in AuNP Core Size for Batch and Flow Syntheses

AuNPs were synthesized in (1) batch reactions performed by a single researcher, (2) batch reactions performed by 3 different researchers, and (3) microfluidic reactions by multiple researchers. AuNP size distributions were determined by SAXS. Variability in core size is low when a single researcher performs batch syntheses in rapid succession, but rises dramatically when multiple researchers perform these batch syntheses. When syntheses are performed in a microreactor and the same stock solutions are utilized, researcher-dependent variables are eliminated and variability is much lower than for reactions performed in batch. Microfluidic reactions performed by single or multiple researchers yield consistent results between syntheses.

Table S4. Summary of AuNP core sizes for 9 different AuNP syntheses, using he MHA ligand, as determined by SAXS

Synthetic Method	SAXS AuNP Diameter (nm)	Diameter Standard Deviation
Single Researcher Batch Syntheses	A) 7.77	5%
	B) 7.45	
	C) 8.22	
Multiple Researcher Batch Syntheses	A) 7.87	18%
	B) 5.71	
	C) 8.17	
Microfluidic Syntheses	A) 5.73	2%
	B) 5.88	
	C) 5.92	

APPENDIX B

SUPPORTING INFORMATION FOR CHAPTER IV: RAPID DIRECT

SYNTHESIS OF WATER-SOLUBLE, MIXED MONOLAYER AZIDE

FUNCTIONALIZED GOLD NANOPARTICLES FOR USE AS CLICK

CHEMISTRY REAGENTS

Materials

All materials were used as received: $HAuCl_4 \cdot H_2O$ (99.9%) (Strem); 2-[2-(2-

chloroethoxy)-ethoxy]ethanol (99%), sodium borohydride (98%, caplets), Copper(I)

bromide (99.999%), 1-ethynyl-1-cyclohexanol (99%), (Aldrich); sodium hydroxide,

sodium thiosulfate (anhydrous), (Mallickandrot); sodium L-ascorbate (powder,

Bioreagent), dibenzocyclooctyne-PEG_4-Fluor 545 (DBCO-PEG_4-Alexafluor-545),

phenylacetylene (98%), ethynylferrocene (97%), (Sigma-Aldrich); thionyl chloride (99.5%)

(Acros), sodium azide (95%) (J.T. Baker); benzyltriethylammonium chloride (BTEAC,

99%) (TCI America); DBCO-PEG_4-OH, DBCO-NHS ester (Click Chemistry Tools).

The Bunte salt analog of 2-[2-(2-mercaptoethoxy)-ethoxy)ethanol (EG_3-BS) was

synthesized as previously reported.[x1] Column chromatography was performed using 40-

63 μM silia-P flash silica gel (Silicycle). Deionized water (18.2 MΩ·cm) was obtained

using a Barnstead Nanopure Diamond system. Flow nanoparticle syntheses were driven

using Kloehn syringe pumps (P/N 54022) and Kloehn 10 and 25 mL syringes. The flow

system was created using IDEX Teflon tubing (0.75 mm ID, WO# 0554152) and Teflon

T-mixers. Lengths of tubing were used in assembling the reactor, to keep residence and mixing constant for all flow rates.

Methods

Nanoparticle Core Size Determination using Small Angle X-ray Scattering (SAXS). Nanoparticle sizes resulting from the direct syntheses performed were determined in solution at synthesis concentrations using small angle X-ray scattering (SAXS). Briefly, NP samples were exposed to monochromated X-rays from a Long Fine Focal spot (LFF) sealed X-ray tube (Cu 1.54 Å) powered by a generator at 2 kW focused by multilayer optics, measured with a Roper CCD in a Kratky camera. The Anton Paar SAXSess, in line collimation mode, was set to average a minimum of 50 scans of 40 s exposures. The corresponding dark current and background scans were subtracted from the data before desmearing using the beam profile in Anton Paar SAXSQuant software. The size distribution of the sample was then determined by using the size distribution macro in the IRENA package.[ca-paper] The SAXS patterns were fit using the modeling II macro and best model fits were determined using a nonlinear least squares method, assuming spherical particles (confirmed with TEM), to yield a Gaussian size volume distribution binned by core diameter. For each sample, percent polydispersity was then also determined relative to the average core size.

TEM microscopy of Purified EG$_3$-azide / EG$_3$ (5:95)-AuNPs and EG$_3$-triazole-DBCO-1 / EG$_3$ (5:95)-AuNPs Samples for Analysis of Morphology. TEM analysis of purified nanoparticle samples was performed on a FEI Tecnai G2 Spirit TEM operating at 120 kV. AuNP samples were prepared for analysis by floating holey carbon TEM grids (Ted Pella) on top of a drop of diluted AuNP solution of either **EG$_3$-azide / EG$_3$ (5:95)-AuNPs** or

EG$_3$-triazole-DBCO-1 / EG$_3$ (5:95)-AuNPs for ~5 minutes. The grids were lifted from the drop and excess solution wicked away using a Kimwipe before being allowed to dry in ambient conditions prior to imaging.

NMR Spectroscopy of Purified Nanoparticle Samples for Analysis of Purity and of Decomposed Nanoparticles for Quantifying Mixed Ligand Compositions. Approximately 7-10 mg of purified lyophilized nanoparticles were redispersed in 0.6 mL D$_2$O or a D$_2$O/DMSO-d$_6$ mixture as specified in the experimental. An initial spectrum was acquired at 600 MHz with 128 scans and a relaxation delay of 1 s to confirm that all free ligands and synthetic byproducts were removed. The absence of sharp peaks (due to free ligands) and the presence of the broad peaks characteristic of quadrupolar broadening due to the size of the AuNPs indicated that all of the ligands were bound to the surface. Characterization of the bound mixed ligands before and after coupling reactions was initiated by adding approximately 2 mg of I$_2$ directly to the NMR tube. The mixture was shaken vigorously and allowed to react in ambient conditions for ~10-15 min. The solid I$_2$ was then removed from the NMR tube prior to acquiring another spectrum at 600 Mhz with 512 scans. All AuNP NMR spectra showed that the ligands had been oxidized to form the corresponding disulfides. Identification of characteristic peaks attributed to the coupled product was then performed to verify successful reactions.

UV-visible Spectroscopy of Purified EG$_3$-azide / EG$_3$ (5:95)-AuNPs and EG$_3$-triazole-DBCO-1 / EG$_3$ (5:95)-AuNPs. All measurements were performed using an HP 8453 UV-visible spectroscopy system. Absorbance of purified AuNPs solutions were measured in a quartz cuvette cleaned with aqua regia and rinsed copiously with nanopure water between all measurements.

131

Fluorescence Spectroscopy of Purified EG₃-azide / EG₃ (5:95)-AuNPs and EG₃-triazole-DBCO-1 /

EG₃ (5:95)-AuNPs to Verify the Efficacy of the Strain Promoted AAC Reaction. Nanoparticle

solutions were first diluted with nanopure water to give yield absorbance at λ_{max} of 0.6.

All fluorescence measurements were preformed using the Horiba Jobin Yvon Fluoromax-

4 spectrofluorometer with excitation at 525 nm and emission collected from 540-700 nm,

slit widths were set to 5 nm. The quartz cuvette was cleaned with aqua regia and rinsed

copiously with nanopure water in between all measurements.

Experimental

Synthesis of sodium S-(2-(2-(2-azidoethoxy)ethoxy)ethyl) sulfothioate (EG₃-azide-BS)
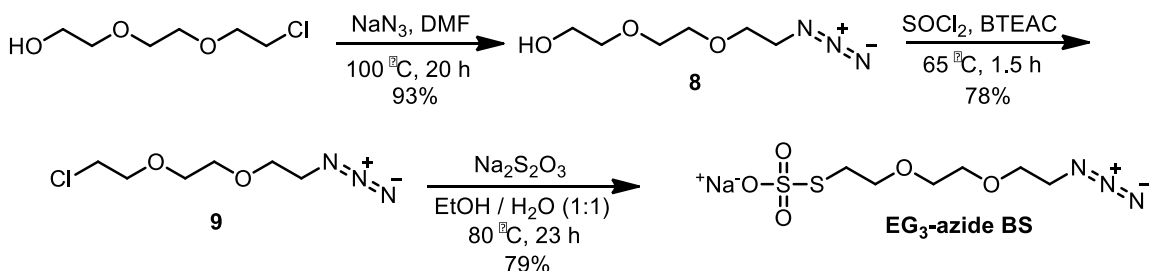
Scheme S1. Synthetic route to a PEG tethered azide functionalized Bunte salt

1-azido-2-(2-(2-chloroethoxy)ethoxy)ethane (**8**). 2-[2-(2-chloroethoxy)-ethoxy]ethanol

(4.00 g, 0.0237 mol) was dissolved in anhydrous DMF (100 mL) under N₂. Sodium azide

(3.07 g, 0.0472 mol) was added and the mixture was heated to 100 °C for 20 h while

stirring. The mixture was cooled down to r.t. and DMF removed under reduced pressure

in a rotary evaporator condensed over NaOH pellets to trap any HN_3 potentially produced.[1] The crude residue was then suspended in diethyl ether (100 mL), filtered through a medium fritted funnel, and concentrated *in vacuo* to yield **8** (3.85 g, 93%) as a colorless liquid. ^{1}H-NMR (300 MHz, CDCl$_3$): δ = 3.62-3.77 (m, 10H), 3.42 (t, 2H), 2.28 (t, 1H).

1-azido-2-(2-(2-chloroethoxy)ethoxy)ethane (**9**).[2] A mixture of azide **8** (3.50 g, 0.0200 mol) and benzyltriethylammonium chloride (BTEAC) (0.137 g, 0.0600 mmol) were heated in a 3-neck RB flask to 65 °C. Thionyl chloride (4.78 g, 0.0402) was then added dropwise from an addition funnel equipped with a pressure-equalization arm, and the reaction mixture was further stirred at 65 °C for 1.5 h while maintaining a continuous N_2 flow (to remove HCl generated).The mixture was let cool to r.t. and excess thionyl chloride removed by rotary evaporation. The crude product was suspended in phosphate buffer (50 mM, pH = 7.0, 15 mL) and extracted with 1:1 EtOAc/hexane (15 mL total). The organic layer was washed with phosphate buffer (4 x 15 mL), dried with Na_2SO_4, filtered using a coarse fritted funnel, and concentrated *in vacuo* to yield **9** (3.02 g, 78 %) as a yellow liquid. ^{1}H-NMR (300 MHz, CDCl$_3$): δ = 3.64-3.81 (m, 10 H), 3.42 (t, 2H).

S-(2-(2-(2-azidoethoxy)ethoxy)ethyl) sulfothioate (**EG$_3$-azide-BS**). Chloro compound **9** (2.51 g, 0.0130 mol) was dissolved in a 4:3 EtOH/H$_2$O (70 mL total) mixture. Anhydrous sodium thiosulfate (2.47 g, 0.0156 mol) (dissolved in 10 mL deionized water) was added over ~ 2 min. The resulting mixture was heated at 80 °C for 23 h. Upon letting cool to r.t., EtOH and H$_2$O were removed by rotary evaporation. The crude material was dissolved in CH$_3$CN (20 mL) to precipitate salts which were subsequently removed by filtering using a medium fritted funnel. CH$_3$CN was removed by rotary evaporation to

133

produce a crude yellow liquid which was then redissolved in deionized H_2O (10 mL) to separate unreacted starting material as a yellow oily residue. The water solution was decanted and subsequently filtered through a fine fritted funnel to remove residual trace starting material. Concentration *in vacuo* produced **EG₃-azide-BS** (2.99 g, 79%) as an oily pale yellow solid. ^{1}H-NMR (300 MHz, D_2O): δ = 3.78 (t, 2H), 3.57-3.65 (m, 6H), 3.39 (t, 2H), 3.18 (t, 2H).
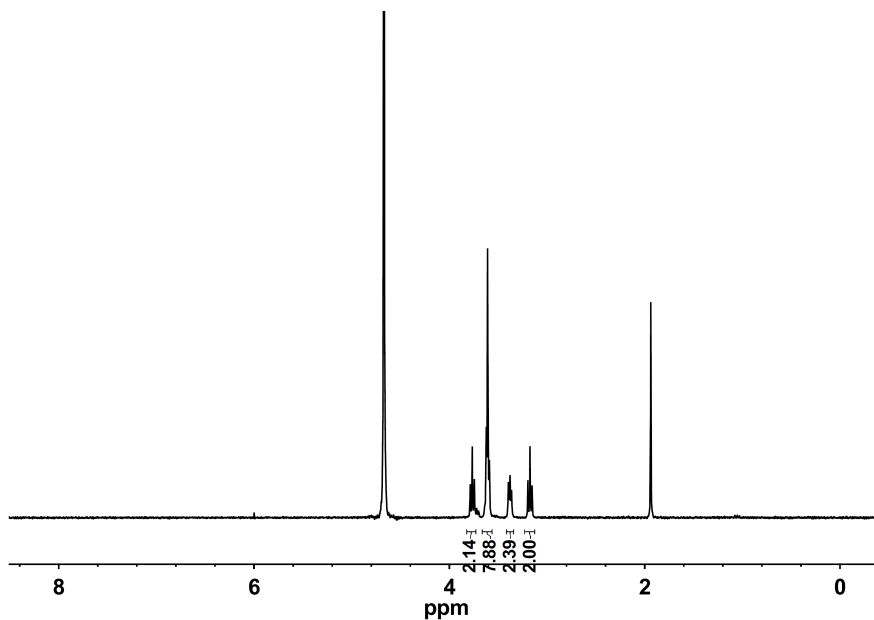
Figure S1. ^{1}H-NMR spectrum of **EG₃-azide-BS (D_2O).**

EG₃-azide / EG₃ (5:95)-AuNP and EG₃-azide / EG₃ (10:90)-AuNP characterization

Calculation of moles of azide ligand for a given mass of EG₃-azide / EG₃ (5:95)-AuNPs. For a 3.5 nm AuNP, there are 1580 Au atoms (obtained from $N_{Au} = 10^{((LOG(diameter-0.2177)-LOG(0.225))/0.3639)^3}$ and 180 EG₃ ligands (#EG₃ ligands = (surface

area*0.826(maximum packing density on a sphere))/(0.1775 nm^2)(footprint of an EG$_3$ molecule)[4]. Therefore, the *average* molecular weight for 3.5 nm **EG$_3$-azide / EG$_3$ (5:95)-AuNPs** [Au$_{1580}$(EG$_3$-azide)$_9$(EG$_3$)$_{171}$] is 3.41 x 10^5 g/mol. The moles of AuNPs can then be calculated from g$_{AuNPs}$*(1 mol / 3.41 x 10^5 g $_{AuNPs}$). For every mole of AuNPs, there are 9 molar equivalents of azide-ligand, therefore mol$_{AuNPs}$*9 = mol$_{azides}$.
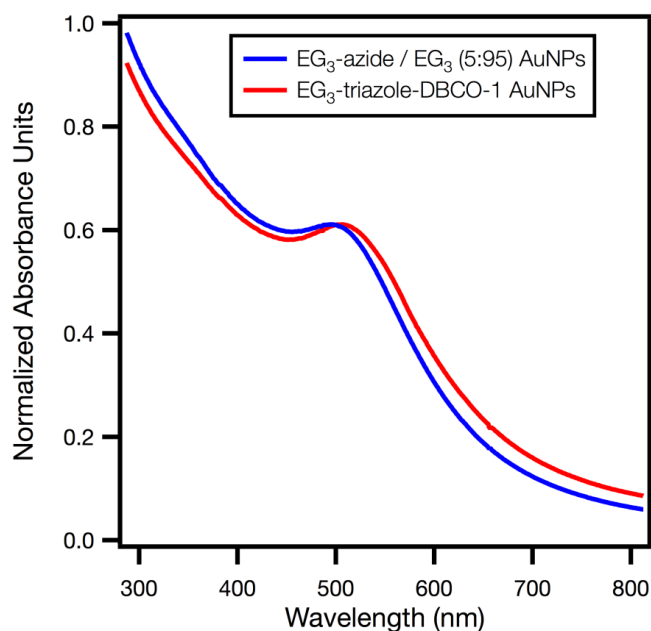
Figure S2. UV-vis of AuNPs before (**EG$_3$-azide / EG$_3$ (5:95)-AuNPs**) and after (**EG$_3$-triazole-DBCO-1**) coupling reactions.

Table S1. EG$_3$-azide / EG$_3$ (5:95) – Multiple batches of AuNPs, core size determined by SAXS.

	Diameter (nm)	Polydispersity (nm)	% Polydispersity
Batch 1	3.5	0.4	12%
Batch 2	3.7	0.3	9%

Batch 3	3.5	0.4	13%
Batch 4	3.4	0.5	14%
Batch 5	3.5	0.5	14%
Batch 6	3.5	0.5	13%
Average	**3.5**	**0.4**	**13%**
Std Dev	*0.08*	*0.05*	

Table S2. EG$_3$-azide / EG$_3$ (10:90) – AuNPs core size determined by SAXS

	Diameter (nm)	**Polydispersity (nm)**	**% Polydispersity**
Batch 1	3.5	0.5	15%
Batch 2	3.5	0.6	16%
Batch 3	3.5	0.5	14%
Batch 4	3.5	0.5	15%
Batch 5	3.6	0.3	8%
Batch 6	3.5	0.4	12%
Batch 7	3.5	0.5	14%
Batch 8	3.5	0.5	14%
Batch 9	3.5	0.5	13%
Average	**3.5**	**0.5**	**13%**
Std Dev	*0.04*	*0.07*	
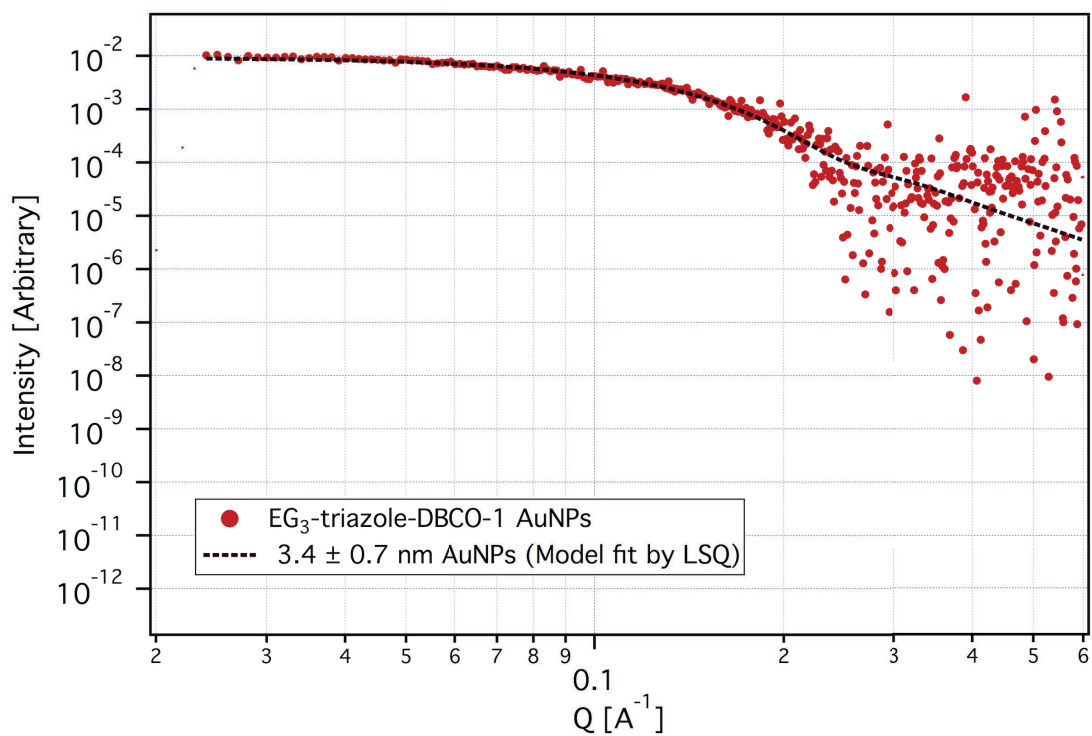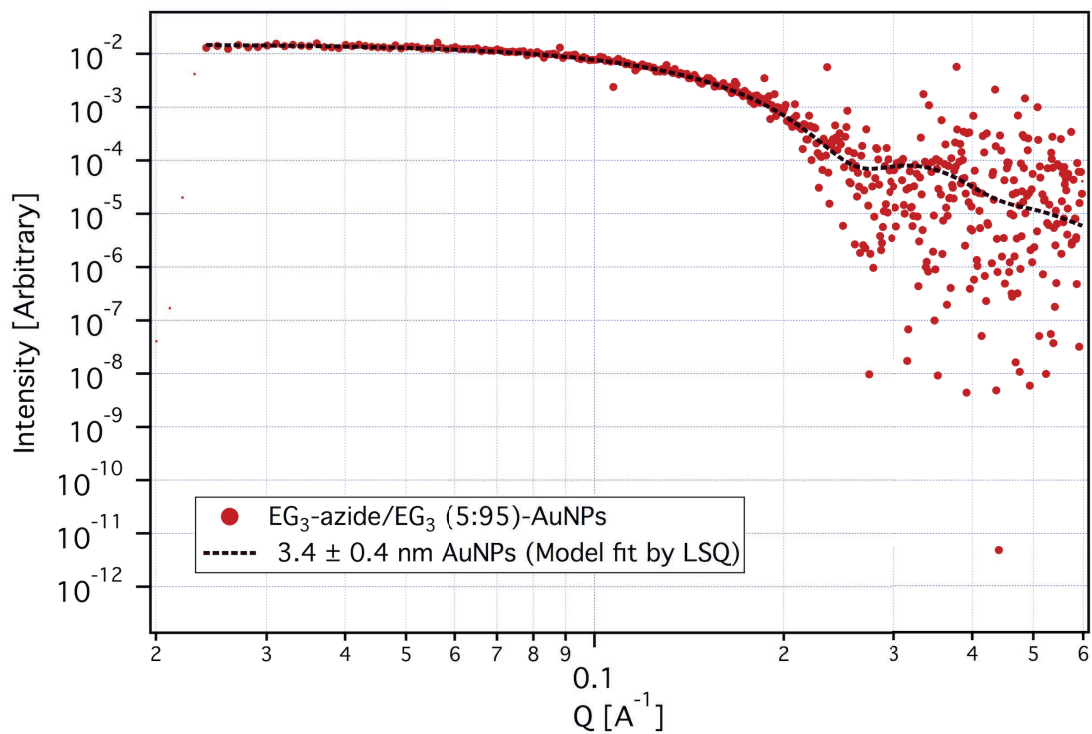
Figure S3. Raw SAXS patterns and overlaid LSQ model fits for AuNPs before (**EG₃-azide / EG₃ (5:95)-AuNPs**, top) and after (**EG₃-triazole-DBCO-1**, bottom) the coupling reaction showing no core growth during the reaction or subsequent purification.
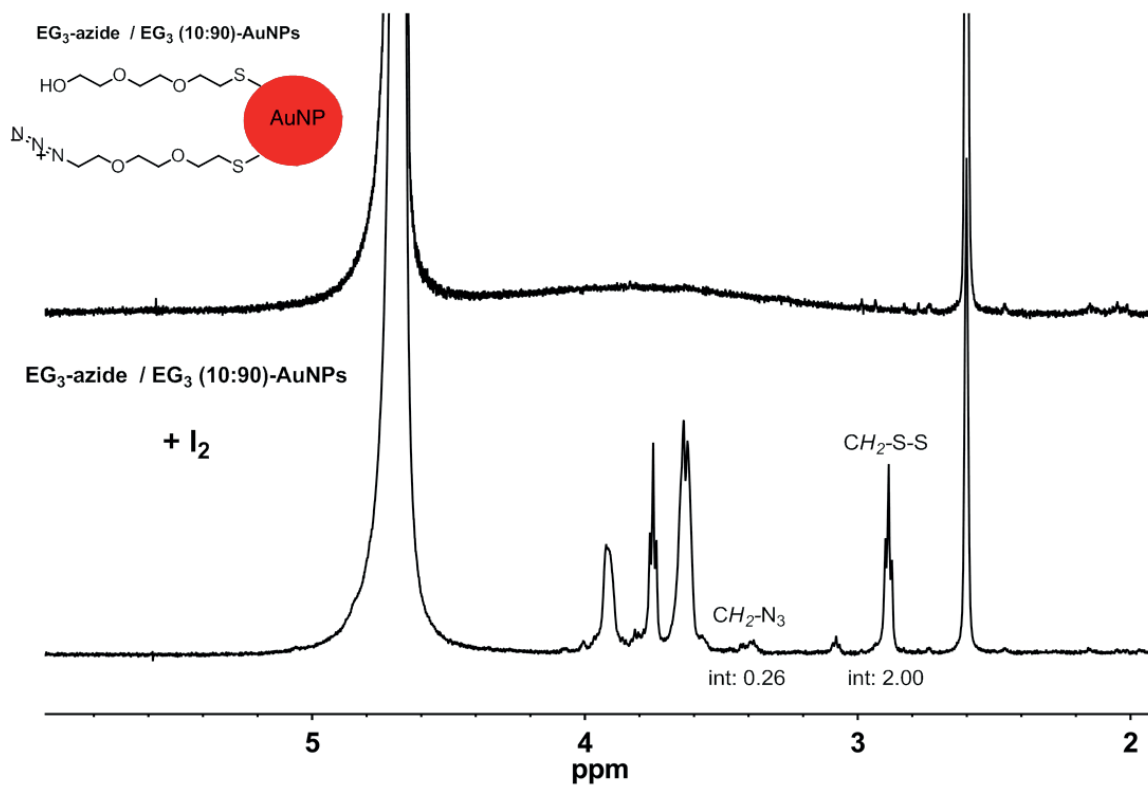
Figure S4. ^{1}H-NMR, 600 MHz, D_2O/DMSO-d_6 (80:20) before and after I_2-decomposition
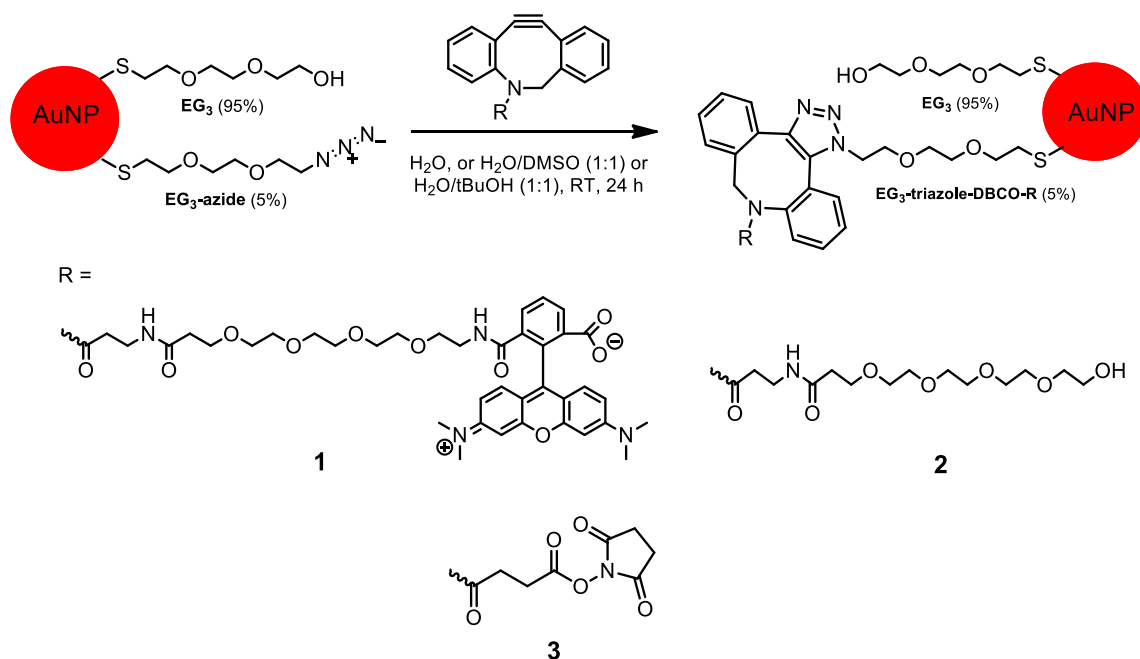
Figure S5. Copper-free 1,3-dipolar cycloadditions involving **EG₃-azide / EG₃ (5:95)-AuNPs** and strained alkynes (**1-3**)

EG₃-triazole-DBCO-1 / EG₃ (5:95)-AuNPs. Lyophilized **EG₃-azide / EG₃ (5:95)-AuNPs** (15.59 mg, 4.1 x 10⁻⁷ mol EG₃-azide) were dissolved in H_2O (1.72 mL) in a scintillation vial. DBCO-PEG₄-Alexafluor-545 (1.40 mg, 1.5 x 10⁻⁶ mol) (dissolved in 0.28 mL H_2O) was added to the vial, capped, and the mixture was stirred at room temperature for 24 hours. The reaction mixture was then purified and lyophilized to isolate **EG₃-triazole-DBCO-1 / EG₃ (5:95)-AuNPs** as a black powder. Confirmation of the successful coupling reaction was obtained by I_2 decomposition followed by NMR analysis. Diagnostic ¹H-NMR (600MHz, D_2O): δ 8.26 (d), 8.09 (m), 7.90 (d), 7.75 (m), 7.58-7.62 (m), 7.44-7.52 (m), 7.31 (m), 7.23 (m), 6.65 (s), 6.30-6.32 (m), 6.06-6.11 (m), 5.89 (m), 5.84 (m).
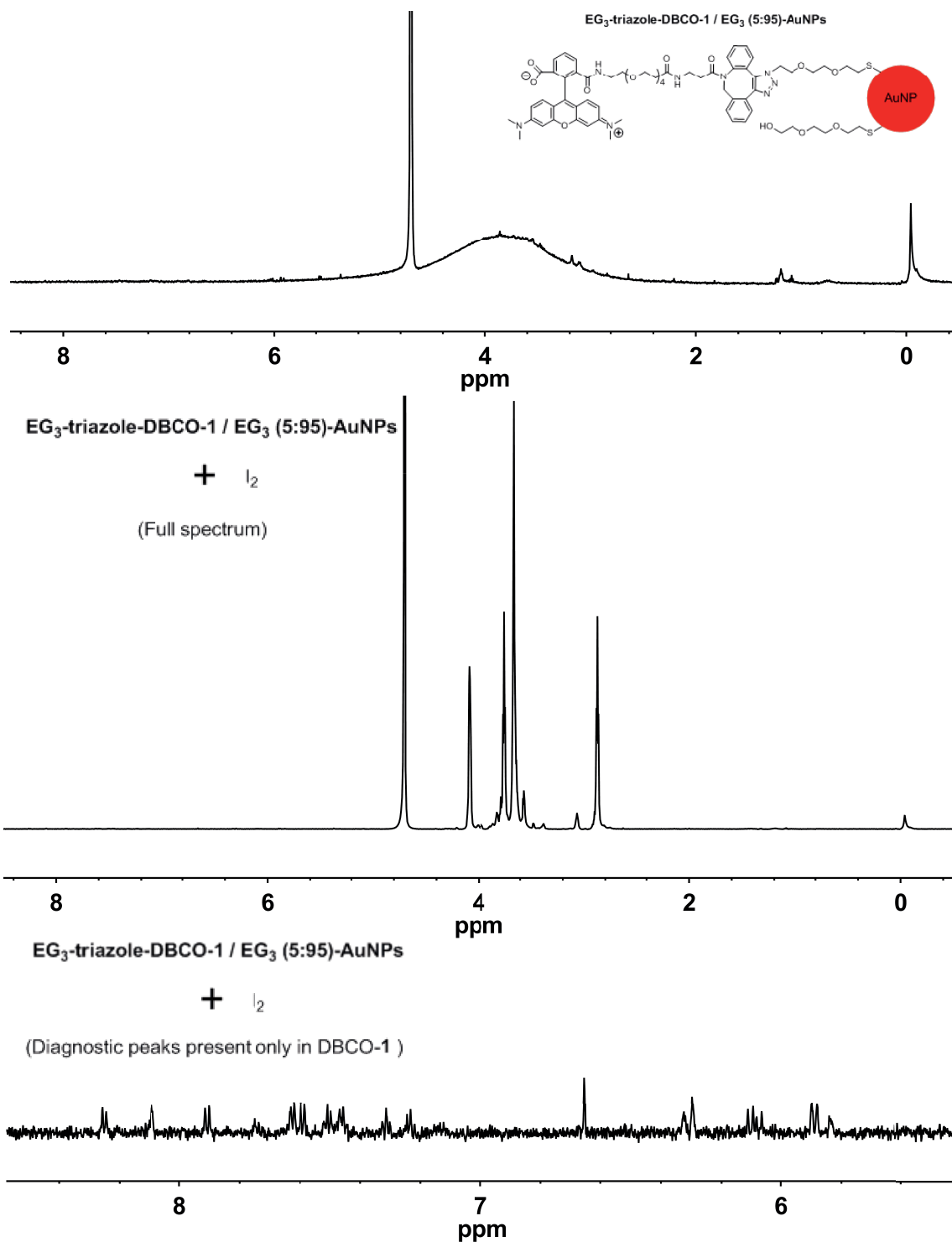
Figure S6. NMR characterization of **EG₃-triazole-DBCO-1 / EG₃ (5:95)-AuNPs** before and after I₂ decomposition. Diagnostic peaks showing successful coupling shown enlarged.

EG$_3$-triazole-DBCO-2 / EG$_3$ (5:95)-AuNPs. Lyophilized **EG$_3$-azide / EG$_3$ (5:95)-AuNPs** (15.04 mg, 4.0 x 10^{-7} mol EG$_3$-azide) were dissolved in H$_2$O (1 mL) in a scintillation vial. DBCO-PEG$_4$-OH (1.53 mg, 3.0 x 10^{-6} mol) (dissolved in 1 mL t-BuOH) was added to the vial, capped, and the mixture was stirred at room temperature for 24 hours. The reaction mixture was then purified and lyophilized to isolate **EG$_3$-triazole-DBCO-2 / EG$_3$ (5:95)-AuNPs** as a black powder. Diagnostic ^{1}H-NMR (600MHz, D$_2$O): δ 8.34 (d), 8.18-8.23 (m), 7.99 (d), 7.81-7.92 (m), 7.67-7.72 (m), 7.60 (m), 7.55 (m), 7.40 (t), 7.32 (t), 7.22 (m), 6.74 (s).
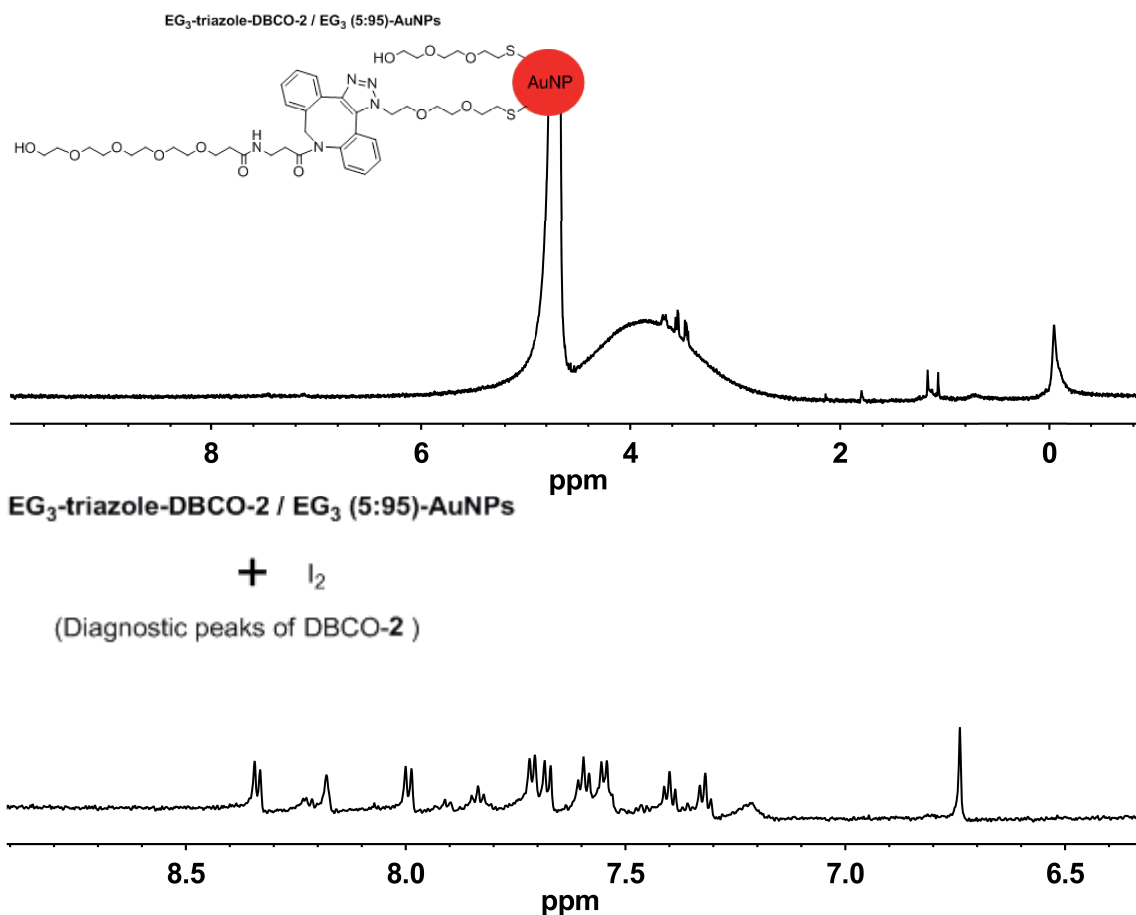
Figure S7. NMR characterization of **EG$_3$-triazole-DBCO-2 / EG$_3$ (5:95)-AuNPs** before and after I$_2$ decomposition. Diagnostic peaks showing successful coupling shown enlarged.

141

EG$_3$-triazole-DBCO-3 / EG$_3$ (5:95)-AuNPs. Lyophilized **EG$_3$-azide / EG$_3$ (5:95)-AuNPs** (16.70 mg, 4.4 x 10^{-7} mol EG$_3$-azide) were dissolved in H$_2$O (1 mL) in a scintillation vial. DBCO-PEG$_4$-NHS-ester (1.16 mg, 2.9 x 10^{-6} mol) (dissolved in 1 mL DMSO) was added to the vial, capped, and the mixture was stirred at room temperature for 24 hours. The reaction mixture was then purified and lyophilized to isolate **EG$_3$-triazole-DBCO-3 / EG$_3$ (5:95)-AuNPs** as a black powder. Diagnostic ^{1}H-NMR (600MHz, D$_2$O/DMSO-d$_6$ (80:20)): δ 2.80-2.83 (m), 2.77 (m), 2.35 (m).
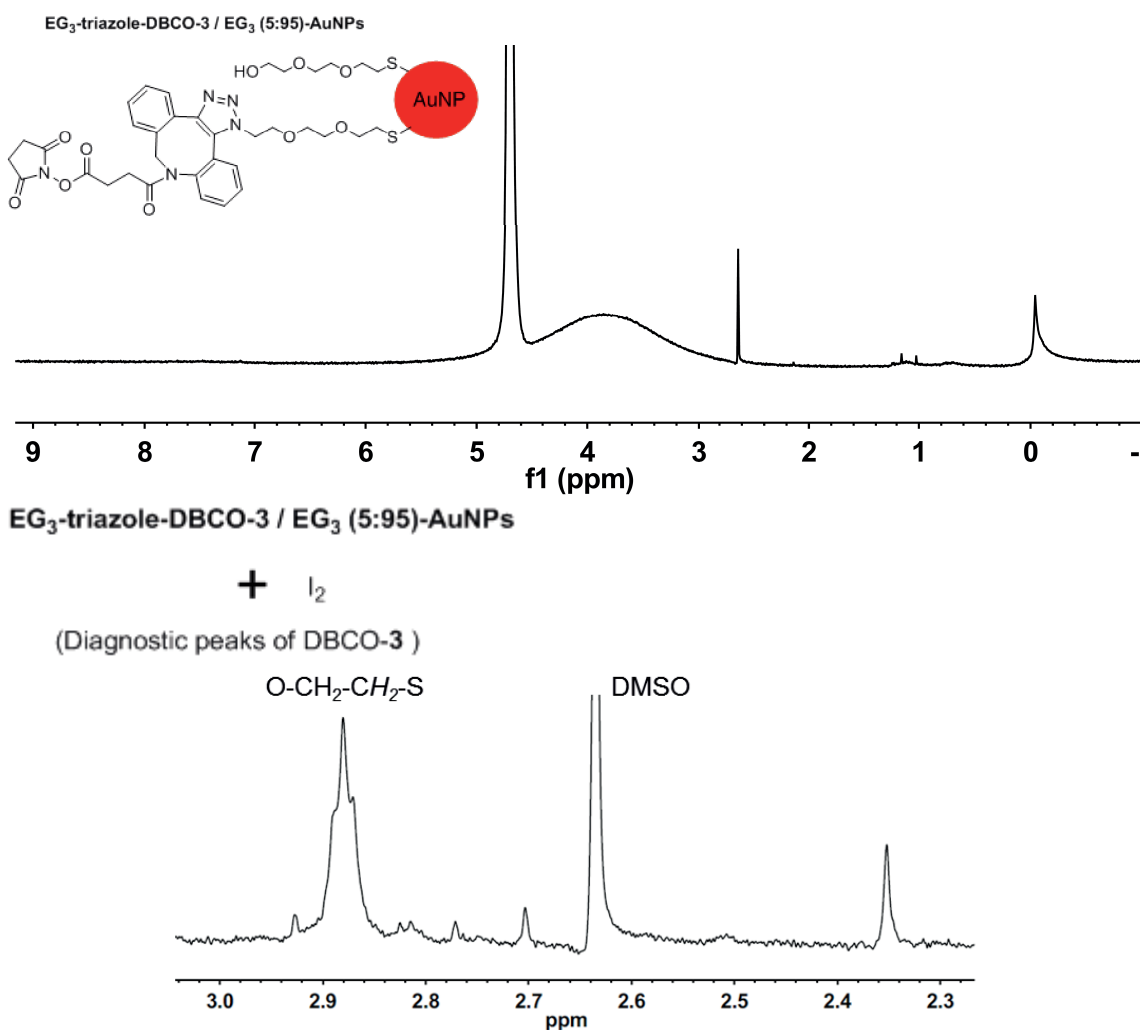
Figure S8. NMR characterization of **EG$_3$-triazole-DBCO-3 / EG$_3$ (5:95)-AuNPs** before and after I$_2$ decomposition. Diagnostic peaks showing successful coupling shown enlarged.

142

Copper-catalyzed 1,3-dipolar cycloadditions involving EG$_3$-azide / EG$_3$-(5:95)-AuNPs and terminal alkynes (4-7)

Figure S9. Copper catalyzed 1,3-dipolar cycloadditions involving **EG$_3$-azide / EG$_3$ (5:95)-AuNPs** and various terminal alkynes (**4-7**)

EG$_3$-triazole-4 / EG$_3$ (5:95)-AuNPs. Lyophilized **EG$_3$-azide / EG$_3$ (5:95)-AuNPs** (10.0 mg, 2.6 x 10^{-7} mol EG$_3$-azide) were dissolved in H$_2$O (489 µL) in a scintillation vial. Sodium ascorbate (38 µL, 0.01 M in H$_2$O, 3.8 x 10^{-7} mol) was added to the vial, followed by tert-butyl alcohol as a co-solvent (985 µL), 1-ethynyl-1-cyclohexanol (15 µL, 0.1 M in tert-butyl alcohol, 1.5 x 10^{-6} mol), and CuBr (474 µL, satd., aq. 3.8 x 10^{-8} mol) The resulting solution was capped and stirred at room temperature for 48 hours. The reaction mixture was then purified and lyophilized to isolate **EG$_3$-triazole-4 / EG$_3$ (5:95)-AuNPs** as a black powder. For ^{1}H-NMR analysis, AuNPs were dissolved in D$_2$O/DMSO-d$_6$ (80:20, 500 µL total) to confirm successful purification and decomposed with I$_2$. Diagnostic ^{1}H-NMR (600MHz, D$_2$O/DMSO-d$_6$ (80:20)): δ 1.79-1.84 (m), 1.38-1.66 (m).

Figure S10. NMR characterization of **EG₃-triazole-4 / EG₃ (5:95)-AuNPs** following I₂ decomposition. Diagnostic peaks showing successful coupling shown enlarged for clarity.

EG₃-triazole-5 / EG₃ (5:95)-AuNPs. Lyophilized **EG₃-azide / EG₃ (5:95)-AuNPs**

(14.6 mg, 3.9 x 10⁻⁷ mol EG₃-azide) were dissolved in H₂O (489 µL) in a scintillation vial.

Sodium ascorbate (37.5 µL, 0.01 M in H₂O, 3.75 x 10⁻⁷ mol) was added to the vial,

followed by tert-butyl alcohol as a co-solvent (985 µL), phenylacetylene (15 µL, 0.1 M in

tert-butyl alcohol, 1.5 x 10⁻⁶ mol), and CuBr (474 µL, satd., aq. 3.8 x 10⁻⁸ mol). The

resulting solution was capped and stirred at room temperature for 48 hours. The reaction

mixture was then purified and lyophilized to isolate **EG₃-triazole-5 / EG₃ (5:95)-**

AuNPs as a black powder. For ¹H-NMR analysis, AuNPs were dissolved in

D₂O/DMSO-d₆ (80:20, 500 µL total) to confirm successful purification and decomposed

with I₂, then extracted into CD₂Cl₂ (500 µL) and the organic phase was washed with

brine (500 µL). Diagnostic ¹H-NMR (600MHz, CD₂Cl₂): δ 7.97-8.05 (m), 7.30-7.72 (m),

7.20-7.29 (m).
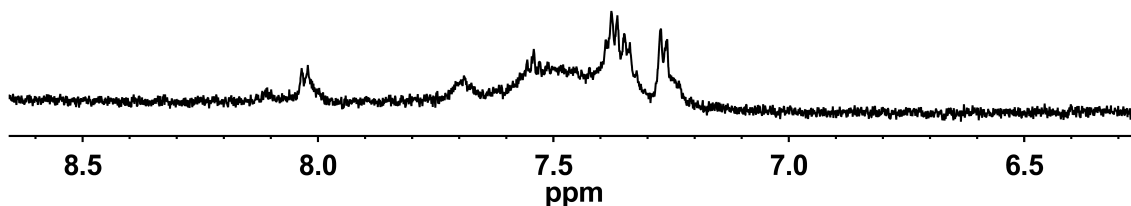
Figure S11. NMR characterization of **EG₃-triazole-5 / EG₃ (5:95)-AuNPs** following I₂ decomposition. Diagnostic peaks showing successful coupling shown enlarged.
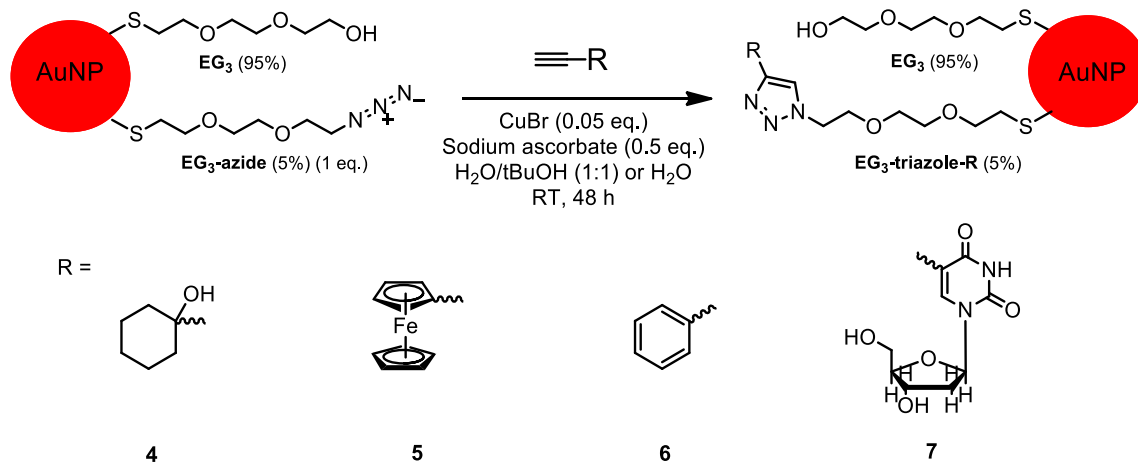

EG₃-triazole-6 / EG₃ (5:95)-AuNPs. Lyophilized **EG₃-azide / EG₃ (5:95)-AuNPs**

(14.5 mg, 3.8 x 10⁻⁷ mol EG₃-azide) were dissolved in H₂O (489 µL) in a scintillation vial.

Sodium ascorbate (37.5 µL, 0.01 M in H₂O, 3.8 x 10⁻⁷ mol) was added to the vial,

followed by tert-butyl alcohol (985 µL), ethynylferrocene (15 µL, 0.1 M in tert-butyl

alcohol, 1.5 x 10⁻⁶ mol), and CuBr (474 µL, satd., aq. 3.8 x 10⁻⁸ mol) The resulting

solution was capped and stirred at room temperature for 48 hours. The reaction mixture

was then purified and lyophilized to isolate **EG₃-triazole-6 / EG₃ (5:95)-AuNPs** as a

black powder. For ¹H-NMR analysis, AuNPs were dissolved in D₂O/DMSO-d₆ (80:20,

500 µL total) to confirm successful purification, decomposed with I₂, then extracted into

CDCl₃ (500 µL) and the organic phase was washed with brine (500 µL). Diagnostic ¹H-

NMR (600MHz, CDCl₃): δ 4.13-4.15 (ferrocene, m).
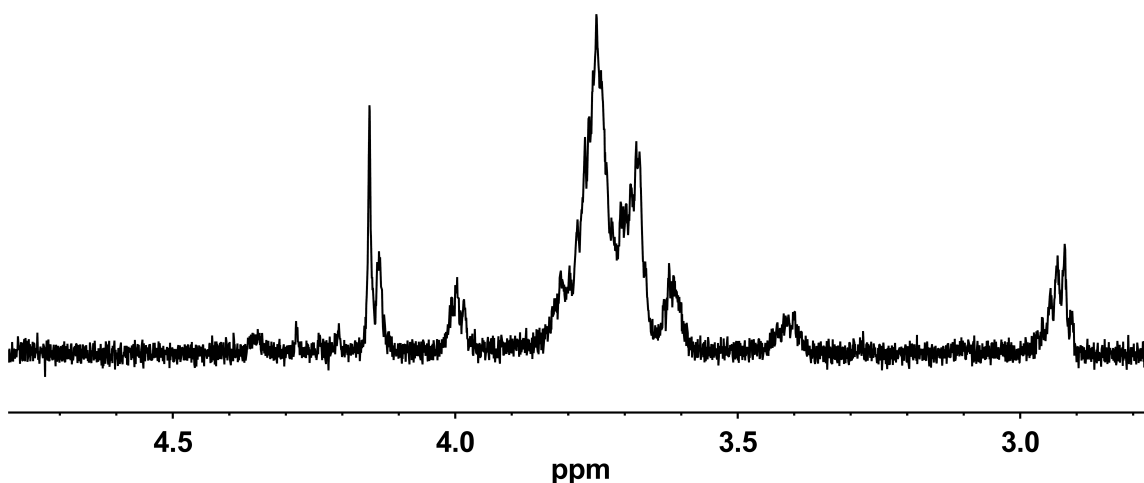
Figure S12. NMR characterization of **EG₃-triazole-6 / EG₃ (5:95)-AuNPs** following I₂ decomposition. Diagnostic peaks showing successful coupling shown enlarged for clarity.
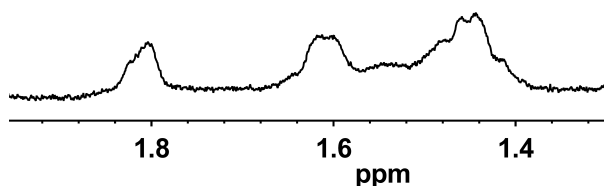
EG₃-triazole-7 / EG₃ (5:95)-AuNPs. Lyophilized **EG₃-azide / EG₃ (5:95)-AuNPs** (13.1 mg, 3.5×10^{-7} mol EG₃-azide) were dissolved in H_2O (489 µL) in a scintillation vial. Sodium ascorbate (37.5 µL, 0.1 M in H_2O, 3.8×10^{-7} mol) was added to the vial, followed by tert-butyl alcohol (985 µL), 5-ethynyl-2'-deoxyuridine[5] (15 µL, 0.1 M in tert-butyl alcohol, 1.5×10^{-6} mol), and CuBr (474 µL, satd., aq. 3.8×10^{-8} mol) The resulting solution was capped and stirred at room temperature for 48 hours. The reaction mixture was then purified and lyophilized to isolate **EG₃-triazole-7 / EG₃ (5:95)-AuNPs** as a black powder. For ¹H-NMR analysis, AuNPs were dissolved in D_2O/DMSO-d_6 (91:9, 550 µL total) to confirm successful purification and decomposed with I_2. Diagnostic ¹H-NMR (600MHz, D_2O/DMSO-d_6 (91:9)): δ 8.76 (s), 8.07-8.13 (m), 6.12-6.34 (m), 5.82-5.88 (m).
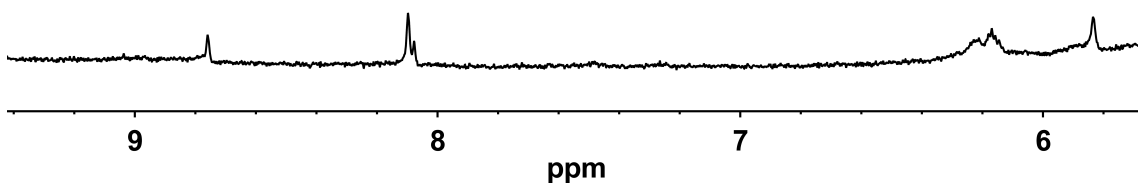
Figure S13. NMR characterization of **EG₃-triazole-7 / EG₃ (5:95)-AuNPs** following I_2 decomposition. Diagnostic peaks showing successful coupling shown enlarged for clarity.

APPENDIX C

SUPPORTING INFORMATION FOR CHAPTER V:

THE CONTROLLED REMOVAL OF THIOL LIGANDS FROM SURFACE-

CONFINED, MONOLAYER PROTECTED GOLD NANOPARTICLES
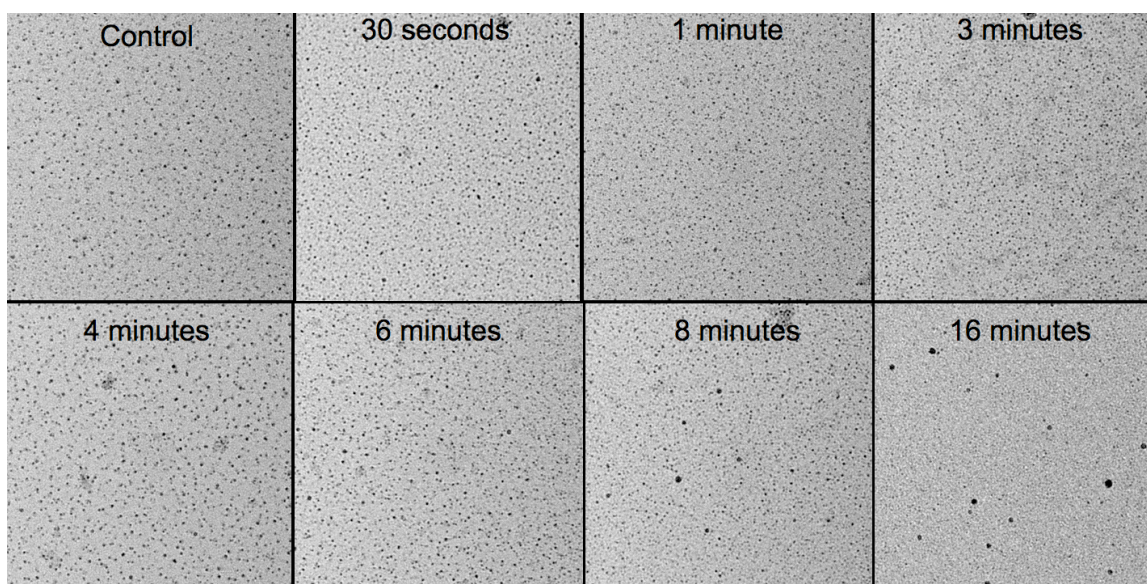
Figure S1. TEM micrographs of 1.5 nm 2-MEPA AuNP nanoparticle assemblies treated with dilute ozone, each representative of an individual sample removed from the ozone stream at incremental time points. The nanoparticles assemblies are visually similar through out treatment through 8 minutes. At 16 minutes larger aggregates appeared indicating particle growth and disruption to the nanoparticle assembly.
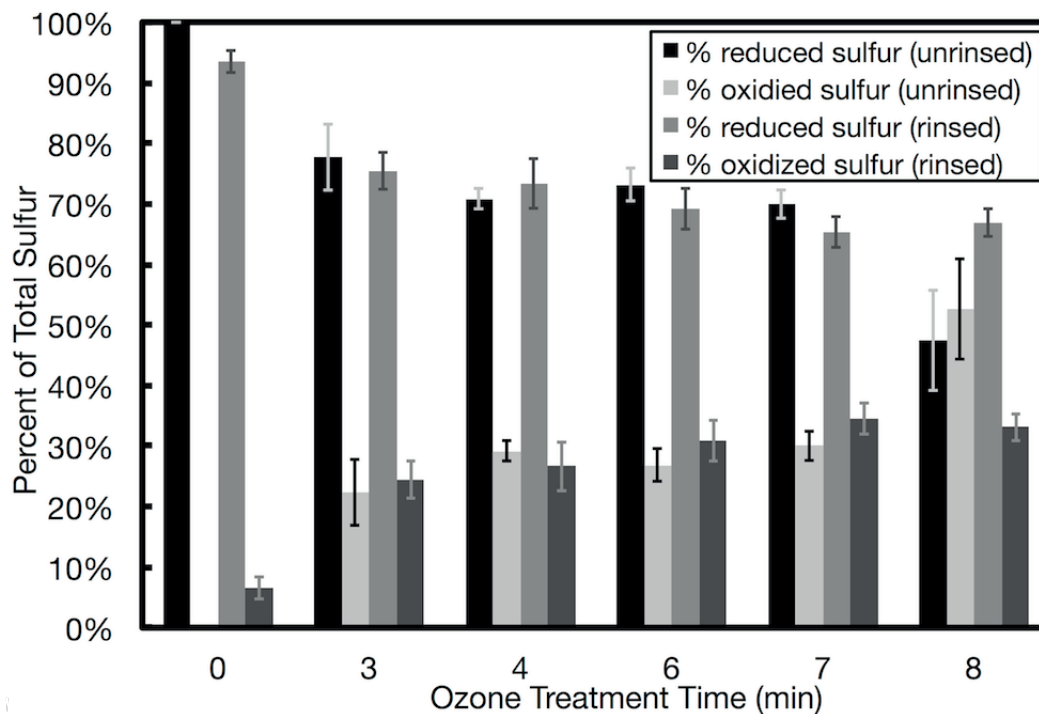
Figure S2. Bar graph plotting XPS S2p3 peak area ratios between reduced and oxidized sulfur on samples treated with ozone over 8 minutes. At each time point two were analyzed as treated (unrinsed) and the other two following an 11 minute water rinse (rinsed). Peaks were fit to an S2p trace and each percentage was calculated from the sum of oxidized (168 eV) and reduced (162 eV)sulfur on that sample.
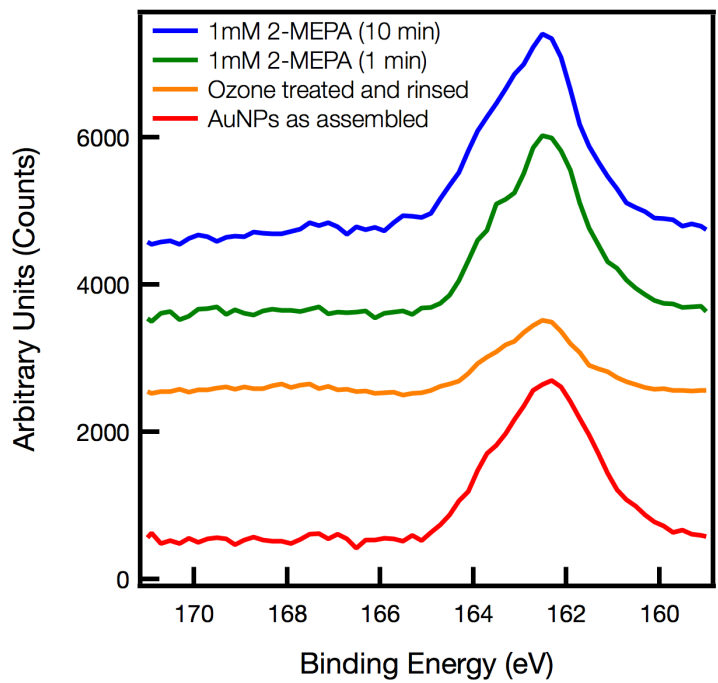
Figure S3. Stacked XPS S2p traces of assembled AuNPs (red), following ligand removal with ozone (orange) and after soaking in 1 mM 2-MEPA to restore the ligand shell (green and blue). The ligand shell shows restoration of thiolate linkages after 1 minute (green) and little change after 10 minutes (blue).
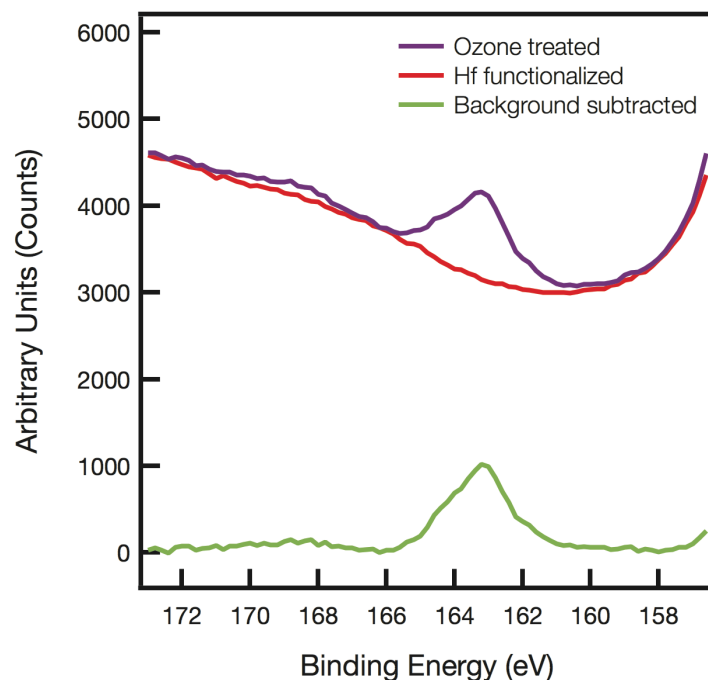
Figure S4. 3 traces shown from planar analysis platform of to illustrate the background subtraction process. The blue trace represents the average trace from three points on a sample treated with ozone for 8 minutes. The red trace represents the average trace from three points on the planar analysis platform substrate prior to nanoparticle assembly. The black is a result of subtracting the red trace from the black trace to remove interference from the silicon shake-up feature.

REFERENCES CITED

Chapter I

(1)   Huang, C.; Notten, A.; Rasters, N. *J. Technol. Transf.* **2011**, 36, 145-172.

(2)   Lee, D-E.; Koo, H.; Sun, I-C.; Ryu, J. H.; Kim, K.; Kwon, I. C. *Chem. Soc. Rev.* **2012**, 41, 2656.

(3)   Rana, S.; Bajaj, A.; Mout, R.; Rotello, V. M. *Adv. Drug Deliver. Rev.,* **2012**, 64, 200.

(4)   Saha, K.; Agasti, S. S.; Kim, C.; Li, X.; Rotello, V. M. *Chem. Rev.*, **2012**, 112, 2739.

(5)   Homberger, M.; Simon, U. *Philos. Trans. A: Math. Phys. Eng. Sci.* **2010**, 368, 1405-1453.

(6)   Kolb, H. C.; Finn, M. G.; Sharpless, K. B. *Angew. Chem. Int. Ed.* **2001**, 40, 2004-2012.

(7)   Faraday, M. *Phil. Trans. R. Soc. Lond.* **1857**, 147, 145-181

(8)   Turkevich, J.; Stevenson, P. C.; Hillier, J. *Discuss. Faraday Soc.* **1951**, 11, 55-75.

(9)   Brust, M.; Walker, M.; Bethell, D.; Schiffrin, D. J.; Whyman, R., *J. Chem. Soc., Chem. Commun.*, **1994**, 7, 801-802.

(10)   Haruata, M., *Chem. Rec.*, **2003**, 3, 75-87.

(11)   Mitsudome, T.; Kaneda, K., *Green Chem.*, **2013**, 15, 2636-2654.

(12)   Turner, M.; Golovko, V.; Vaughan, O.; Abdulkin, P.; Berenguer-Murcia, A.; Tikhov, M.; Johnson, B. F. G.; Lambert, R. M. *Nature*, **2008**, *454*, 981−983.

(13)   Ghosh, P.; Han, G.; De, M.; Kim, C. K.; Rotello, V. M., *Adv. Drug Deliver. Rev.*, **2008**, 60, 1307-1315.

(14)   Sperling, R. A.; Gil, P. R.; Zhang, F.; Zanella, M.; Parak, W. J. *Chem. Soc. Rev.* **2008**, 37, 1896-1908.

(15)   Connor, E. E.; Mwamuka, J.; Gole, A.; Murphy, C. J.; Wyatt, M. D. *Small* **2005**, 3, 325-327.

(16)   Pan, Y.; Neuss, S.; Leifert, A.; Fischler, M.; Wen, F.; Simon, U.; Schmid, G.; Brandau, W.; Jahnen-Dechent, W., *Small*, **2007**, 3, 1941-1949.

(17)   Truong, L.; Tilton, S. C.; Zaikova, T.; Richman, E.; Waters, K. M.; Hutchison, J. E.; Tanguay, R. L. *Nanotoxicology* **2013**, 7, 192-201

(18)   Kim, K. T.; Zaikova, T.; Hutchison, J. E.; Tanguay, R. L. *Toxicol. Sci.* **2013**, 133, 275-288.

(19)   Cai, W.; Gao, T.; Hong, H.; Sun, J. *Nanotechnol. Sci. Appl.* **2008**, 1, 17-32.

(20)   Jain, S.; Hirst, D. G.; O'Sullivan, J. M. *Br. J. Radiol.* **2012**, 85, 101-113.

(21)   Llevota, A.; Astruc, D. *Chem. Soc. Rev.* **2012**, 41, 242–257.

(22)   Dykman, L. A.; Khlebtsov, N. G. *Chem. Rev.* **2014**, 114, 1258-1288.

(23)   Bramini, M.; Ye, D.; Hallerbach, A.; Raghnail, M. N.; Salvati, A.; Aberg, C.; Dawson, K. A. *ACS Nano* **2014**, [Online early access].

(24)   Chompoosor, A.; Han, G.; Rotello, V. M. *Bioconjugate Chem.* **2008**, 19, 1342-1345.

(25)   Prencipe, G.; Tabakman, S. M.; Welsher, K.; Liu, Z.; Goodwin, A. P.; Zhang, L.; Henry, J.; Dai, H., *J. Am. Chem. Soc.*, **2009**, 131, 4783-4787.

(26)   Otsuka, H.; Nagasaki, Y.; Kataoka, K., *Adv. Drug Deliv. Rev.*, **2003**, 55, 403-419.

(27)   Lee, J.; Chatterjee, D. K.; Lee, M. H.; Krishnan, S. *Cancer Lett.* **2014**, 347, 46-53.

(28)   Huang, X.; Jain, P. K.; El-Sayed, I. H.; El-Sayed, M. A., *Nanomedicine-UK*, **2007**, 2, 681-693.

(29)   Lipka, J.; Semmler-Behnke, M.; Sperling, R. A.; Wenk, A.; Takenaka, S.; Schleh, C.; Kissel, T.; Parak, W. J.; Kreyling, W. G., *Biomaterials*, **2010**, 31, 6574-6581.

(30)   Chithrani, B. D.; Ghazani, A. A.; Chan, C. W. *Nano Letts.* **2006**, 6, 662-668

(31)   Oh, E.; Delehanty, J. B.; Sapsford, K. E.; Susumu, K.; Goswami, R.; Blanco-Canosa, J. B.; Dawson, P. E.; Granek, J.; Shoff, M.; Zhang, Q.; Goering, P. L.; Huston, A.; Medintz, I. L. *ACS Nano* **2011**, 5, 6434- 6448.

(32)   Kang, B.; Mackey, M. A.; El-Sayed, M. A. *J. Am. Chem. Soc.* **2010**, 132, 1517-1519.

(33)   Nativo, P.; Prior, I. A.; Brust, M. *ACS Nano* **2008**, 2, 1639-1644.

(34)   Pelaz, B.; Jaber, S.; de Aberasturi, D. J.; Wulf, V.; Aida, T.; de la Fuente, J. E.;
         Feldmann, J.; Gaub, H.E.; Josephson, L.; Kagan, C. R.; Kotov, N. A.; Liz-
         Marzán, L. M.; Mattoussi, H.; Mulvaney, P.; Murray, C. B.; Rogach, A. L.;
         Weiss, P. S.; Wilner, I.; Parak, W. J., *ACS Nano*, **2012**, 6, 8468-8483.

(35)   Brown, S. C.; Boyko, V.; Meyers, G.; Voetz, M.; Wohleben, W. *Environ. Health
         Perspect.* **2013**, 121, 1282-1291.

(36)   Liden, G. *Ann. Occup. Hyg.* **2011**, 55, 1-5.

(37)   Maynard, A. D. *Nature*, **2011**, 475, 31.

(38)   Auffan, M.; Rose, J.; Bottero, J. Y.; Lowry, G. V.; Jolivet, J. P.; Wiesner, M. R.
         Nat. Nanotechnol. **2009**, 4, 634-641.

(39)   Cheng, Z.; Al Zaki, A.; Hui, J. Z.; Muzykantov, V. R.; Tsourkas, A. *Science*
         2012, 338, 903-910.

(40)   Richman, E. K.; Hutchison, J. E. *ACS Nano* **2009**, 3, 2441-2446.

(41)   Ozin, G. Nanochemistry Reproducibility. September 19, 2013, *Materials Views*
         [Online] http://www.materialsviews.com/nanochemistry-reproducibility/
         (accessed April 28, 2014).

(42)   Woehrle, G. H.; Hutchison, J. E. *Inorg. Chem.* **2005**, 44, 6149-6158.

(43)   Jadzinsky, P. D.; Calero, G.; Ackerson, C.J.; Bushnell, D.A.; Kornberg, R.D.
         Science **2007**, 318, 430-433.

(44)   Baumgardner, W. J.; Quan, Z.; Fang, J.; Hanrath, T. *Nanoscale* **2012**, 4, 3625-
         3628.

(45)   Geyer, K.; Codee, J. D. C.; Seeberger, P. H. *Chem. Eur. J.*, **2006**, 33, 8434-
         8442.

(46)   Hessel, V.; Renken, A.; Schouten, J. C.; Yoshida, J-I. Micro Process
         Engineering: A Comprehensive Handbook; Wiley-VCH: Weinheim, 2009;
         Vol. 1.

(47)   Fang, J. Z.; Lee, D. J. *Chem. Eng. Sci.* **2001**, 56, 3797-3802.

(48)   Nguyen, N-T. Micomixers: Fundamentals, Design and Fabrication, 2nd ed.;
         Elsevier: Boston, 2012.

(49)   Hessel, V.; Löwe, H.; Schönfelf, F. *Chem. Eng. Sci.* **2005**, 8, 2479-2501.

(50)   Haiss, W; Thanh, N. T. K.; Aveyard, J.; Fernig, D. G., *Anal. Chem.*, **2007**, 79,
         4215-4221.

(51)   Liu, X.; Atwater, M.; Wang, J.; Huo, Q., *Colloids Surf.*, **2007**, 58, 3-7.

(52)   Williams, D. B.; Carter, B. C. Transmission Electron Microscopy: A Textbook for Materials Science, 2nd ed.; Springer: New York, 2009.

(53)   Woehrle, G. H.; Hutchison, J. E.; Ozkar, S.; Finke, R. G. *Turk. J. Chem.* **2006**, 30, 1-13.

(54)   Pyrz, W. D.; Buttrey, D. J. *Langmuir*, **2008**, 24, 11350-11360.

(55)   Woehl, T. J.; Jungjohann, K. L.; Evans, J. E.; Arslan, I.; Ristenpart, W. D.; Browning, N. D. *Ultramicroscopy*, **2013**, 127, 53-63.

(56)   Kawamoto, N.; Tang, D.; Wei, X.; Wang, X.; Mitome, M.; Bando, Y.; Golberg, D. *Microscopy*, **2013**, 62, 157-176.

(57)   Pennycook, S. J.; Varela, M.; Lupini, A. R.; Oxley, M. P.; Chisholm, M. F. *J. Electron Microsc.* **2009**, 58, 87-97.

(58)   Herzing, A. A.; Kiely, C. J.; Carley, A. F.; Landon, P.; Hutchings, G. *Science* **2008**, 321, 1331-1335.

(59)   Williams, D. B.; Carter, B. C. Transmission Electron Microscopy: Spectroscopy; Plenum Press: New York, 1996; Vol. 4.

(60)   Glatter, O; Kratky, O. *Small-angle X-ray Scattering;* Academic Press: London, 1982.

(61)   Polte, J.; Erler, R.; Thunemann, A. F.; Sokolov, S. Ahner, T. T.; Rademann, K.; Emmerling, F.; Kraehnert, R. *ACS Nano*, **2010**, 4, 1076-1082.

(62)   Cho, H. S.; Schotte, F.; Dashdorj, N.; Kyndt, J.; Anfinrud, P. A. *J. Phys. Chem. B* **2013**, 117, 15825-15832.

(63)   Saldin, D. K.; Poon, H. C.; Bogan, M. J.; Marchesini, S.; Shapiro, D.A.; Kirian, R. A.; Weierstall, U.; Spence, J. C. H. *Phys. Rev. Lett.* **2011**, 106, 115501.

(64)   Ilavsky, J.; Jemian, P. R. *J. Appl. Cryst.* **2009**, 42, 347-353.

(65)   Pauw, B. R. *J. Phys.: Condens. Matter* **2013**, 25, 383201-383225.

(66)   Daughdrill, D. W.; Kashtanov, S.; Stancik, A.; Hill, S. E.; Helms, G.; Muschol, M.; Receveur-Bréchot, V.; Ytreberg, F. M. *Mol. Biosyst.* **2012**, 8, 308-319.

(67)   Bernado, P.; Svergun, D. I. *Mol. Biosyst.* **2012**, 8, 151-167.

(68)   Tsutakawa, S. E.; Hura, G. L.; Frankel, K. A.; Cooper, P. K.; Tainer, J. A. *J. Struc. Biol.* **2007**, 158, 214-223.

(69)   Choi, K. H.; Morais *Methods Mol. Bio.* **2014**, 1138, 241-251.

(70)   Pelikan, M.; Hura, G. L.; Hammel, M. *Gen. Physiol. Biophys.* **2009**, 28, 174-189.

(71)   McKenzie, L. C.; Haben, P. M.; Kevan, S. D.; Hutchison, J. E. *J. Phys. Chem. C* **2010**, 114, 22055-22063.

(72)   Salorinne, K.; Lahtinen, T.; Koivisto, J.; Kalenius, E.; Nissinen, M.; Pettersson, M.; Häkkinen, H. *Anal. Chem.* **2013**, 85, 3489-3492.

(73)   Canzi, G.; Mrse, A. A.; Kubiak, C. P. *J. Phys. Chem. C* **2011**, 115, 7972-7978.

(74)   Kohlmann, O.; Steinmetz, W. E.; Mao, X.; Wuelfing, W. P.; Templeton, A. C.; Murray, R. W.; Johnson Jr., C. S. **2001**, 105, 8801-8809.

(75)   Canzi, G.; Mrse, A. A.; Kubiak, C. P., *J. Phys. Chem. C*, **2011**, 115, 7972-7978.

(76)   Van der Heide, P. X-ray Photoelectron Spectroscopy : an Introduction to Principles and Practices; Wiley: Hoboken, NJ, 2012.

(77)   Jespersen, M. L.; Inman, C. E.; Kearns, G. J.; Foster, E. W.; Hutchison, J. E. *J. Am. Chem. Soc.*, **2007**, *129*, 2803–2807.

(78)   Zorn, G.; Dave, S. R.; Gao, X.; Castner, D. G. *Anal. Chem.*, **2011**, *83*, 866–873.

(79)   Techane, S.; Baer, D. R.; Castner, D. G. *Anal. Chem.,* **2011**, 83, 6704–6712.

(80)   Bourg, M.C.; Badia, A.; Lennox, R. B. *J. Phys. Chem. B,* **2000**, *104*, 6562–6567.

(81)   Smith, B. L.; Hutchison, J. E., *J. Phys. Chem. C*, **2013**, 117, 25127-25137.

(82)   Castner, D. G.; Hinds, K.; Grainger, D. W. *Langmuir*, **1996**, *12*, 5083–5086.

(83)   Woehrle, G. H.; Brown, L. O.; Hutchison, J. E. *J. Am. Chem. Soc.* **2005**, 127, 2172-2183.

(84)   Brennen, J. L.; Hatzakis, N. S.; Tshikhudo, T. R.; Dirvianskyte, N.; Razumas, V.; Patkar, S.; Vind, J.; Svendsen, A.; Nolte, R. J. M.; Rowan, A. E.; Brust, M. *Bioconj. Chem.* **2006**, 17, 1373-1375.

(85)   Mann, S. *Nature Mater.* **2009**, 8, 781-792.

(86)   Lu, Y.; Liu, J. *Acc. Chem. Res.*, **2007**, 40, 315-323.

(87)   Zhang, S.; Leem, G.; Lee, T. R. *Langmuir* **2009**, 25, 13855-13860.

(88)   Lukkari, J.; Meretoja, M.; Kartio, I.; Laajalehto, K.; Rajamaki, M.; Lindstrom, M.; Kankare, J. *Langmuir* **1999**, 15, 3529-3537.

(89)   Lohse, S. E.; Dahl, J. A.; Hutchison, J. E. *Langmuir* **2010**, 26, 7504-7511.

(90)   Shon, Y.; Gross, S. M.; Dawson, B.; Porter, M.; Murray, R. W. *Langmuir* **2000**, 16, 6555-6561.

(91)   IUPAC. Compendium of Chemical Terminology, 2nd ed. (the "Gold Book"). Compiled by A. D. McNaught and A. Wilkinson. Blackwell Scientific Publications, Oxford (1997). XML on-line corrected version: http://goldbook.iupac.org (2006-) created by M. Nic, J. Jirat, B. Kosata; updates compiled by A. Jenkins.

(92)   Reeves, J. T.; Camara, K.; Han, Z. S.; Xu, Y.; Lee, H.; Busacca, C. A.; Senanayake, C. H., *Org. Lett.*, **2014**, 16, 1196-1199.

(93)   Lecher, H. Z.; Hardy, E. M. *J. Org. Chem.* **1955**, 20, 475-487.

(94)   Distler, H. *Ang. Chem. Int. Ed.* **1967**, 6, 544-553.

(95)   Kice, J. L. *J. Org. Chem.* **1963**, 28, 957-961.

(96)   Sweeney, S. F.; Woehrle, G. H.; Hutchison, J. E. *J. Am. Chem. Soc.* **2006**, 128, 3190-3197.

(97)   Zhao, P.; Grillaud, M.; Salmon, L.; Ruiz, J.; Astruc, D. *Adv. Synth. Catal.*, **2012**, 354, 1001.

(98)   Boisselier, E.; Salmon, L.; Ruiz, J.; Astruc, D. *Chem. Commun.*, **2008**, 44, 5788.

(99)   Li, N.; Zhao, P.; Salmon, L.; Ruiz, J.; Zabawa, M.; Hosmane; N. S.; Astruc, D. *Inorg. Chem.*, **2013**, 52, 11146.

(100)   Baranov, D.; Kadnikova, E. N. *J. Mater. Chem.*, **2011**, 21, 6152.

(101)   Gobbo, P.; Novoa, S.; Biesinger, M. C.; Workentin, M. S. *Chem. Commun.*, **2013**, 49, 3982.

(102)   Flemming, D.; Thode, C.; Williams, M. *Chem. Mater.*, **2006**, 18, 2327.

(103)   Thode, C.; Williams, M., *J. Colloid Interface Sci.*, **2008**, 320, 346.

(104)   Hajati, S.; Zaporojtchenko, V.; Faupel, F.; Tougaard, S. *Surf. Sci.*, **2007**, 601, 3261-3267.

Chapter II

(1)   R. Silverstein, F. Webster, D. Kiemle, *Spectrometric Identification of Organic Compounds*, John Wiley & Sons, Inc, State University of New York, **2005**.

(2)   Z. L. Mensinger, J. T. Gatlin, S. T. Meyers, L. N. Zakharov, D. A. Keszler, D. W. Johnson, *Angew. Chem. Int. Ed.* **2008**, *47*, 9484–9486.

(3)   J. Heo, J. Kim, S. Choi, K. S. Park, C. D. Kim, Y. K. Hwang, I. J. Chung, S. T. Meyers, J. T. Anderson, B. C. Clark, et al., *SID 10 Digest* **2010**, *41*, 241–244.

(4)   F. von der Kammer, P. L. Ferguson, P. A. Holden, A. Masion, K. R. Rogers, S. J. Klaine, A. A. Koelmans, N. Horne, J. M. Unrine, *Environ. Toxicol. Chem.* **2012**, *31*, 32–49.

(5)   J. Polte, R. Erler, A. F. Thünemann, S. Sokolov, T. T. Ahner, K. Rademann, F. Emmerling, R. Kraehnert, *ACS Nano* **2010**, *4*, 1076–1082.

(6)   E. Richman, J. Hutchison, *ACS Nano* **2009**, *3*, 2441–2446.

(7)   L. C. McKenzie, P. M. Haben, S. D. Kevan, J. E. Hutchison, *J. Phys. Chem. C* **2010**, *114*, 22055–22063.

(8)   O. Glatter, O. Kratky, *Small Angle X-ray Scattering*, Academic Press, London, **1982**.

(9)   J. S. Pedersen, *Adv. Colloid Interface Sci.* **1997**, *70*, 171–210.

(10)   G. Schwedt, *The Essential Guide to Analytical Chemistry*, John Wiley & Sons, Inc, Chichester, **1997**.

(11)   T. D. W. Claridge, *High-Resolution NMR Techniques in Organic Chemistry*, Elsevier, Oxford, **2009**.

(12)   C. S. Johnson Jr., *Prog. Nucl. Magn. Reson. Spectrosc.* **1999**, *34*, 203–256.

(13)   D.-L. Long, R. Tsunashima, L. Cronin, *Angew. Chem. Int. Ed.* **2010**, *49*, 1736–1758.

(14)   C. A. Ohlin, *Chem. Asian J.* **2012**, *7*, 262–270.

(15)   P. J. Wyatt, *Anal. Chim. Acta* **1993**, *272*, 1–40.

(16)   R. Tantra, P. Schulze, P. Quincey, *Particulology* **2010**, *8*, 279–285.

(17)   X. Liu, M. Atwater, J. Wang, Q. Huo, *Colloid. Surface B* **2007**, *58*, 3–7.

(18)   A. F. Oliveri, M. E. Carnes, M. M. Baseman, E. K. Richman, J. E. Hutchison, D. W. Johnson, *Angew. Chem. Int. Ed.* **2012**, *51*, 10992–10996.

(19)   M. Jackson, L. Wills, I. Chang, M. E. Carnes, L. Scentena, P. H. Cheong, D. W. Johnson, Vibrational Spectroscopy and Theoretical Studies of M13 Clusters in the Solid State and Aqueous Solutions. *Inorg. Chem.*, Manuscript in Progress.

(20)   G. Canzi, A. A. Mrse, C. P. Kubiak, *J. Phys. Chem. C* **2011**, *115*, 7972–7978.

(21)   R. Terrill, T. Postlethwaite, *J. Am. Chem. Soc.* **1995**, *117*, 12537–12548.

(22)   E. W. Elliott, A. F. Oliveri, T. Zaikova, L. McKenzie, D. W. Johnson, J. E. Hutchison, Manuscript in Progress.

(23)   J. Qiu, J. Ling, A. Sui, J. E. S. Szymanowski, A. Simonetti, P. C. Burns, *J. Am. Chem. Soc.* **2012**, *134*, 1810–1816.

(24)   J. Ling, C. M. Wallace, J. E. S. Szymanowski, P. C. Burns, *Angew. Chem. Int. Ed.* **2010**, *49*, 7271–7273.

(25)   G. E. Sigmon, J. Ling, D. K. Unruh, L. Moore-Shay, M. Ward, B. Weaver, P. C. Burns, *J. Am. Chem. Soc.* **2009**, *131*, 16648–16649.

(26)   J. Ling, J. Qiu, G. E. Sigmon, M. Ward, J. E. S. Szymanowski, P. C. Burns, *J. Am. Chem. Soc.* **2010**, *132*, 13395–13402.

(27)   R. L. Johnson, C. A. Ohlin, K. Pellegrini, P. C. Burns, W. H. Casey, A Nanometer-Size Uranyl Cluster Equilibrates with Other Metastable Structures in Solution. *Nature*, *In Submission*.

Chapter III

(1)   Sardar, R.; Schumaker-Parry, J. S. *J. Am. Chem. Soc.* **2011**, *133*, 8179-8190.

(2)   Dahl, J. A.; Maddux, B. L. S.; Hutchison, J. E. *Chem. Rev.* **2007**, *107*, 2228-2269.

(3)   Wang, D.; Nap, R. J.; Lagzi, I.; Kowalcyzk, B.; Han, S.; Grzybowski, B. A.; Szleifer, I. *J. Am. Chem. Soc.* **2011**, *133*, 2192-2197.

(4)   Daniel, M.-C.; Astruc, D. *Chem. Rev.* **2004**, *104*, 293-346.

(5)   Kemp, M. M.; Kumar, A.; Mousa, S.; Park, T.; Ajayan, P.; Kubotera, N.; Mousa, S. A.; Linhardt, R. J. *Biomacromolecules* **2009**, *10*, 589-595.

(6)   Simpson, C. A.; Agrawal, A. C.; Balinski, A.; Harkness, K. M.; Cliffel, D. E. *ACS Nano* **2011**, *5*, 3577-3584.

(7)   Popovtzer, R.; Agrawal, A.; Kotov, N. A.; Popovtzer, A.; Balter, J.; Carey, T. E.; Kopelman, R. *Nano letters* **2008**, *8*, 4593-4596.

(8)   Sun, I.-C.; Eun, D.-K.; Na, J. H.; Lee, S.; Kim, I.-J.; Youn, I.-C.; Ko, C.-Y.; Kim, H.-S.; Lim, D.; Choi, K.; Messersmith, P. B.; Park, T. G.; Kim, S. Y.; Kwon, I. C.; Kim, K.; Ahn, C.-H. *Chem. Eur. J.* **2009**, *15*, 13341-13347.

(9)   Jain, S.; Hirst, D. G.; O'Sullivan, J. M. *Brit. J. Radiol.* **2012**, *85*, 101-13.

(10)   Unak, G.; Ozkaya, F.; Medine, E. I.; Kozgus, O.; Sakarya, S.; Bekis, R.; Unak, P.; Timur, S. *Colloids Surf., B* **2012**, *90*, 217-26.

(11)   Lohse, S. E.; Murphy, C. J. *J. Am. Chem. Soc.* **2012**, *134*, 15607-15620.

(12)   Kang, B.; Mackey, M. A.; El-Sayed, M. A. *J. Am. Chem. Soc.* **2010**, *132*, 1517-1519.

(13)   Oh, E.; Delehanty, J. B.; Sapsford, K. E.; Susumu, K.; Goswami, R.; Blanco-canosa, J. B.; Dawson, P. E.; Granek, J.; Shoff, M.; Zhang, Q.; Goering, P. L.; Huston, A.; Medintz, I. L. *ACS Nano* **2011**, *5*, 6434-6448.

(14)   Chen, A. H.; Silver, P. A. *Trends Cell Biol.* **2012**, *22*, 662-670.

(15)   Brown, L. O.; Hutchison, J. E. *J. Am. Chem. Soc.* **1999**, *121*, 882-883.

(16)   Woehrle, G. H.; Hutchison, J. E. *Inorg. Chem.* **2005**, *44*, 6149-6158.

(17)   Hong, R.; Fernandez, J. M.; Nakade, H.; Arvizo, R.; Emrick, T.; Rotello, V. M. *Chem. Commun.* **2006**, 22, 2347-2349.

(18)   Brust, M.; Walker, M.; Bethell, D.; Schiffrin, D. J.; Whyman, R. *J. Chem. Soc., Chem. Commun.* **1994**, 7, 801-802.

(19)   Hill, H. D.; Millstone, J. E.; Banholzer, M. J.; Mirkin, C. A. *ACS Nano* **2009**, *3*, 418-424.

(20)   Ivanov, M. R.; Bednar, H. R.; Haes, A. J. *ACS Nano* **2009**, *3*, 386-394.

(21)   Ojea-Jimenez, I.; Puntes, V. *J. Am. Chem. Soc.* **2009**, *131*, 13320-13327.

(22)   Brust, M.; Fink, J.; Schiffrin, D. J.; Kiely, C. *J. Chem. Soc., Chem. Commun.* **1995**, 16, 1655-1656.

(23)   Oh, E.; Susumu, K.; Goswami, R.; Mattoussi, H. *Langmuir* **2010**, *26*, 7604-7613.

(24)   Hostetler, M. J.; Wingate, J. E.; Zhong, C.-J.; Harris, J. E.; Vachet, R. W.; Clark, M. R.; Londono, J. D.; Green, S. J.; Stokes, J. J.; Wignall, G. D.; Glish, G. L.; Porter, M. D.; Evans, N. D.; Murray, R. W. *Langmuir* **1998**, *14*, 17-30.

(25)   Ji, X.; Song, X.; Li, J.; Bai, Y.; Yang, W.; Peng, X. *J. Am. Chem. Soc.* **2007**, *129*, 13939-48.

(26)   Wang, S.; Qian, K.; Bi, X.; Huang, W. *J. Phys. Chem. C* **2009**, *113*, 6505-6510.

(27)   Lisowski, C. E.; Hutchison, J. E. *Anal. Chem.* **2009**, *81*, 10246-10253.

(28)   Lohse, S. E.; Dahl, J. A.; Hutchison, J. E. *Langmuir* **2010**, *26*, 7504-7511.

(29)   Shon, Y.-S.; Gross, S. M.; Dawson, B.; Porter, M.; Murray, R. W. *Langmuir* **2000**, *16*, 6555-6561.

(30)   Fealy, R. J.; Ackerman, S. R.; Ferguson, G. S. *Langmuir* **2011**, *27*, 5371-5376.

(31)   Liu, X.; Atwater, M.; Wang, J.; Huo, Q. *Colloids Surf., B* **2007**, *58*, 3-7.

(32)   Koerner, H.; MacCuspie, R. I.; Park, K.; Vaia, R. A. *Chem. Mater.* **2012**, *24*, 981-995.

(33)   Haben, P. M.; McKenzie, L. C.; Kevan, S. D.; Hutchison, J. E. *J. Phys. Chem. C* **2010**, *114*, 22055-22063.

(34)   Polte, J.; Ahner, T. T.; Delissen, F.; Sokolov, S.; Emmerling, F.; Thunemann, A. F.; Kraehnert, R. *J. Am. Chem. Soc.* **2010**, *132*, 1296-1301.

(35)   Richman, E. K.; Hutchison, J. E. *ACS Nano* **2009**, *3*, 2441-2446.

(36)   Wagner, J.; Köhler, J. M. *Nano Lett* **2005**, 5, 685-691.

(37)   Karnik, R.; Gu, F.; Basto, P.; Cannizzaro, C.; Dean, L.; Kyei-Manu, W.; Langer, R.; Farokhzad, O. C. *Nano Lett* **2008**, 8, 2906-2012.

(38)   Marre, S.; Jensen, K. F. *Chem. Soc. Rev.* **2010**, *39*, 1183-1203.

(39)   Park, J. I.; Saffari, A.; Kumar, S.; Gunther, A.; Kumacheva, E. *Annu. Rev. Mater. Res.* **2010**, *40*, 415-443.

(40)   DeMello, A. J. *Nature* **2006**, *442*, 394-402.

(41)   Woehrle, G. H.; Brown, L. O.; Hutchison, J. E. *J. Am. Chem. Soc.* **2005**, *127*, 2172-2183.

(42)   Reeves, J. H.; Song, S.; Bowden, E. F. *Anal. Chem.* **1993**, *65*, 683-688.

(43)   Takegawa, Y.; Deguchi, K.; Ito, S.; Yoshioka, S.; Sano, A.; Yoshinari, K.; Kobayashi, K.; Nakagawa, H.; Monde, K.; Nishimura, S. *Anal. Chem.* **2004**, *76*, 7294-7303.

(44)   Ilavsky, J.; Jemian, P. R. *J. Appl. Crystallogr.* **2009**, *42*, 347-353.

Chapter IV

(1)   D-E. Lee, H. Koo, I-C. Sun, J. H. Ryu, K. Kim; I. C. Kwon, *Chem. Soc. Rev.*, **2012**, 41, 2656.

(2)   S. Rana, A. Bajaj, R. Mout; V. M. Rotello, *Adv. Drug Deliver. Rev.*, **2012**, 64, 200.

(3)   K. Saha, S. S. Agasti, C. Kim, X. Li; V. M. Rotello, *Chem. Rev.*, **2012**, 112, 2739.

(4)   Z. Cheng, A. Al Zaki, J. Z. Hui, V. Muzykantov; A. Tsourkas, *Science*, **2012**, 338, 903.

(5)   N. Desai, *AAPS J.* **2012**, 14, 282.

(6)   H. C. Kolb, M. G. Finn; K. B. Sharpless, *Angew. Chem. Int. Ed.*, **2001**, 40, 2004.

(7)   J. Turkevich, P. C. Stevenson; J. Hiller, *Discuss. Faraday Soc.*, **1951**, 11, 55.

(8)   J. L. Brennan, N. S. Hatzakis, T. R. Tshikhudo, N. Dirvianskyte, V. Razumas, S. Patkar, J. Vind, A. Svendsen, R. Nolte, A. E. Rowan,; M. Brust, *Bioconjugate Chem.*, **2006**, 17, 1373.

(9)   D. Baranov; E. N. Kadnikova, *J. Mater. Chem.*, **2011**, 21, 6152.

(10)   P. Zhao, M. Grillaud, L. Salmon, J. Ruiz; D. Astruc. *Adv. Synth. Catal.*, **2012**, 354, 1001.

(11)   E. Boisselier, L. Salmon, J. Ruiz; D. Astruc, *Chem. Commun.*, **2008**, 5788.

(12)   N. Li, P. Zhao, L. Salmon, J. Ruiz, M. Zabawa, N. S. Hosmane; D. Astruc, *Inorg. Chem.*, **2013**, 52, 11146.

(13)   P. Gobbo, S. Novoa, M. C. Biesinger; M. S. Workentin, *Chem. Commun.*, **2013**, 49, 3982.

(14)   D. Flemming, C. Thode; M. Williams, *Chem. Mater.,* **2006**, 18, 2327.

(15)   C. Thode; M. Williams, *J. Colloid Interface Sci.*, **2008**, 320, 346.

(16)   R. Shukla, V. Bansal, M. Chaudhari, A. Basu, R. R. Bhonde; M. Sastry, *Langmuir*, **2005**, 21, 10644.

(17)   F. Fringuelli, F. Pizzo; L. Vaccaro, *Synthesis*, **2000**, 5, 646.

(18)   P. Haben, E. Elliott; J. Hutchison, *Nano Lett.*, in submission.

(19)   J. Z. Fang; D. J. Lee, *Chem. Eng. Sci.*, **1999**, 56, 3797.

(20)   A. Karakoti, S. Das, S. Thevuthasan; S. Seal, *Angew. Chem. Int. Ed.*, **2011**, 50, 1980.

(21)   S. Sweeney, G. H. Woehrle; J. E. Hutchison, *J. Am. Chem. Soc.*, **2006**, 128, 3190.

(22)   J. Ilavsky; P. R. Jemian, *J. Appl. Cryst*, **2009**, 42, 347.

(23)   A. Salic; T. J. Mitchison, *P. Natl. Acad. Sci. USA*, **2008**, 105, 2415.

Chapter V

(1)   Saha, K., Agasti, S., Kim, C., Li, X., Rotello, V. Gold Nanoparticles in Chemical and Biological Sensing *Chem. Rev.* **2012**, 112, 5, 2739-2779.

(2)   Pina, C., Falletta, E., Prati, L., Rossi, M. Selective oxidation using gold *Chem Soc Rev.* **2008**, 37, 2077-2095.

(3)   Haruta, M. Nanoparticulate Gold Catalysts for Low-Temperature CO Oxidation. *J. New. Mat. Electrochem. Systems* **2004**, 7, 163-172.

(4)   Linic, S., Christopher, P., Ingram, D. Plasmonic-metal nanostructures for efficient conversion of solar to chemical energy. *Nature Materials* **2011**, 10, 911-920.

(5)   Wang, J., Lee, Y-J, Chadha, A., Yi, J., Jesperson, M., Kelley, J., Nguyen, H., Nimmo, M., Malko, A., Vaia, R., Zhou, W., Hsu, J.. Effect of Plasmonic Au Nanoparticles on Inverted Organic Solar Cell Performance. *J. Phys. Chem. C.* **2013**, 117(1), 85-91.

(6)   Brust M, Walker M, Bethell D, Schiffrin DJ, Whyman R. Synthesis of Thiol-derivatised Gold Nanoparticles in a Two-phase Liquid-Liquid System. *J Chem Soc, Chem Commun* **1994**, 801.

(7)   Ojea-Jimenez, I., Bastus, N., Puntes, V. Influence of the Sequence of the Reagents Addition in the Citrate-Mediated Synthesis of Gold Nanoparticles *J. Phys. Chem. C* **2011**, 115, 15752-15757.

(8)   Lohse, S., Dahl, J., Hutchison, J. Direct Synthesis of Large Water-Soluble Functionalized Gold Nanoparticles Using Bunte Salts as Ligand Precursors. *Langmuir* **2010**, 26, 7504.

(9)   Haben, P., Elliott III, E., Hutchison, J. Facile synthesis of thiol-stabilized, water-soluble gold nanoparticles with targeted core sizes from 2-10 nm. *JACS*, Manuscript in submission.

(10)   Oh, E., Susumu, K., Goswami, R., Mattoussi, H. One-Phase Synthesis of Water-Soluble Gold Nanoparticles with Control over Size and Surface Functionalities. *Langmuir* **2010**, 26, 10, 7604-7613.

(11)   Pursell, C., Chandler, B., Manzoli, M., Boccuzzi, F. CO Adsoption on Supported Gold Nanoparticle Catalysts: Application of the Temkin Model. *J. Phys. Chem. C.* **2012**, 116, 11117-11125.

(12)   Foster, E., Kearns, G., Goto, S., Hutchison, J. Patterned Gold-Nanoparticle Monolayers Assembled on the Oxide of Silicon. *Adv. Mater.* **2005**, 17, 1542-1545.

(13)   Sweeney, S., Woehrle, G., Hutchison, J. Rapid Purification and Size Separation of Gold Nanoparticles via Diafiltration. *J Am. Chem. Soc.* **2006**, 128, 10, 3190.

(14)   Woehrle, G., Brown, L., Hutchison, J. Thiol-functionalized, 1.5-nm Gold Nanoparticles through Ligand Exchange Reactions: Scope and Mechanism of Ligand Exchange. *J. Am. Chem. Soc.* 2005, 127, 2172-2183.

(15)   Lopez-Sanches, J.A, et al., A. Facile removal of stabilizer-ligands from supported gold nanoparticles. *Nature Chemistry* **2011**, 3, 551-556.

(16)   Catalysis by Gold. Geoffrey C. Bond, Catherine Louis, David T. Thompson. Imperial College Press 2006

(17) Kilmartin, J., Sarip, R. Grau-Crespo, R., Di Tommaso, D., Hogarth, G., Prestipino, C., Sankar, G. Following the Creation of Active Gold Nanocatalysts from Phosphine-Stabilized Molecular Clusters. *ACS Catal.* **2012**, 2, 957-963.

(18) Menard, L., Xu, F., Nuzzo, R., Yang, J. Preparation of TiO2-supported Au nanoparticle catalysts from a Au13 cluster precursor: Ligand removal using ozone exposure versus a rapid thermal treatment. *J. Catal.* **2006**, 243, 64-73.

(19) Sze, C., Gulari, E., Demczyk, B. .Structure of Coprecipitated Gold–iron Oxide Catalyst Materials. *Mat. Lett.* **1998**, 36, 11–16.

(20) Ma, Z., Dai, S. Design of Novel Structured Gold Nanocatalysts. ACS Catalysis 2011, 1, 805–818.

(21) Yan, W., Mahurin, S. M., Pan, Z., Overbury, S. H., Dai, S. Ultrastable Au Nanocatalyst Supported on Surface-modified TiO_2 Nanocrystals. *J. Am. Chem. Soc.* **2005**, 127, 10480–1.

(22) Zanella, R., Giorgio, S., Henry, C. R., Louis, C. Alternative Methods for the Preparation of Gold Nanoparticles Supported on TiO_2. *J. Phys. Chem.* B **2002**, 106, 7634–7642.

(23) Yang, Y.-F., Sangeetha, P., Chen, Y.-W. $Au/FeO_x − TiO_2$ Catalysts for the Preferential Oxidation of CO in a H_2 Stream. *Ind. Eng. Chem. Res.* **2009**, 48, 10402–10407.

(24) Worley, C.G, Linton, R.W, Removing sulfur from gold using ultraviolet/ozone cleaning. *Vac. Sci. Technol. A.* **1995** 13(4), 2281-2282.

(25) King, D. E. Oxidation of Gold by Ultraviolet Light and Ozone at 25 °C. *J. Vacuum Sci. Tech. A* **1995**, 13, 1247.

(26) Zhang, Y.; Terrill, R. H.; Bohn, P. W. Ultraviolet Photochemistry and Ex Situ Ozonolysis of Alkanethiol Self-Assembled Monolayers on Gold. *Chem. Mater.* **1999**, 11, 2191–2198.

(27) Norrod, K. L.; Rowlen, K. L. Ozone-Induced Oxidation of Self-Assembled Decanethiol: Contributing Mechanism for "Photooxidation"? *J. Am. Chem. Soc.* **1998**, 120, 2656–2657.

(28) Campbell, C. The Active Site in Nanoparticle Gold Catalysis. *Science* **2004**, *306*, 234–235.

(29) Kearns, G. J., Foster, E. W., Hutchison, J. E., Substrates for direct imaging of chemically functionalized SiO2 surfaces by transmission electron microscopy. *Anal. Chem.* **2006,** *78* (1), 298-303.

(30)   Haruta, M. Gold as a novel catalyst in the 21st century: Preparation, working
         mechanism and applications. *Gold Bull*. **2004,** 37(1), 27-36.

(31)   Dasog, M., Scott, R. W. J. Understanding the Oxidative Stability of Gold
         Monolayer-protected Clusters in the Presence of Halide Ions Under Ambient
         Conditions. *Langmuir* **2007**, 23, 3381–7.

(32)   Neff, G. A., Page, C. J., Meintjes, E., Tsuda, T., Pilgrim, W. C., Roberts, N.,
         Warren, W. W. Hydrolysis of surface-bound phosphonate esters for the self-
         assembly of multilayer films: Use of solid state magic angle spinning P-31 NMR
         as a probe of reactions on surfaces. *Langmuir* **1996,** *12* (2), 238-42.

(33)   Dugas, V., Chevalier, Y. Surface hydroxylation and silane grafting on fumed
         and thermal silica. *J. Colloid Int. Sci. .***2003,** 264 (2), 354-361.

(34)   Hong, H., Sackett, D., Mallouk, T. Adsorption of well-ordered zirconium
         phosphonate multilayer films on high surface area silica. *Chem. Mater.* **1991**, 3,
         521-527.

(35)   Woehrle, G. H., Hutchison, J. E., Saim, O., Finke, R. G., Analysis of
         Nanoparticle Transmission Electron Microscopy Data Using a Public- Domain
         Image-Processing Program, Image. *Turk. J. Chem.* **2006,** *30*, 1-13.

(36)   Bourg, M.-C., Badia, A., Lennox, R. B. Gold−Sulfur Bonding in 2D and 3D
         Self-Assembled Monolayers: XPS Characterization. *J. Phys. Chem. B* . **2000,**
         104, 6562–6567.

(37)   Lindberg, B. J., Hamrin, K., Johansson, G., Gelius, U., Fahlman, A., Nordling,
         C., Siegbahn, K. Molecular Spectroscopy by Means of ESCA II. Sulfur
         Compounds. Correlation of Electron Binding Energy with Structure. *Physica
         Scripta.* **1970**, 1, 286–298.

(38)   Castner, D. G., Hinds, K., Grainger, D. W. X-ray Photoelectron Spectroscopy
         Sulfur 2p Study of Organic Thiol and Disulfide Binding Interactions with Gold
         Surfaces. *Langmuir* **1996**, 7463, 5083–5086.

(39)   Hostetler, M., Templeton, A., Murray, R. Dynamics of Place-Exchange
         Reactions on Monolayer-Protected Gold Cluster Molecules. *Langmuir*. **1999**,
         15, 3782-3789.

(40)   Johnson, B. N., Mutharasan, R. Regeneration of Gold Surfaces Covered by
         Adsorbed Thiols and Proteins Using Liquid-Phase Hydrogen Peroxide-
         Mediated UV-Photooxidation. *J. Phys. Chem. C* **2013**, 117, 1335–1341.

(41)   Pang, S., Kurosawa, Y., Kondo, T., Kawai, T. Decomposition of Monolayer
         Coverage on Gold Nanoparticles by UV/ozone Treatment. *Chem. Lett.* **2005**,
         34, 544–545.

(42)   Bak, J.; Clausen, S. Signal-to-Noise Ratio of FT-IR CO Gas Spectra. *Appl. Spectrosc.* **1999,** 53(6)**,** 697-700.

(43)   Smith, B. L.; Hutchison, J. E. Transformations during Sintering of Small (D_{core} < 2 nm) Ligand-Stabilized Gold Nanoparticles: Influence of Ligand Functionality and Core Size *J. Phys. Chem. C* **2013**, 117, 25127-25137.

Appendix A

(1)   Lohse, S. E.; Dahl, J. A.; Hutchison, J. E. Langmuir **2010**, 26, 7504-7511.

(2)   Haben, P. M.; McKenzie, L. C.; Kevan, S. D.; Hutchison, J. E. *J. Phys. Chem. C* **2010**, 114, 22055-22063.

(3)   Ilavsky, J.; Jemian, P. R. *J. Appl. Crystallogr.* **2009**, 42, 347-353.

(4)   Woehrle, G. H.; Hutchison, J. E.; Ozkar, S.; Finke, R. G. *Turk. J. Chem.* **2006**, 30, 1-13.

(5)   Sweeney, S. F.; Woehrle, G. H.; Hutchison, J. E. *J. Am. Chem. Soc.* **2006**, 128, 5220-5227.

(6)   Pecsok, R. L. *J. Am. Chem. Soc.* **1953**, 75, 2862-2864.

(7)   Wang, S.; Qian, K.; Bi, X.; Huang, W. *J. Phys. Chem. C* **2009**, 113, 6505-6510.

(8)   Woehrle, G. H.; Warner, M. G.; Hutchison, J.E. *Langmuir* **2004**, 20, 5982-5988.

Appendix B

(1)   Lohse, S. E.; Dahl, J. A.; Hutchison, J. E. *Langmuir*. **2010**, *26*, 7504-7511.

(2)   Amaral, S. P.; Fernandez-Villamarin, M.; Correa, J.; Riguera , R.; Fernandez-Megia, E. *Org. Lett.* **2011**, *13*, 4522-4525.

(3)   Haben, P. M. Controlling the Synthesis of Bunte Salt Stabilized Gold Nanoparticles Using a Microreactor Platform in Concert with Small Angle X-ray Scattering Analysis. Ph.D. Dissertation [Online], The University of Oregon, Eugene, OR, October 2013. http://hdl.handle.net/1794/13429 (accessed Apr 29, 2014.)

(4)   Woehrle, G. H.; Brown, L. O.; Hutchison, J. E. *J. Am. Chem. Soc.* **2005**, 127, 2172-2183

(5)   Yu, C-S.; Oberdorfer, F. *Synlett.* **2000**, 1, 86-88.